2-14-2014

Synthesis, Characterization, and Electrochemical Evaluation of Novel, Highly Active Catalysts for the Oxygen Reduction Reaction in Alkaline Media

Danae Jacquelyne Davis

Danae J. Davis

Candidate

The Department of Chemistry and Chemical Biology

Department

This thesis is approved, and it is acceptable in quality and form for publication:

Approved by the Thesis Committee:

Richard A. Kemp, Ph.D., Chairperson

Yang Qin, Ph.D.

Terefe Habteyes, Ph.D.

Timothy N. Lambert, Ph.D.

SYNTHESIS, CHARACTERIZATION, AND

ELECTROCHEMICAL EVALUATION OF NOVEL, HIGHLY

ACTIVE CATALYSTS FOR THE OXYGEN REDUCTION

REACTION IN ALKALINE MEDIA

by

DANAE J. DAVIS

BACHELOR OF ARTS, CHEMISTRY

THESIS

Submitted in Partial Fulfillment of the
Requirements for the Degree of

Master of Science

Chemistry

The University of New Mexico
Albuquerque, New Mexico

December, 2013

DEDICATION

This work is lovingly dedicated to my family,

whose constant encouragement made this possible.

Philippians 4:13

ACKNOWLEDGEMENTS

I would like to gratefully acknowledge my co-advisors, Dr. Richard A. Kemp and Dr. Timothy N. Lambert, for encouraging me to pursue a graduate degree and helping me to develop both as a student and a researcher. I would also like to thank Dr. Yang Qin and Dr. Terefe Habteyes for kindly agreeing to serve as members of my thesis committee.

I would like to thank Mr. Julian A. Vigil for his assistance in the electrochemical evaluation of numerous catalyst materials. I am grateful to the following individuals for their gracious contributions to various aspects of this research: Dr. Mark Rodriguez (SNL) for x-ray diffraction analyses, Dr. Michael Brumbach (SNL) for interpretation of x-ray photoelectron spectroscopy data, Dr. Eric Coker (SNL) for surface area analyses, Ms. Bonnie McKenzie and Mrs. Amy Allen (SNL) for scanning electron microscopy, Dr. Steven J. Limmer (SNL) for assistance in interpreting electrochemical data, and Dr. Ying-Bing Jiang (UNM) for assistance with transmission electron microscopy studies. I would also like to acknowledge the research group of Dr. James Tour at Rice University.

To my parents, Michael and Deborah Davis, thank you for being a constant source of unwavering support and love. To my brother, Landon Davis, thank you for consistently reminding me to focus on the positives in life. To my fiancé, Phillip London, thank you for your continual optimism and perpetual reminders to be confident.

◆ ◆ ◆

This work was funded by Sandia National Laboratories. Sandia National Laboratories is a multi-program laboratory operated by Sandia Corporation, a wholly owned subsidiary of Lockheed Martin Corporation, for the United States Department of Energy's National Nuclear Security Administration under Contract DE-AC04-94AL8500.

SYNTHESIS, CHARACTERIZATION, AND ELECTROCHEMICAL EVALUATION OF NOVEL, HIGHLY ACTIVE CATALYSTS FOR THE OXYGEN REDUCTION REACTION IN ALKALINE MEDIA

By

Danae J. Davis

Bachelor of Arts, Chemistry, University of New Mexico, 2011

Master of Science, Chemistry, University of New Mexico, 2013

ABSTRACT

Efficient electrocatalysts for the oxygen reduction reaction (ORR) are needed for fuel cells and next generation metal-air batteries, as the overall efficiency of these systems is currently limited by cathode kinetics. While Pt and Pt-based alloys demonstrate excellent electrocatalytic activities, their prohibitive cost and rarity ultimately prevents their widespread utilization. Catalyst materials that are highly active, stable, and cost effective are needed.

Manganese oxide (α-MnO_2) catalysts doped with varying amounts of Cu or Ni were synthesized, characterized, and evaluated for their performance as catalysts for the oxygen reduction reaction in alkaline electrolyte. Cu-α-MnO_2 nanowire catalysts consistently attained higher terminal current densities than those achieved with undoped α-MnO_2. As the amount of Cu-dopant in the nanowire increases, the kinetic rate constants increase, and the charge transfer resistances decrease. By studying the physicochemical properties of the Cu-doped catalysts, it was discovered that an increase in Cu-content

corresponds to an increase in catalyst surface area, as well as an expansion of the crystalline lattice. The observed improvement in catalytic behavior can also be attributed to an increase in surface Mn^{3+} character, as measured by X-ray photoelectron spectroscopy (XPS), that corresponds to an increase in Cu-dopant at the surface. Similarly, an increase in Mn^{3+} character is hypothesized to be a significant factor in the activities of Ni-α-MnO_2 catalysts, though the observed catalytic performance of this catalyst series does not trend directly with Ni-content.

In addition, a novel composite containing Ag and graphene nanoribbons (Ag-GNRs) was also studied. Catalytic studies revealed that the Ag-GNR composite outperforms a commercial Ag-Carbon catalyst as determined by comparing terminal current densities, *n*-values, kinetic rate constants, onset potentials, and half-wave potentials. In addition, the Ag-GNR composite is more electrocatalytically selective than the benchmark Pt/C catalyst when subjected to simulated methanol crossover effects.

TABLE OF CONTENTS

LIST OF FIGURES

Chapter 1

Chapter 2

Chapter 3

Chapter 4

Chapter 5

LIST OF EQUATIONS

LIST OF TABLES

Chapter 2

Chapter 3

Chapter 4

Chapter 5

Chapter 1

The Oxygen Reduction Reaction:

Relevance, Mechanisms, and Methods of Electrochemical Analysis

1.1 Introduction

Before many promising advanced technologies, such as optimized portable electronics, electric vehicles, and smart energy grids, can be widely utilized in modern society improved technologies capable of sustaining the necessary capacities for energy storage and conversion must be developed. [1] It is widely acknowledged that the existing supply of natural resources cannot support ever-increasing demands for power, which are expected to total 42 terawatts by 2050. [2] Thus, there is a momentous need for innovative power sources capable of sustaining rapidly evolving technologies.

Environmental compatibility, economic feasibility, and overall performance are crucial criteria that must be considered in the research and development phases of advanced power sources. Currently, metal-air batteries and fuel cells are two electrochemical systems being widely studied for their potential to meet the practical gravimetric energy density of gasoline. [1, 3, 4] The oxygen reduction reaction, commonly referred to as ORR, is a critical electrochemical process that occurs in both fuel cells and metal-air batteries. The factors currently limiting the performance of these promising electrochemical systems are the kinetics and energetics of the reduction reaction occurring at the cathode. Electrocatalysts for ORR must be highly active and durable. Since the kinetics and energetics of the oxygen reduction reaction determine the efficiency of the electrochemical system, sluggish processes will have an adverse impact

on the overall performance. In the past, many development efforts have focused on noble metal catalysts. While noble metals such as platinum, platinum alloys, gold, silver, ruthenium, and palladium demonstrate remarkable catalytic performances, these materials are costly and relatively scarce, thereby preventing widespread implementation of technologies benefitting from improved ORR kinetics. [5-8] Therefore, more economically viable, highly active electrocatalyst materials are needed.

Ultimately, bidirectional catalysts capable of catalyzing not only ORR but also the oxygen evolution reaction (OER) are needed for numerous applications that require reversibility. Bifunctional catalysts are employed in secondary batteries (which, unlike primary batteries, are electrically rechargeable) and regenerative fuel cells. [9] A bifunctional catalyst in a lithium-oxygen battery, for example, enables not only ORR during discharge but also OER upon charging. [2] OER is also integral in applications in which water is electrolyzed to form hydrogen and oxygen, applications which would enable chemical fuels to be derived from solar or electrical energy.[10, 11] The work reported in this thesis focuses exclusively on developing improved catalysts for the ORR in alkaline electrolyte; future work will be directed to developing the bifunctional catalysts necessary for the further development of advanced battery technologies.

Clearly, the path forward to achieving fully optimized electrochemical systems is not immediately apparent. As such, many research efforts are currently dedicated to investigating highly active, durable, cost effective materials in an attempt to enhance the electrochemical capabilities of batteries and fuel cells and thus ultimately enable new technologies to be realized. Numerous affordable materials that have been recently developed offer unique electronic properties and nanoscale structures that can provide

interesting catalytic behaviors, warranting further investigation for future applications in catalysis.

1.2 Pathways of ORR

The oxygen reduction reaction is thought to proceed through two possible pathways in alkaline solution, as seen below. [7] The reactions in acidic solution are also provided for comparison; however, the research presented in this thesis will focus exclusively on catalyzing the reaction in alkaline media. The reaction pathways in alkaline solution are either (i) a direct, four-electron process in which O_2 is reduced to OH^-, or (ii) a less efficient two-step, two-electron pathway that involves the formation of hydrogen peroxide ions as an intermediate, which can then be further reduced by another two-electron process or can decompose catalytically. It is important to note that the catalytic decomposition process forms ½ O_2, which can be reintroduced into the reduction pathways. [7, 12]

Obviously, the direct reduction pathway, which reduces oxygen to water, is ideal, as the indirect production of reactive peroxide species can corrode various components of electrochemical systems, such as membranes within a fuel cell or carbonaceous additives. [7, 13]

Alkaline Solution:

(i) Direct four electron pathway:
$O_2 + 2H_2O + 4e^- \rightarrow 4OH^-$

(ii) Indirect (peroxide) pathway:
$O_2 + H_2O + 2e^- \rightarrow OH^- + HO_2^-$

Followed by either

(a) The further reduction of peroxide:
$HO_2^- + H_2O + 2e^- \rightarrow 3OH^-$
or alternatively,

(b) The catalytic peroxide decomposition
$HO_2^- \rightarrow$ ½ $O_2 + OH^-$

Acidic Solution:

(i) Direct four electron pathway:
$O_2 + 4H^+ + 4e^- \rightarrow 2H_2O$

(ii) Indirect (peroxide) pathway:
$O_2 + 2H^+ + 2e^- \rightarrow H_2O_2$

Followed by either

(a) Subsequent reduction:
$H_2O_2 + 2H^+ + 2e^- \rightarrow 2H_2O$
or,

(b) Decomposition of peroxide
$2H_2O_2 \rightarrow 2H_2O + O_2$

It has been acknowledged that, for any catalyst, the direct four-electron process is not the predominant mechanism; rather, a stepwise four-electron process that occurs via two consecutive two-electron reactions in which peroxide is formed and reduced is the probable reduction mechanism. [5] Therefore, the ideal catalyst material must be capable of efficient electron transfer and rapid peroxide decomposition or reduction. [5] A discussion of how electrochemical techniques can be utilized to elucidate the reaction pathway, measure peroxide formation, and compare catalyst materials follows.

1.3 Methods for Electrochemical Analysis

Electrochemical testing of catalysts for the oxygen reduction reaction is typically performed using techniques employing a rotating disk electrode (RDE) or rotating ring disk electrode (RRDE). Rotating electrodes are used because they enable the controlled transport of oxygen (O_2) from the bulk of the electrolyte solution to the electrode. [14] By rotating the electrode, the electrolyte solution is continuously mixed, and the solution is drawn to the disk surface. [15] The resulting solution flow patterns in a given system are governed by many equations of hydrodynamics, which have been described extensively in numerous sources.[8, 14] The general principles of a rotating electrode can be understood by considering a disk electrode of a given radius rotating in a liquid at a constant rate. The liquid immediately adjacent to the surface of the disk participates in the rotational motion, while the liquid not immediately adjacent also rotates to some extent due to the viscosity of the solution. [8] As distance from the electrode increases, the rotational motion decreases. The centrifugal forces cause the rotating liquid to be transported to the periphery of the disk; assuming a continuous supply of liquid to the disk surface, this

process is repeated. [14] The limiting current, therefore, is predicted to be proportional to the square root of the rotation rate. [8] Figure 1.1 illustrates the general schematics for the rotating disk system.

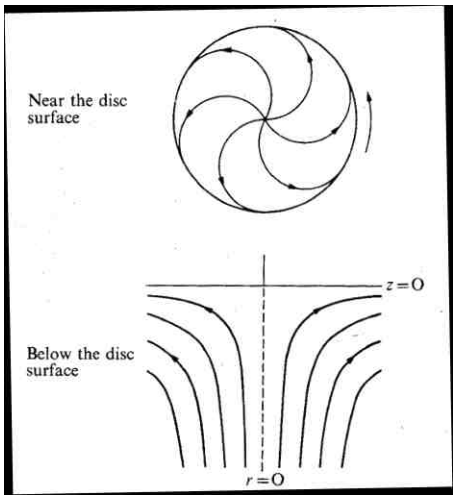

Figure 1.1: Schematic streamlines for the rotating disk system [14]

For electrochemical experiments aimed at studying the reduction of O_2, a thin layer of the electrocatalyst of interest is prepared on the glassy carbon surface of the disk electrode. Typically, this is achieved by drop coating a small aliquot of catalyst suspension, made by dispersing a known amount of catalyst via ultrasonication in an appropriate solvent. A solution of Nafion polymer is commonly included in the catalyst film to act as a binder that improves the adherence of the catalyst to the glassy carbon surface. [6, 15-17] Oxygen is purged through the electrolyte prior to the start of the experiment.

In linear scanning voltammetry, the current density at the working electrode is monitored as a function of the applied potential, which is scanned from a positive

potential to a negative potential, causing oxygen to be reduced. Figure 1.2 illustrates a typical linear scanning voltammogram (LSV) obtained at 500 rpm.

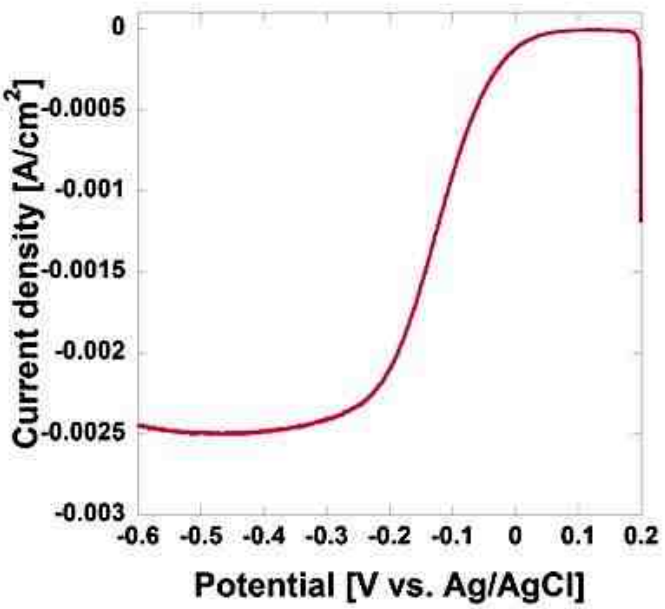

Figure 1.2: Representative LSV obtained at 500 rpm

In the curve shown in Figure 1.2, the potential is scanned from a positive potential (0.2 V vs. Ag/AgCl) to a negative potential (-0.6 V vs. Ag/AgCl). As the applied potential becomes increasingly negative, the magnitude of the current increases due the reduction of O_2. Control experiments performed in a N_2-purged solution in the same electrochemical window enable the subtraction of the background signal.

Rotation of the disk electrode at discrete rates changes the flux, or mass transport, of O_2 to the surface; as the rate of rotation increases, the flux of O_2 to the electrocatalyst increases, and the limiting current becomes increasingly negative, which is indicative of more oxygen arriving at the disk surface, resulting in increasingly more cathodic

(reduction) current being generated by the ORR. [14, 15, 18] The effect of rotation rate is illustrated in Figure 1.3.

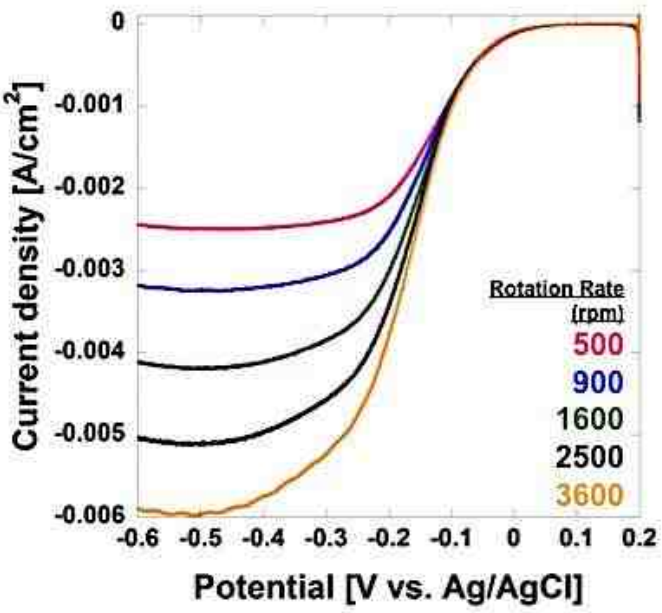

Figure 1.3: Representative LSVs demonstrating an increase in observed current as a result of increased rotation rate.

The curves obtained in RDE experiments can be analyzed using the Koutecky-Levich equation, which is as follows:

$$\frac{1}{i} = \frac{1}{i_k} + \frac{1}{i_d} = -\frac{1}{nFAkC^0} - \frac{1}{0.62nFAD_{O2}^{2/3}\nu^{-1/6}C^0\omega^{1/2}}$$

Equation 1.1: The Koutecky-Levich Equation

where i, i_k, and i_d represent the measured, kinetic, and diffusion-limiting current, respectively, n corresponds to the number of electrons transferred in the reduction, F is the Faraday constant, A is the geometric area of the electrode (cm^2), k is the rate constant

for oxygen reduction, C^o is the saturated concentration of oxygen in electrolyte (0.1 M KOH, 1.14 x 10^{-6} mol cm^{-3}), D_{O2} is the diffusion coefficient of oxygen (1.73 x 10^{-5} cm^2/s), v is the kinetic viscosity of solution (0.01 cm^2/s), and ω is the rotation rate (rad/s). [18, 19]

Applying the Koutecky-Levich equation to RDE data enables the extraction of several important catalytic criteria. The first is termed *n*-value, which is the number of electrons involved in the reduction process (*n*); the *n*-value is calculated using the slope of the Koutecky-Levich line, which is obtained when the inverse of the current is plotted as a function of the inverse square root of the rotation rate. [18] Referencing the reaction schemes previously discussed and shown on page 3, it is apparent that the nominal value is equal to four. An *n*-value of four electrons indicates that the either a) the direct four electron reduction pathway or b) the competing apparent four electron process involving the formation and rapid reduction of peroxide are the predominant mechanisms. However, because there are numerous reactions occurring simultaneously, with complex electron-transfer processes involving O, OH, O_2^-, and HO_2^-, the n-value can actually be any value between two and four. [1, 9, 13, 20]

In addition, the kinetic rate constant (*k*) can also be calculated from the y-intercept of the Koutecky-Levich line, and it is a useful metric of comparison when studying catalysts. [18] Since the rates of electrocatalytic reactions are affected by rates of varied adsorption processes for both initial-state reactants and intermediates, the value of *k* is most relevant when employed as a means to compare the relative rates of the entire process, as opposed to a single step of the complex mechanism. [12]

When a bipotentiostat is utilized, a rotating ring disk electrode can be used to monitor two electrochemical processes concurrently. In the context of oxygen reduction, rotating ring disk electrode studies allow for measurement of the amount of peroxide being generated in the system, in addition to the aforementioned metrics obtained from RDE studies. The solution flow patterns of a rotating disk electrode cause the product generated at the disk, peroxide, to be swept radially outward. Because the ring electrode surrounds the disk electrode and is isolated electrochemically, the ring electrode can detect the amount of peroxide present. [15] By using the currents generated at both the disk (reduction of O_2) and the ring (oxidation of peroxide), hypotheses regarding the ORR mechanism can be formed. While the Koutecky-Levich equation can be used to analyze RRDE data, the equation that follows is also commonly applied, which yields an n-value for the process:

$$n = 4 \times \frac{|Id|}{|Id| + \frac{Ir}{N}}$$

Equation 1.2: Determining *n*-value using RRDE data

where I_d is the disk current, I_r is the current at the ring electrode, and N is the measured collection efficiency for the specific RRDE employed for the experiment. [14, 21-23] It should be emphasized that N is exclusively used to denote collection efficiency, a specific parameter for the ring electrode, whereas n consistently refers to the *n*-value.

Also, the following equation can be used to determine the percent peroxide generated. [14, 21, 22]

$$\% (HO_2^-) = 200 \times \frac{\frac{Ir}{N}}{\left(Id + \frac{Ir}{N}\right)}$$

Equation 1.3: Determining the percent of evolved peroxide using RRDE data

The linear scanning voltammograms contain a wealth of information that can be used to effectively assess catalyst performance and compare various catalysts. The obtained LSV curves are typically examined for onset potential, half-wave potential, and terminal current density (which can be further utilized to calculate mass activity, mA/mg). Several key criteria used for catalyst comparisons are outlined in Figure 1.4.

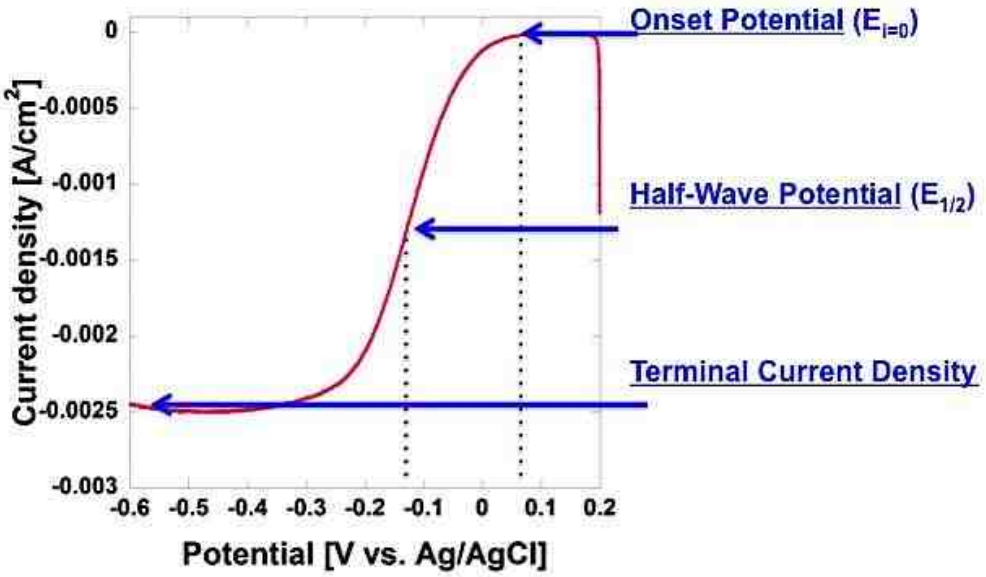

Figure 1.4: A representative LSV with the onset potential, half-wave potential, and terminal current density indicated

The onset potential ($E_{i=o}$) can be conceptualized as the energy investment that must be made before the system begins to generate reductive current; clearly, the more

positive the onset potential, the lower the overpotential required for reduction. The defined reduction potential for the ORR is 0.401V vs. NHE at 25 °C. [7] Therefore, the overpotential is the difference between the theoretical reduction potential and the experimentally observed value. Many researchers assert that the onset potential is the first potential at which the current is a negative value; [19] therefore, this potential can be easily obtained by examining the numerical data from a LSV curve. However, it has been our assertion that since the first negative current density value is often negligible in magnitude, a more effective means of determining the true onset potential is needed. Also, the negligible negative current density often does not correspond to the potential at which the LSV visibly changes slope. Therefore, we calculate the onset potential by fitting two tangential lines to the LSV and finding the potential value that corresponds to their intersection. The first tangential line is fit to the sloped region (mass transport regime) of the LSV; the second tangential line is fit to the linear region that exists before negative current density predominates. Thus, these lines intersect where the slope of the LSV visibly changes slope, yielding a value that could be considered a more representative onset potential for oxygen reduction.

The half-wave potential ($E_{1/2}$) is defined as the point half-way between zero current and the terminal current density plateau [19] - the more positive the half-wave potential, the more effective the catalyst, as it does not require high overpotentials to generate reductive current. The half-wave region is of particular interest because it is a potential range that is most realistic for the operation of electrochemical systems such as fuel cells in which ORR catalysts are commonly employed. [24]

Also relevant to any study of a novel catalyst material is a comparison to the commercial benchmark, typically regarded to be 20% Pt on Vulcan XC-72 Carbon (termed Pt/C). [1] The inclusion of an internal metric of comparison enables both the researcher and the scientific community to assess whether a not a novel material has the potential to attain or possibly exceed the catalytic activity routinely attained by Pt/C benchmarks.

While Pt-containing catalysts are known to demonstrate remarkable catalytic behavior, they are not electrocatalytically selective, meaning that these catalysts are subject to deactivation. For example, methanol crossover, a process that can occur in direct methanol fuel cells (DMFC), renders Pt catalysts relatively inactive. To show this, previous reports have demonstrated the drastic change (50 to 60% decrease) in current density that results upon injection of two weight percent methanol into an electrochemical cell in which Pt/C is the catalyst. [24] Also, Pt/C is sensitive to CO, a poison which originates from the H_2 fuel generation in conventional fuel cells. Carbon monoxide will strongly adsorb onto Pt surfaces, causing a decrease in the performance of the catalyst. [3] Therefore, another key criteria for catalysts to be employed in fuel cells is that they are electrocatalytically selective, not susceptible to possible deactivation or poisoning.

The research presented in this thesis describes the synthesis, characterization, and electrochemical evaluation of highly active, novel electrocatalysts for the oxygen reduction reaction. Chapter 2 outlines recent work in the development of manganese oxide catalysts, as well as recent syntheses of composite catalysts that augment the performance and conductivity of manganese oxides with graphene. Chapter 3 describes

the synthesis, characterization, and electrochemical evaluation of Cu-doped α-MnO_2 nanowires, performed with the goal of determining the role of the Cu-dopant species in electrocatalysis. In a similar fashion, Chapter 4 describes the synthesis, characterization, and electrochemical evaluation of Ni-doped α-MnO_2 nanowires; preliminary results regarding the specific electrocatalytic role of Ni-dopants are presented. Finally, Chapter 5 presents the electrocatalytic performance of a composite material comprised of silver nanoparticles on graphene nanoribbons. Chapter 6 provides a brief summary and overall conclusions of this research.

Chapter 2

A Brief Overview of Manganese Oxide Electrocatalysts for the Oxygen Reduction Reaction

2.1 Introduction

Manganese oxides have been utilized extensively as catalysts for the oxygen reduction reaction in alkaline electrolytes. First investigated in the early 1970s, manganese oxide was demonstrated to improve the performance of carbon-air electrodes when added in small amounts, generally less than 10% by weight. [25] Since then, numerous newly developed manganese oxide (MnO_x) catalysts have been investigated extensively for applications as ORR catalysts and have consistently demonstrated promising catalytic behavior. [19, 26, 27] In addition to favorable catalytic performance, manganese oxides offer additional benefits of being environmentally benign, abundant, and relatively inexpensive, making them compelling alternatives to costly Pt and Pt-based alloys.

2.2 Diverse Physicochemical Properties of Manganese Oxides and Related Synthetic Techniques

This overview will focus on various manganese oxides that have been synthesized on the nanoscale. Nanomaterials have typically demonstrated more promising electrochemical activities as compared to bulk materials due to their unique properties and reactivity. [19, 28] Manganese oxides are structurally versatile, and have been shown to exist in a number of diverse morphologies with varied particle sizes, stoichiometries, and crystalline phases. Many research efforts have focused on elucidating the effects of these

physicochemical factors on the electrochemical performance. As a result, changing the reaction parameters, such as duration, temperature, and reagents, often enables control of the shapes, sizes, and phases of the synthesized nanomaterials. [28]

A number of nanostructured morphologies have been synthesized, including plates, urchin-structures, spheres, flowers, cubes, wires, rods, belts, tubes, sheets, core-corona particles, stars, and dendritic hierarchical structures. [19, 26, 28-34] Uniquely shaped reaction products of various crystalline phases are commonly obtained by hydrothermal syntheses [19, 26, 30-34] or microwave-assisted hydrothermal processes, [29] but microemulsion techniques and sol-gel procedures have also been demonstrated. [28] Examples of the morphological diversity that exist in manganese oxide materials are shown in Figure 2.1.

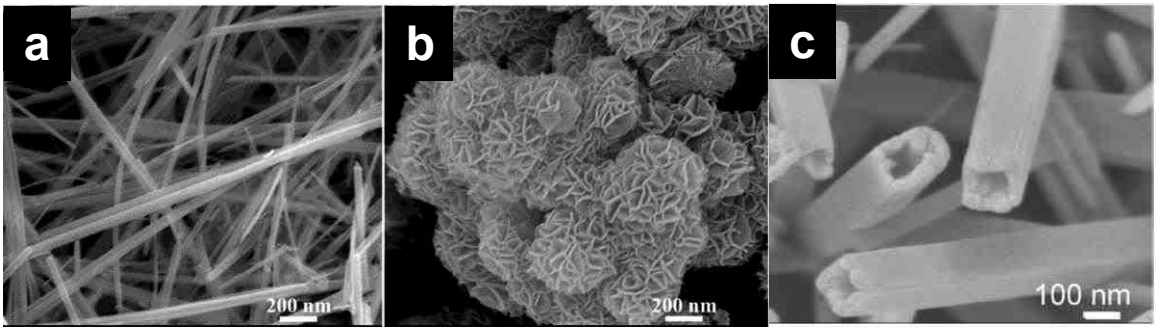

Figure 2.1: Various morphologies of nanoscale α-MnO_2.
a) nanowires [19], b) flower-like nanospheres [19], and c) nanotubes [26]

Xiao *et al*. demonstrated control of the product morphology by varying the reaction temperature of a hydrothermal synthesis using $KMnO_4$ (0.45 g) and HCl (1.0 mL, 37 wt. %) as reagents. [29] Lower temperatures (100 °C) yielded δ-MnO_2 nanosheets, whereas tetragonal α-MnO_2 nanorods and α-MnO_2 nanotubes were observed at higher temperatures (120 °C and 140 °C, respectively). [26] This work also proposed a mechanism for the transition from δ-MnO_2 nanosheets to α-MnO_2 nanostructures; initially, unstable δ-MnO_2 domains form, which are highly sensitive to both temperature and reaction

acidity. Diffusion of the δ-MnO_2 domains to the stable α-MnO_2 domains leads to a phase transition, ultimately forming α-MnO_2 exclusively. [26, 29]

Other efforts have focused on determining how the morphology changes as a function of reaction time. The work of Truong *et al*. revealed that δ-MnO_2 microflowers comprised of smaller nanosheets began to form after a mere two minutes of heating an aqueous solution of $KMnO_4$ and HCl within a microwave reactor. After five minutes, α-MnO_2 nanowires begin to form, and after six hours pure α-MnO_2 nanotubes are obtained. [29] For the hydrothermal syntheses performed by Cheng *et al*., variations in the duration of the hydrothermal reaction between $MnSO_4 \cdot H_2O$ and $KMnO_4$ caused significant changes in product morphology. Flower-like α-MnO_2 nanospheres were obtained after two hours of heating, whereas α-MnO_2 nanowires could be obtained after twelve hours. [19] In this synthesis, $KMnO_4$ is used to oxidize Mn^{2+}.

A recent report by Sun *et al*. demonstrated the syntheses of α-MnO_2, β-MnO_2, γ-MnO_2, MnOOH, Mn_3O_4, and several mixed phases via hydrothermal processes. [32] By changing the concentrations of acetic acid (AcOH) and potassium acetate (AcOK) in the reaction while maintaining constant concentrations of $MnSO_4$ and $KClO_3$ at a standard reaction time (12 hours) and temperature (160 °C), the mechanism of crystal evolution for β-MnO_2 or MnOOH to α-MnO_2 could be studied in detail. Through the precise control of the concentration of H^+ and K^+ ions, the attained product can be tailored, since these ions can affect the reaction acidity, stabilize crystal structures by occupying tunnel sites, or promote phase transformations. [32]

MnO_2 is of particular interest because it exists in a number of crystalline forms, which are denoted as α, β, γ, δ, and λ phases. The various possible arrangements of the

basic structural unit of MnO_2, the [MnO_6] octahedron, gives rise to the different crystalline forms in which the [MnO_6] octahedra are connected by sharing either corners or edges. [19] The resulting polymorphic structures can be divided into the three following classes: the one-dimensional chain-like tunnel structure (α-, β-, and γ-phases), the two-dimensional layered sheet structure (δ-MnO_2), or the three-dimensional spinel structure (λ-MnO_2). [19, 28] The one-dimensional structures of α-, β-, and γ-MnO_2 vary in the arrangement and sizes of the tunnels within the lattice. The α-MnO_2 lattice contains both (2 x 2) and (1 x 1) tunnels; β-MnO_2 contains only (1 x 1) tunnels; γ-MnO_2 contains (1 x 2) tunnels, as well as (1 x 1) tunnels. [19] A defective structure based on γ-MnO_2 is also known to exist and is called ε-MnO_2. [35] Schematics of these MnO_2 crystal structures are shown in Figure 2.2.

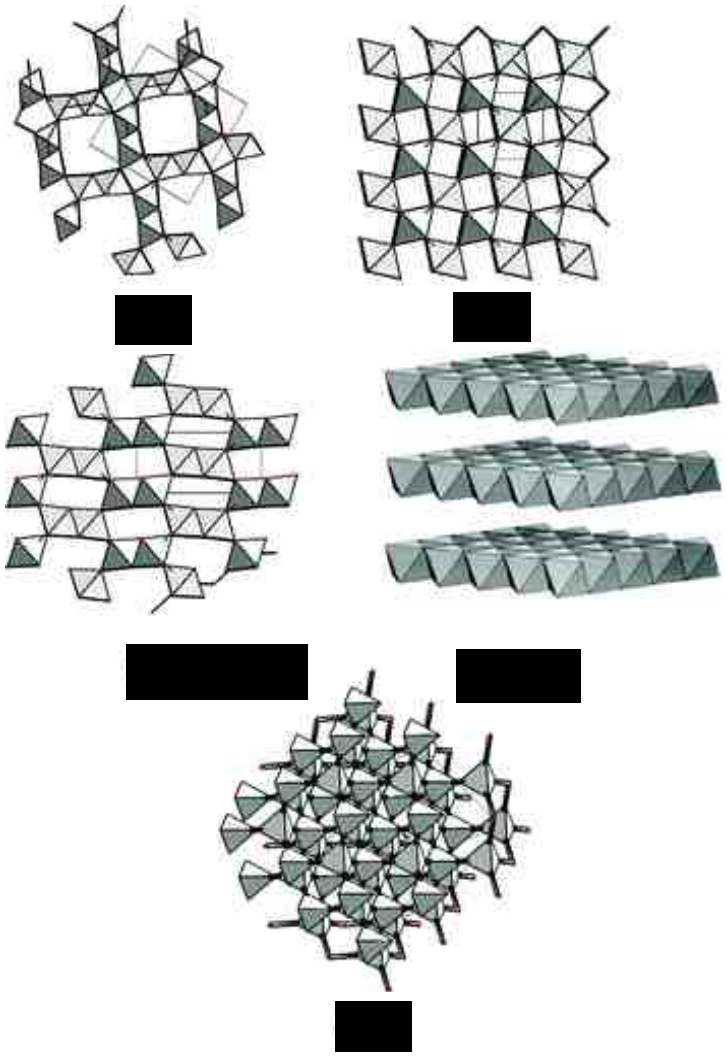

Figure 2.2: The crystal structures for α-, β-, γ-, δ-, and λ-MnO_2. [30]

2.3 Catalytic Performance and Related Rationale

It is generally accepted that phase and morphology have significant impacts on the performance of manganese oxides for various applications, which include electrochemical capacitors, [28, 30, 33] molecular sieves, [33, 36] and catalysts for the combustion of volatile organic compounds. [32, 37] However, the discussion to follow will focus solely on the demonstrated performance of manganese oxides as catalysts for the oxygen reduction reaction. Nanostructured catalyst materials are of particular interest in the field of catalyst development because these materials possess higher surface areas than bulk counterparts, causing the adsorption, diffusion, and transport of small molecules (O_2) to be more readily accommodated. [19] In addition, the porosity of nanostructures provides for improved interactions between O_2 and the catalyst. Surface defects present in nanostructures could also influence their catalytic performance. Electrochemical data clearly reveals that the catalytic behavior of nanostructures outperforms that of bulk structures and microstructures. [19]

The activities of MnO_2 phases employed as catalysts for the ORR have been demonstrated to be in the following order: α-$MnO_2 \approx \delta$-$MnO_2 > \gamma$-$MnO_2 > \lambda$-$MnO_2 > \beta$-MnO_2. [38] This order of ORR activities was determined by examining the reduction currents generated by air cathodes in air-saturated 6M KOH solution. However, another study found α-$MnO_2 > \beta$-$MnO_2 > \gamma$-MnO_2 for both attained current density and the calculated n-value. [19] These experimental findings were correlated to the physical parameters of the crystal structures. Specifically, the α-MnO_2 structure possesses (2 x 2) tunnels of approximately 4.6 Å, which are larger than the (1 x 1) and (1 x 2) tunnels

observed in the β- and γ-phases (1.89 Å and 2.3Å, respectively. [19, 30] Larger tunnels could promote the insertion and transfer of ions throughout the lattice. [19]

A recent study rigorously examined the α- and δ-MnO_2 phases and determined that α-MnO_2 nanorods and nanotubes are more catalytically active than mixed microsphere/nanosheet δ-MnO_2, [26] a difference that was attributed to the Mn-O bond strength, channel structure, and the adsorption mechanism of O_2. For δ-MnO_2, the average Mn-O bond length is 1.94 Å, as compared to the Mn-O bond length of 1.98 Å in the α-phase. Therefore, the stronger Mn-O bond length in δ-MnO_2 can be correlated to lower electrocatalytic activity. Also, the sheet-like structure of δ-MnO_2 is dense, so although O_2 can be adsorbed in the interlayer region the tunneled structure of α-MnO_2 is more favorable for the reversible adsorption and desorption processes required for electrocatalysis. [26] Finally, the O-O bond length of dioxygen, approximated to be 0.12 nm, is considered to be comparable to the size of the (1 x 1) tunnels present in α-MnO_2. Therefore, it is hypothesized that the O_2 molecule can bind in such a way that favors the cleavage of the O-O bond, promoting the four-electron pathway. [26]

It is important to note that, for each of the aforementioned electrochemical studies of various phases of MnO_2, α-MnO_2 is consistently identified as the most active species. Cheng *et al*. synthesized this phase in two different morphologies. This work further demonstrated the effect that catalyst morphology has on activities of α-MnO_2 catalysts; α-MnO_2 nanowires were more catalytically active than nanospheres of the same crystalline phase. [19] The surface areas of the nanowires (32.9 m^2/g) and nanospheres (40.1 m^2/g) were comparable.

Revisiting the possible pathways for oxygen reduction in alkaline electrolyte, the reader will recall that there are competing reduction processes occurring. The various pathways for ORR in alkaline solution are outlined as follows: [7]

(i) Direct four electron pathway:

$O_2 + 2H_2O + 4e^- \rightarrow 4OH^-$

(ii) Indirect (peroxide) pathway:

$O_2 + H_2O + 2e^- \rightarrow OH^- + HO_2^-$

Followed by either

(a) The further reduction of peroxide:

$HO_2^- + H_2O + 2e^- \rightarrow 3OH^-$ or alternatively,

(b) The catalytic peroxide decomposition:

$HO_2^- \rightarrow ½\ O_2 + OH^-$

With respect to manganese oxides (MnO_2), the following equations have been presented to demonstrate how the Mn species mediates the charge transfer processes in the oxygen reduction reaction. [19]

Four-electron pathway	**Two-electron pathway**
$MnO_2 + H_2O + e^- \leftrightarrow MnOOH + OH^-$	$MnO_2 + H_2O + e^- \leftrightarrow MnOOH + OH^-$
$2MnOOH + O_2 \leftrightarrow 2(MnOOH\bullet\bullet\bullet O)$	$MnOOH + O_2 \leftrightarrow MnOOH\bullet\bullet\bullet O_2$
$(MnOOH\bullet\bullet\bullet O) + e^- \leftrightarrow MnO_2 + OH^-$	$MnOOH\bullet\bullet\bullet O_2 + e^- \leftrightarrow MnO_2 + HO_2^-$
$O_2 + 2H_2O + 4e^- \rightarrow 4OH^-$	$O_2 + H_2O + 2e^- \rightarrow OH^- + HO_2^-$

For both possible pathways, the first proposed step is the same – a charge is transferred, generating MnOOH. The primary difference between the apparent four-electron pathway and the indirect two-electron pathway is the manner in which O_2 is adsorbed. For the adsorption necessary for a four-electron process, the O_2 must adsorb onto two MnOOH neighboring sites and the O-O bond is cleaved. In contrast, to achieve a two-electron process, the O_2 can adsorb onto a single MnOOH site. Then, the bond between O atoms is not broken, thus generating HO_2^-. It has been shown that α-MnO_2 catalyzes the ORR through an apparent four-electron process (n = 4 e^-) in which the peroxide intermediate is rapidly reduced upon its formation. [23, 26, 38] Other crystalline phases (δ-MnO_2, for example) give $n \approx 3$ e^-, indicating that both the apparent four-electron process and the two-electron process are occurring simultaneously. [26]

Manganese can exist in numerous oxidation states (+2, +3, +4, +6, and +7), a property that has been hypothesized to be a key factor in the catalytic activity of a transition metal-containing species. Because Mn-containing catalysts can be mixed-valent, it is possible that the redox reactions that occur simultaneously with the electron transfer to oxygen, as well as the storage of surface charges, are factors that enhance catalysis. [39] For α-MnO_2, the oxidation state is typically considered to be +4; however, it has been suggested that the presence of accessible Mn^{3+} ions at the surface of MnO_2 electrocatalysts can account for the differences in demonstrated electrocatalytic activities. [38] Similarly, catalytic performance has been correlated to the Mn^{3+}/Mn^{4+} redox couple and the resulting average valence. The existence of this redox couple permits moderate bond strength between the catalyst and the reactant and/or product and facilitates rapid

charge transfer. [39] The role of the Mn^{3+}/Mn^{4+} redox couple as it pertains to α-MnO_2 is discussed further in Chapter 3.

2.4 The Effect of Dopant Cations and Co-deposited Species

In order to further augment the catalytic activities demonstrated by nanoscale manganese oxides, numerous efforts have been focused on doping the crystalline lattice with various cations that are conductive and, ideally, affordable. [23, 24, 40-42] Roche *et al.* prepared MnO_x/carbon composites doped with Ni (~ 5 wt.%) or Mg (~ 2 wt. %) and found the doped catalysts to yield higher *n*-values as compared to the undoped catalyst, indicating an improvement in the ORR catalysis. The Ni-doped species was shown to give a significant decrease in the production of peroxide intermediate; the Ni was hypothesized to be stabilizing the Mn^{3+}/Mn^{4+} redox couple, thereby promoting the apparent four-electron reduction process. [23] Similarly, a Ni-doped/MnO_x catalyst prepared by Garcia *et al.* demonstrated enhanced ORR kinetics. [41] Benbow *et al.* synthesized Ni-doped α-MnO_2 nanorods that were shown to be more catalytically active than the undoped species in both aqueous and organic electrolytes. [42] In addition to studying Ni-doped α-MnO_2, in recent work from our own group, Lambert *et al*. prepared a Cu-doped α-MnO_2 and demonstrated that both the Ni- and Cu-doped species were improved ORR catalysts relative to undoped α-MnO_2 in terms of calculated *n*-value, current density, onset potential, and peroxide formation. [24] Interestingly, $CaMnO_3$ and $CaMn_3O_6$ microspheres have also been studied as ORR electrocatalysts; calculated *n*-values were 3.95 and 3.86, respectively, and the average amount of peroxide generated was 2.2% for $CaMnO_3$. [39] In addition, the Ca-Mn-O species were shown to have slightly

better activity retention during durability studies conducted over 60,000 seconds as compared to the Pt/C benchmark. [39]

Other efforts have demonstrated improved catalysis by co-depositing nanoparticles of other metals (such as Ni, Au, and Ag) onto a manganese oxide template. [19, 43, 44] By utilizing α-MnO_2 nanowires as a template material for the deposition of conductive Ni-nanoparticles, Cheng *et al.* were able to increase the conductivity of the catalyst by an order of magnitude as measured by a four-probe instrument, subsequently improving the half-wave potential, terminal current density, and calculated *n*-value. [19] The inclusion of nano-Au species on a nano-MnO_x electrode was shown to decrease the amount of peroxide that was generated, indicating the promotion of the apparent four-electron reduction. [43] A composite of Ag/Mn_3O_4 obtained via pyrolysis yielded a calculated *n*-value of 3.97 e^-, and was determined to be more stable than Pt/C when subjected to accelerated aging studies. [44]

Alternatively, catalytic activities can be enhanced through facile post-treatment processes that induce oxygen vacancies in a given material. Recently, it was shown that the performance of β-MnO_2 could be improved through controlled calcination processes, which introduced oxygen defects to the surface. When O_2 is bound to the surface defect, the O-O bond is elongated and activated, and the kinetic barriers are lowered. [45] Also, the inclusion of conductive additives, such as commercially available carbons or graphene, is another technique proven to achieve enhancement of the catalytic character. [19, 23, 24, 41, 46-48]

2.5 Preparation of Manganese Oxide-Carbon Composites

Commercially available conductive carbons have been utilized in composite catalysts for some time, including catalysts in which these carbons are paired with manganese oxides. [23, 28, 41, 49] However, while these investigations did demonstrate the fact that the conductivity of the composite is improved upon the addition of commercial carbonaceous species, graphene, a network of sp^2 hybridized carbons, is also garnering significant attention in electrochemical applications. The high surface area, superior electron mobility, and tailorable surface properties of graphene make this material of interest for catalytic applications. [50] In order to achieve a true synergistic effect from a composite catalyst, the interactions between the ceramic material and graphene must be maximized so as to ensure that the entirety of the ceramic material is rendered electrochemically active while still being augmented by the conductive graphene component. Studies investigating MnO_x-graphene composite materials have addressed this through varied synthetic routes aimed at attaining optimized interactions between the active ceramic component and the conductive graphene.

Several groups have demonstrated an *in situ* preparation in which nanostructured MnO_x is grown directly on reduced graphene oxide (RGO). RGO commonly finds application as the graphene component of composite or hybrid catalyst materials due to its surface area (100-400 m^2/g) and conductivity. The primary synthetic route that is utilized to obtain RGO is a modified Hummers method [51, 52] in which graphite powder is oxidized, yielding graphene oxide (GO), which is then chemically reduced. [53] The commonly used Mn-containing precursors are $KMnO_4$ or $MnSO_4 \bullet H_2O$, and are typically introduced after the graphene has been dispersed in solution. [46, 54, 55] Modified routes to

activated graphene-ceramic composites have also been employed - specifically, calcination of GO under N_2 to yield graphene nanosheets with $KMnO_4$ as ceramic precursor, [54] polymer-assisted chemical reduction of GO with $MnSO_4 \bullet H_2O$, [55] and ionic-liquid functionalization of GO followed by hydrazine reduction with $NaMnO_4$ as precursor. [47]

For each *in situ* preparation, the formation of the hybrid material is dependent upon certain interactions between the graphene and the Mn-containing precursor. Feng *et al.* report the preparation of a hybrid catalyst comprised of Mn_3O_4 grown on GO coupled with mildly oxidized multi-walled carbon nanotubes. [46] As demonstrated by SEM, the Mn_3O_4 nanoparticles are clearly coupled to the GO as a result of the *in situ* technique; the functional groups residing on the GO promote nucleation and a distinctly controlled formation of nanoparticles that are approximately 11 nm in size. [46]

The polymer-assisted route, yielding ceramic nanoparticles that are approximately 10-20 nm in size in the obtained composite MnO_2/RGO, obtains similar results. In this synthesis, poly(sodium 4-styrene sulfonate (PSS), functions to promote the solubility of the graphene and improves the interactions between the Mn^{2+} and the graphene, ultimately enabling the growth of MnO_2. [55] The synthetic procedure involving the ionic liquid (IL) functionalized graphene material relies upon a reaction at the carboxylic acid groups on GO to obtain the functionalized species. This process demonstrates improved electronic conductivity for the GO-IL material, and later promotes the favorable electrostatic interactions with the Mn-containing precursor. [47] Cao *et al*. has shown the growth of α-MnO_2 nanorods approximately 50-80 nm long and ~10 nm in diameter on

graphene nanosheets. The growth is facilitated by the electrostatic interactions between the Mn^{2+} and the oxygen-containing groups on the oxidized graphene nanosheets. [54]

In situ techniques are often selected in order to attain optimum, synergistic interactions between the ceramic and graphene that are considered unachievable by simple mixing techniques. While some groups do demonstrate that their hybrid composites are preferable to simple mixtures, [46, 54] it has also been shown that highly active, uniform blends can be attained through straightforward preparations. Previous work done in our laboratories in the Lambert group demonstrated that a simple sonication protocol performed with a graphene-like carbon scaffold (termed GLC) and α-MnO_2 nanowires doped with nickel or copper afforded a highly active catalyst material in which the doped α-MnO_2 nanowires appear by SEM to be uniformly dispersed throughout the GLC. [24] One such advantage of such a preparation is the ease with which multiple blends may be prepared and subsequently assessed; therefore, the optimal blend composition yielding the greatest current density could be determined (20% Ni-α-MnO_2 and 80% GLC). [24]

2.6 Electrochemical Analysis of Composite Catalysts

In addition to enhancing the conductivity of the catalyst, graphene also improves the efficiency of ORR catalysis as suggested by the calculated *n*-value, though the exact mechanism of oxygen reduction on composite materials has yet to be elucidated. The majority of efforts reporting an *n*-value claim a value of approximately four electrons, which is the nominal value. A summary of notable data for MnO_x-graphene composites is given in Table 2.1.

Table 2.1: Comparison of ORR Data for MnO_x-Graphene Composites

Author **Ref.**	**Preparation of Composite**	**Composite Description**	**Electrolyte**	**n-value (Potential Range)** ***Technique***	**Onset Potential** ***Half-Wave Potential***	**Other Data of Interest**
Feng 46	*in situ*	Mn_3O_4/Nano-C	1 M KOH	3.9 (-0.151 to -0.301 V) 3.7 (-0.601 V) *RRDE*	Onset not presented *-0.191 V (Pt/C -0.171 V)*	Reduction Peak Potential = -0.181 V at 5 mV/s (Pt/C -0.151 V)
Lambert 24	simple mixing protocol	Cu-α-MnO_2 / GLC and Ni-α-MnO_2 / GLC	0.1 M KOH	3.9 ± 0.2 (avg. -0.280 to -0.530 V) *RDE*	-0.042 V *- 0.189 V (Comparable to Pt/C)*	Kinetic rate constant = 3.50×10^{-2} cm s^{-1} compared to 3.24×10^{-2} cm s^{-1} for Pt/C; Blend is tolerant to MeOH crossover
Lee 47	*in situ*	rGO-IL/Mn_3O_4 (10:1) rGO-IL/Mn_3O_4 (2:1)	0.1 M KOH	3.50 (avg. -0.330 to -0.530 V) 2.75 (avg. -0.330 to -0.530 V) *RDE*	estimated at -0.030 V estimated at -0.070 V *Approximated to be -0.180 V from LSV*	rGO-IL/Mn_3O_4 (10:1) has comparable power density to commercial cathode when implemented in Zn-air cell
Wu 56	layered on electrode surface	α-MnO_2 on graphene	0.1 M KOH	K-L slope ~4 (- 0.455 V) *RDE*	Data not presented	Catalytic durability: 3.2 mA/cm^2 = current density for composite electrode after 10Ks of running time

Reference potentials have been converted to V vs. Standard Calomel Electrode.

Relevant comparisons to Pt/C are provided for studies that presented this data.

In addition to the well-established fact that MnO_x catalysts are capable of efficient peroxide decomposition, [23] it is also known that *n* is highly dependent upon the applied overpotential, [46] and this conclusion appears to be true for composite electrodes as well. Wu *et al*., who prepared a layered electrode of MnO_2 on GO, corroborates that the four-electron reduction can be achieved at lower overpotentials. [56] Results obtained by Lee *et al*. with Mn_3O_4 grown on functionalized rGO (rGO-IL/Mn_3O_4) show that, by applying the Koutecky-Levich equation to RDE data, n = 3.5 could be obtained with a composite containing more rGO (prepared in a 10:1 weight ratio of rGO-IL to Mn precursor). Conversely, a composite that contains more Mn_3O_4 (2:1 reactant ratio rGO-IL to Mn precursor) gives n = 2.75. [47] The authors attribute this to the two possible reaction pathways (a quasi-four-electron transfer and the two-step, two-electron path), and speculate that the reaction mechanism (and thus, the *n* value) can be tuned by the amount of ceramic in the composite. The Mn_3O_4/Nano-C hybrid containing GO and mildly oxidized multi-walled carbon nanotubes as prepared by Feng *et al*. is 67% Mn_3O_4, and gave n = 3.9 at low overpotentials and 3.7 at higher overpotentials, as determined by the RRDE method. This technique also revealed that the peroxide produced by this hybrid varies from 5% at low overpotentials to ~15% at a high overpotential. [46] The manually blended Cu-α-MnO_2 (20%) / GLC (80%) catalyst prepared by Lambert *et al.* yielded n = 3.9 ± 0.2, and corroborated that more peroxide is generated at higher overpotentials. [24]

For the papers that describe MnO_x-graphene composite materials, only two authors (Lambert and Lee) present onset potentials for their novel hybrids. [24, 47] For the sake of comparison, all potentials have been converted to the standard calomel electrode (SCE). The rGO-IL/Mn_3O_4 composites prepared by Lee *et al.* at the ratios of rGO-IL:Mn

equal to 10:1 and 2:1 give onsets of approximately -0.030 V and -0.070 V, respectively. [47] Clearly, the 10:1 composite (determined to be 19.2% Mn) possesses an evident synergistic effect with respect to the onset potential, as the onset of rGO-IL is determined to be roughly equivalent to the 2:1 composite (52.5% Mn). Despite the higher carbon content of the 10:1 composite, the onset is 40 mV more positive, indicating that less energy has to be invested in the system to generate reductive current. Similarly, Lambert *et al.* show that the onset potential for the Ni-α-MnO_2 / GLC blend is -0.042 V, which is a value within the range obtained with Lee's composites. [24] In addition, they demonstrate that the onset is a tunable parameter that can be adjusted with the amount of Ni-α-MnO_2 incorporated into the blend.

Half-wave potentials for composite catalysts are provided for only two composites: Mn_3O_4/Nano-C (-0.191 V) [46] and the Cu-α-MnO_2 / GLC blend (-0.189 V). [24] A half-wave potential can be approximated from LSV curves for rGO-IL/Mn_3O_4 10:1 composite (-0.180 V). [47] For an extensive comparison of half-wave potentials of manganese oxides and manganese oxides blended with commercial conductive carbons, see the electronic supplementary material from Feng *et al.* [46]

Feng *et al.* performed a thorough assessment of reduction-peak potentials by CV for the Mn_3O_4/Nano-C hybrid as compared to the Mn_3O_4 and Nano-C alone, as well as their physical mixture.[46] Also insightful is the comparison they present for 20% Pt on Vulcan from E-Tek. The hybrid material affords a peak potential of -0.181 V, which is more positive than the ORR peak potentials observed when the Mn_3O_4 and Nano-C materials are tested alone, or when they are manually blended together. However, the demonstrated peak potential for the hybrid material is less positive than Pt/C, for which

the observed peak potential was -0.151 V. Similarly, the current densities obtained at 5 mV/s and 1600 rpm at varied catalyst loadings do not exceed -3 mA/cm^2, while Pt/C yields a current density of nearly -4 mA/cm^2.

Results presented by Lambert *et al*. demonstrate a remarkable tolerance to methanol crossover by the 20% Ni-α-MnO_2 / 80% GLC composite catalyst as compared to Pt/C. Specifically, the addition of 2 weight percent methanol into the electrochemical cell triggered a 60% decrease in current for Pt/C; conversely, the blended composite demonstrated a stable amperometric response with a mere 5% decrease in current. In addition, the kinetic rate constants for the 20% Ni-α-MnO_2 / 80% GLC composite and Pt/C are shown to be comparable (3.50×10^{-2} cm/s and 3.24×10^{-2} cm/s, respectively). [24]

Two studies employed their composite catalysts in battery applications. The rGO-IL/Mn_3O_4 (10:1) composite prepared by Lee *et al*. was employed in a Zn-air full cell and was shown to perform better than the commercial air cathode under the current density range from 0 to 200 mA/cm^2. [47] The catalytic activities of the hybrid material comprised of α-MnO_2 nanorods and graphene nanosheets (α-MnO_2/GN hybrid) prepared by Cao *et al.* was tested in LiO_2 batteries. The hybrid material delivered a higher reversible capacity under galvanostatic charge/discharge experiments than the mixtures of α-MnO_2 and graphene nanosheets prepared via ball milling. In addition, the hybrid also demonstrated stable reversible capacities when the cycling stability was assessed. [54]

2.7 Conclusions

Ultimately, much of the work done thus far to investigate catalysts based on manganese oxide, both as independent catalyst materials and in hybrid composites with graphene, demonstrates the promise that these materials hold for effective implementation as oxygen reduction catalysts. Considering that manganese oxide based catalysts are affordable, environmentally friendly, and catalytically active, continued investigations in this regime of research are warranted. Continued advances toward optimizing these catalyst systems could lead to the development and widespread utilization of improved electrochemical devices that employ highly active manganese oxides as a catalyst material. One technique proven to enhance the catalytic performance of α-MnO_2 is the addition of transition metal dopant species, such as Ni and Cu. [24] Chapters 3 and 4 will discuss my efforts to synthesize and characterize Cu- and Ni-doped α-MnO_2 nanowires to gain a more thorough understanding of the role of the dopant species in ORR catalysis.

Chapter 3

Elucidating the Role of Cu-dopants in α-MnO_2 Nanowire Electrocatalysts for the Oxygen Reduction Reaction in Alkaline Media

3.1 Introduction

The synthesis of transition metal oxides is of interest for applications in energy storage and conversion. [1, 28] Manganese oxides have been extensively studied for their performance to catalyze the ORR, a critical reaction that occurs in fuel cells and metal air batteries. While our previous study of Cu-α-MnO_2 nanowires demonstrated improved catalytic performance relative to undoped α-MnO_2, a more thorough understanding of the role of Cu-dopants in catalysis was desired. [24] This study consisted of the synthesis, characterization, and electrochemical evaluation of Cu-α-MnO_2 nanowire catalysts containing varied levels of Cu-dopant. To our knowledge, this is the first study that correlates the physicochemical properties of Cu-α-MnO_2 nanowires to the demonstrated electrocatalytic behavior.

3.2 Experimental

3.2.1 General

All chemicals were obtained commercially and used as received, without further purification. $MnSO_4 \cdot H_2O$ and $Cu(NO_3)_2 \cdot 3H_2O$ were purchased from Alfa Aesar. $KMnO_4$, isopropanol, and Nafion solution (5 wt. % solution in water and lower aliphatic alcohols) were used as received from Sigma-Aldrich.

3.2.2 Synthesis

The synthesis of Cu-α-MnO_2 nanowires was performed via a modified hydrothermal reaction in an acid digestion bomb (PTFE liner, 45 mL capacity, Parr™ reactor), adapted from a previously published synthesis for α-MnO_2 and described in our previous studies. [19, 24] Solutions of $MnSO_4 \cdot H_2O$ (0.2 g, 1.18 mmol), $KMnO_4$ (0.5 g, 3.16 mmol) and a specified amount of $Cu(NO_3)_2 \cdot 3H_2O$ in deionized water were heated in the acid digestion bomb at 140 °C for 120 hours to ensure nanowire morphology. $Cu(NO_3)_2 \cdot 3H_2O$ was added in specific molar ratios to the manganese-containing precursor of 1:1, 1:0.5 and 1:0.25 (Mn:Cu) to achieve different copper doping levels. Undoped α-MnO_2 was obtained by a hydrothermal reaction that excluded the copper precursor. [19, 24] Following heating for 120 hours at 140 °C, all reactions were cooled to room temperature, and the solids were isolated by centrifugation (3000 rpm). The solids were washed with deionized H_2O (4x, 10 mL) and ethanol (4x, 10 mL), isolated via centrifugation, and dried in a vacuum oven overnight at 65 °C.

3.2.3 Materials Characterization

Powder X-ray Diffraction (PXRD). Catalyst powders were mounted directly onto a zero background holder purchased from The Gem Dugout. Samples were scanned at a rate of 0.02°/2 s in the 2θ range of 10-80° on a Bruker D8 Advance Diffractometer in Bragg-Brentano geometry with Cu Kα radiation and a diffracted beam graphite monochromator; extended scans (12 hour scan time) were performed at a rate of 0.0240°/15 s in the range of 10-80°. Phase identification was achieved through use of the Jade 9.0 software suite and the Joint Committee on Powder Diffraction Standards (JCPDS). Diffraction peak positions were determined by profile fitting of peak profiles

within the program Jade 9.0 using a pseudo-Voigt profile function. Using these peak positions, lattice parameters were then derived using a least-squares refinement procedure embedded within the Jade 9.0 software. Initial values of the unit cell were input based on the α-MnO_2 structure (JCPDS file number 00-44-0141).

Transmission Electron Microscopy (TEM). TEM analysis was carried out on a JEOL 2010F electron microscope at 200kV acceleration voltage. Energy Dispersive Spectroscopy was collected using its attachment of Oxford Instruments ISIS/Inca System with Oxford Pentafet Ultrathin Window Detector (UTW).

Scanning Electron Microscopy (SEM). The samples were dispersed onto carbon tape and imaged using a Zeiss Supra 55VP field emitter gun scanning electron microscope (FEGSEM). Samples were sputter coated with gold-palladium prior to analysis. A Noran Energy Dispersive X-Ray Spectroscopy (EDS) detector and Noran System Six software were used for the acquisition of the EDS spectra. EDS data were plotted with Kaleidagraph software for presentation purposes. Samples were sputter coated with gold-palladium prior to analysis.

Brunauer-Emmett-Teller (BET) Surface Area Analysis. Gas sorption experiments were performed on an Autosorb iQ2-Chemi instrument (Quantachrome Instruments, Boynton Beach FL, USA) at 77 K (liquid nitrogen temperature) using ultra-high purity (UHP) nitrogen as adsorbate. Specimens were degassed at 140 °C for between 2 and 3 hours (the exact degas time was determined automatically based upon periodic evaluation of rate of gas evolution from each specimen). The specimen cells were quartz glass with a 9 mm outer diameter, and filler rods were inserted to reduce

dead volume above the sample. Cell volumes were determined prior to each run using ultra-high purity helium.

Isotherms were typically measured using 40 adsorption points and 40 desorption points, with an optional 30 additional adsorption points in the micropore range. Surface areas were calculated using the Brunauer-Emmett-Teller (BET) method using seven adsorption points in the range P/P_0 = 0.05 to 0.3. Total pore volumes were calculated based on the total gas adsorbed at P/P_0 values of 0.996. Pore sizes were determined using the Barrett-Joyner-Halenda (BJH) method during the desorption branch of the isotherm, ignoring P/P_0 points below 0.35.

X-ray Photoelectron Spectroscopy (XPS). X-ray photoelectron spectroscopy (XPS) was performed with a Kratos Axis Ultra Delay-Line Detector (DLD) instrument with base pressures less than 5×10^{-9} Torr. Powder samples were pressed into carbon tape for analyses. No interferences from the carbon tape were observed. Charge neutralization was not required; however, the neutralizer was used for all samples to ensure that differential charging did not influence the spectral lineshapes. XPS was performed with a monochromatic Al-Kα (1486.7 eV) source operated at 150 W with an elliptical spot size of 300x700 microns. Survey spectra were taken with a pass energy of 80 eV, 600 meV step, and 100 ms dwell times. With Al-Kα X-rays, the Mn LMM Auger transition overlaps with the Cu 2p core-level peaks, so XPS was also performed with a non-monochromatic Mg X-ray source (1253.6 eV) operated at 180 W. The energy resolution is lower with the non-monochromatic source, so step sizes were 800-1000 meV for survey spectra. XPS with the Mg source was helpful for resolving the Cu 2p peaks on a relatively flat background. High resolution spectra were recorded with a 20

eV pass energy, 200 ms dwell time, and step sizes ranging from 30-50 meV (100 meV for Mg X-ray XPS). Data processing was performed with CasaXPS. Quantifications were performed using the built-in relative sensitivity factors. Mn 3s peak fitting was performed with a linear background and two unconstrained Gaussian/Lorentzian (70/30) peaks.

3.2.4 Electrochemical Studies

Oxygen reduction studies were performed using rotating disk electrode and rotating ring disk electrode assemblies. Catalyst inks consisting of 5.0 mg of catalyst material, 200 µL isopropanol, and 300 µL Nafion solution were sonicated for approximately 20 minutes. For RDE, a 5 µL aliquot was drop-cast on a glassy carbon RDE electrode (BASi, active area= 0.0788 cm^2). For RRDE, 10 µL of the prepared ink was drop-cast onto the glassy carbon disk, surrounded by a platinum ring electrode (Pine, disk area = 0.2475 cm^2, ring area = 0.1866 cm^2). Prior to each drop-coating process, the RDE or RRDE glassy carbon electrode surface was polished with 0.05 µm alumina slurry and rinsed with deionized water and ethanol.

Linear Scanning Voltammograms were executed in a potential window from 0.2 V to -0.6 V (V vs. Ag/AgCl) at a scan rate of 1 mV/s. For RDE, LSVs were run at rotation rates of 500, 900, 1600, 2500, and 3600 rpm. For RRDE, LSVs were obtained at 500 and 2500 rpm in a potential window from 0.2 V to -0.6 V, and the reference was Hg/HgO. The collection efficiency of the ring electrode (*N*) was determined to be 37%.[6, 14] All experiments were run in 0.1 M KOH electrolyte that had been thoroughly purged with ultra-high purity oxygen (or ultra-high purity nitrogen for background

measurements) prior to each run. The appropriate gaseous atmosphere was preserved via blanketing for the duration of the experiment.

RDE experiments were performed in a three-electrode cell, manufactured by Bioanalytical Systems, Inc. connected to a Versastat 4 potentiostat operated by VersaStudio software. Electrodes (BASi) included the glassy carbon working electrode prepared as previously described, a Pt coil counter electrode, and a Ag/AgCl reference electrode (3 M NaCl, potential = 0.209 V vs. NHE). RRDE experiments were performed in a three-electrode cell, manufactured by Gamry Instruments connected to a Gamry Series G 750 Test System Bipotentiostat. Electrodes included the Gamry RDE710 rotating working electrode prepared as described, Pt foil as the counter electrode, and a Hg/HgO reference electrode (Hach, 0.1 M KOH, potential = 0.171 V vs. NHE).

3.3 Results and Discussion

3.3.1 Synthesis and Characterization

It has been previously demonstrated that α-MnO_2 nanowires contain the most active crystalline phase and morphology, respectively, for manganese oxide nanostructures utilized for the ORR in alkaline electrolyte. [19, 24] The modified hydrothermal method utilized in this study was selected with the goal of synthesizing Cu-doped α-MnO_2 nanowires. Therefore, the first characterization techniques utilized in this study were scanning electron microscopy (SEM) and powder X-ray diffraction (PXRD). The hydrothermal syntheses previously described yielded nanowires at all reactant ratios, as shown in the SEM images in Figure 3.1 a-c. The crystalline phase was determined by

PXRD to be exclusively α-MnO_2 (JCPDS file number 00-44-0141), Figure 3.1 d-f, indicating that the phase was retained upon attempted doping with Cu.

Initially, the presence of copper in the samples was confirmed and qualitatively approximated by energy-dispersive X-ray spectroscopy (EDS) obtained via scanning electron microscopy (SEM), Figure 3.2 a-c. As a preliminary comparison, a ratio of the intensities of the Mn K_β line at ~6.49 keV and the Cu K_α line at 8.04 eV revealed that an increased amount of Cu precursor in the reaction correlated to an increased amount of Cu in the sample. Ratios trended from I_{Cu}:I_{Mn} = 0.433, 0.401 to 0.303 for the 1:1, 1:0.5 and 1:0.25 (Mn:Cu) reactions, respectively.

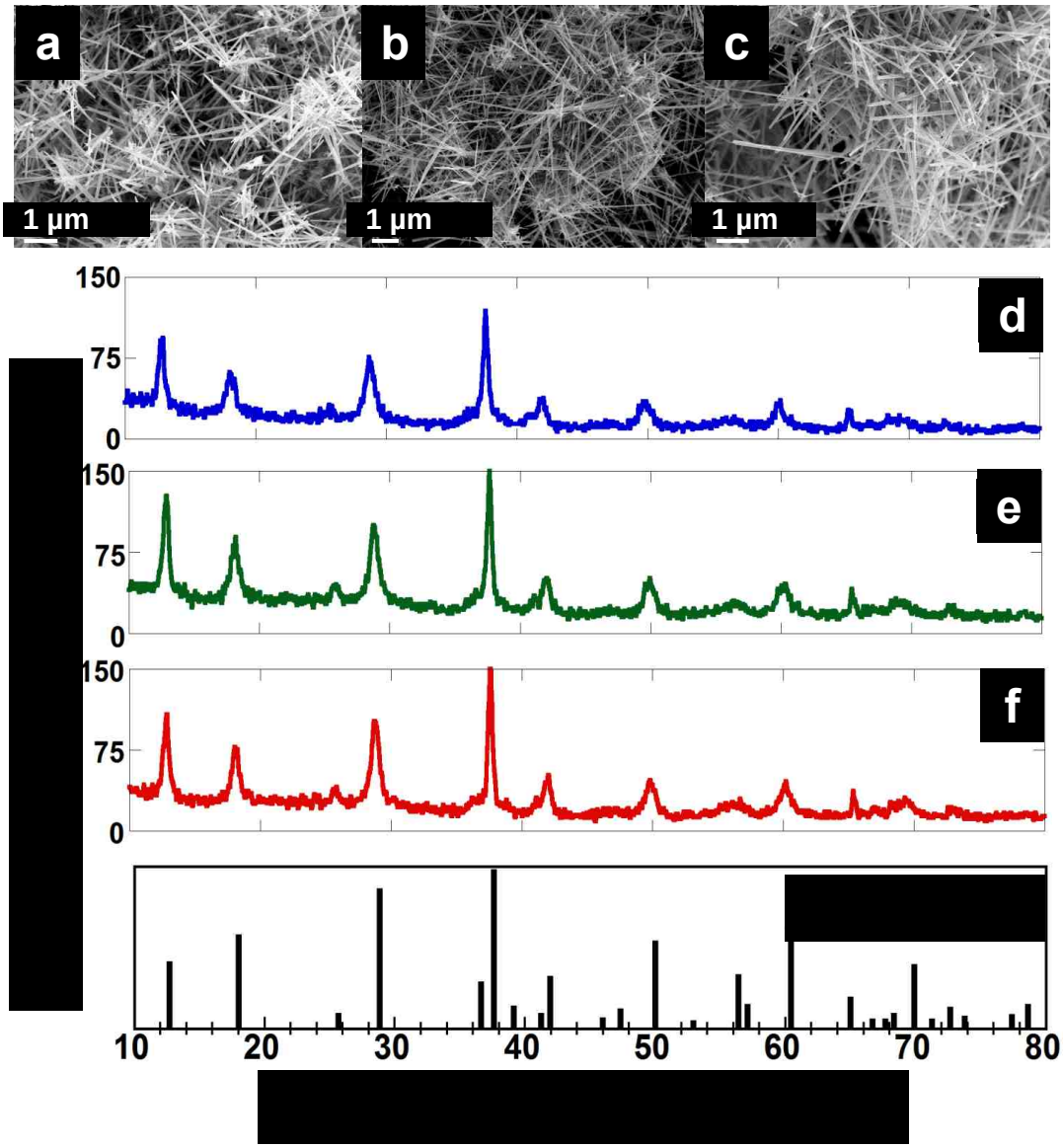

Figure 3.1: Characterization data for the synthesized Cu-doped α-MnO_2 nanowires. a-c) SEM images of the nanowires synthesized at a Mn:Cu ratio of 1:1, 1:0.5, and 1:0.25, respectively. d-f) XRD patterns for Cu-α-MnO_2 nanowires synthesized at a Mn:Cu ratio of 1:1, 1:0.5, and 1:0.25, respectively.

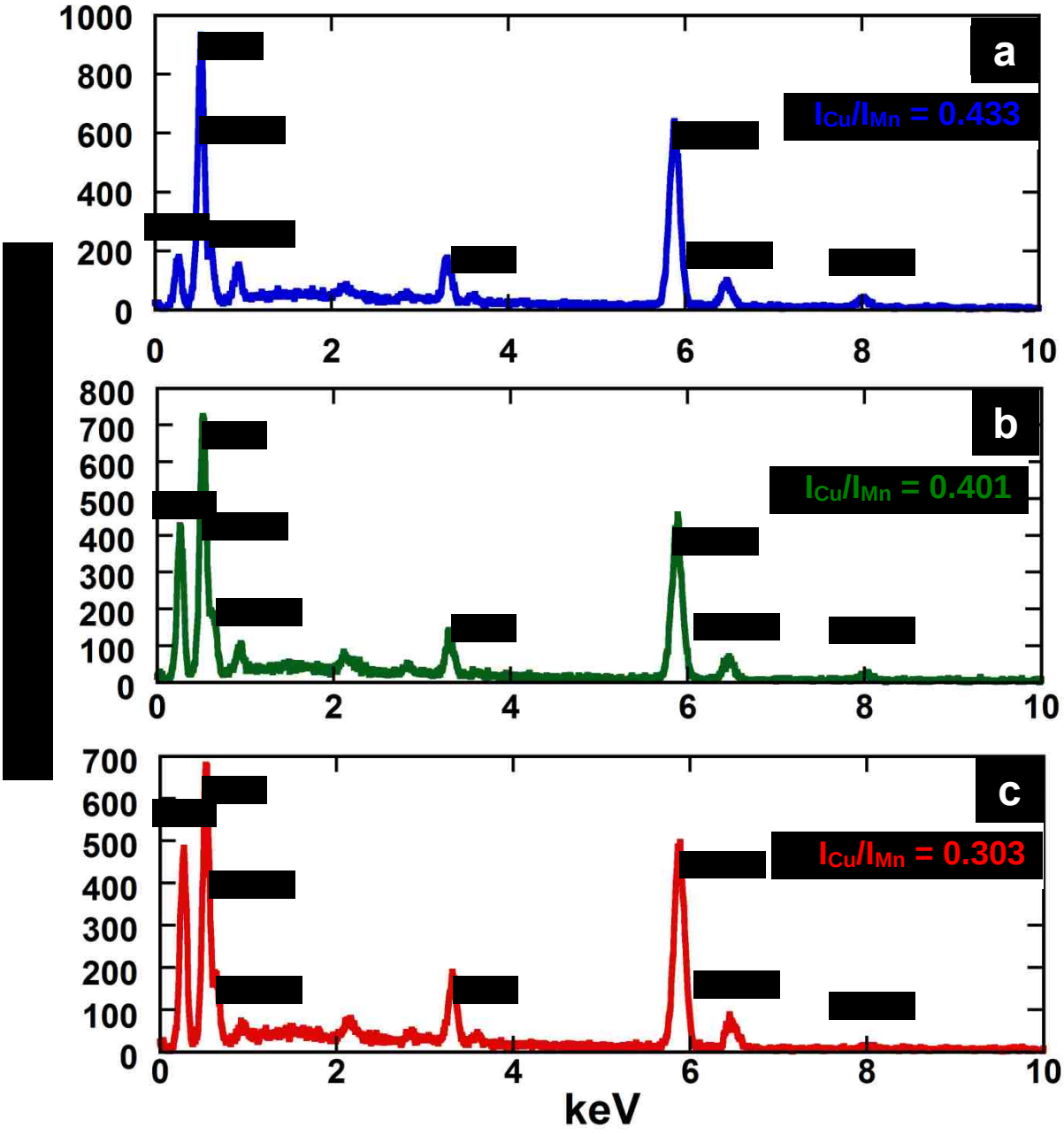

Figure 3.2: EDS spectra obtained by SEM for nanowires prepared at varying precursor ratios a) Mn:Cu ratio of 1:1, b) 1:0.5, and c) 1:0.25. The ratios of the relative intensities of the Cu K_α and Mn K_β peaks (labeled in bold) are noted.

Quantitative measurement of the copper content of each sample was obtained by EDS performed via transmission electron microscopy (TEM), as shown in Tables 3.1, 3.2, and 3.3; average atomic percentages and the corresponding standard deviations are included as well. The sample synthesized at the initial reactant ratio of 1:1 (Mn:Cu) contained 9.31 ± 2.35% Cu. The sample prepared at the reactant ratio of 1:0.5 (Mn:Cu) contained 7.79 ± 0.92% Cu, and the sample prepared at the reactant ratio of 1:0.25 (Mn:Cu) contained 7.55 ± 1.52% Cu.

Table 3.1: EDS Measurements of Atomic Percent Content of Cu-α-MnO_2, prepared at reactant ratio 1:1, Mn:Cu

	Cu	**Mn**	**O**	**K**
Cu-α-MnO_2	11.44	37.08	49.51	1.98
	7.72	39.84	49.19	3.25
	7.79	39.77	49.19	3.25
	8.02	39.73	49.25	3.01
	13.62	36.34	49.98	0.06
	13.25	36.71	49.99	0.05
	7.52	40.16	49.23	3.09
	8.3	39.84	49.38	2.48
	8.39	39.73	49.37	2.5
	7.06	40.51	49.19	3.25
AVERAGE	9.31	38.97	48.43	2.29
STD. DEV.	2.35	1.51	0.29	1.19

Table 3.2: EDS Measurements of Atomic Percent Content of Cu-α-MnO_2, prepared at reactant ratio 1:0.5, Mn:Cu

	Cu	Mn	O	K
Cu-α-MnO_2	8.38	39.19	49.19	3.24
	8.22	39.96	49.39	2.43
	7.49	40.46	49.32	2.74
	8.02	39.99	49.34	2.64
	9.82	37.51	49.11	3.56
	6.93	40.28	49.07	3.72
	6.13	40.62	48.92	4.33
	7.88	39.57	49.15	3.4
	7.36	39.83	49.06	3.74
	7.62	39.94	49.19	3.25
AVERAGE	7.79	39.74	49.17	3.31
STD. DEV.	0.92	0.84	0.14	0.55

Table 3.3: EDS Measurements of Atomic Percent Content of Cu-α-MnO_2, prepared at reactant ratio 1:0.25, Mn:Cu

	Cu	Mn	O	K
Cu-α-MnO_2	5.32	41.02	48.78	4.87
	6.54	41.42	49.32	2.71
	7.76	42.14	49.97	0.14
	7.43	42.48	49.97	0.12
	7.93	41.96	49.96	0.16
	8.45	41.45	49.97	0.13
	4.61	41.59	48.73	5.08
	9.2	40.28	49.83	0.68
	9.26	40.21	49.82	0.71
	8.95	37.73	48.9	4.41
AVERAGE	7.55	41.03	49.53	1.90
STD. DEV.	1.52	1.30	0.51	2.03

X-ray photoelectron spectroscopy (XPS) was used to analyze the percent composition at the surface of the nanowires. The Cu atomic concentration at the surface was found to be much lower than the Cu content of the nanowires measured by EDS, as demonstrated in the XPS data shown in Table 3.4. Because XPS is a surface-sensitive technique that probes a sample depth of approximately 10 nm whereas EDS analyzes the bulk, the notable differences between the EDS and XPS data can be rationalized.

Table 3.4: Atomic Percentage of Cu as Measured by XPS
Percentages obtained by EDS are included for comparison.

Sample (Mn:Cu Ratio)	Atomic % Cu (XPS)	Atomic % Cu (EDS)
α-MnO_2	0%	0%
Cu-α-MnO_2 (1:0.25)	0.31%	7.5%
Cu-α-MnO_2 (1:0.5)	0.42%	7.8%
Cu-α-MnO_2 (1:1)	0.50%	9.3%

XPS was also utilized to gain a more thorough understanding of the oxidation states of the Mn ions within the Cu-α-MnO_2 catalysts; the data is presented in Figure 3.3. The difference in binding energies between the Mn 3s peaks can be used to approximate the oxidation state, as shown in Figures 3.3 and 3.4. As the amount of Cu in the sample increases, the extent of splitting between the Mn 3s peaks becomes greater, indicating that more Mn^{3+} is present. [57, 58] The greatest splitting value (4.589 eV) was observed for the Cu-α-MnO_2 sample determined to contain 0.5% Cu at the surface; in comparison, the observed Mn 3s splitting for the undoped α-MnO_2 sample was determined to be 4.445 eV. Figure 3.4 and accompanying data in Table 3.5 show that as the amount of surface Cu-dopant increases, the splitting between the Mn 3s peaks (ΔBE) increases slightly.

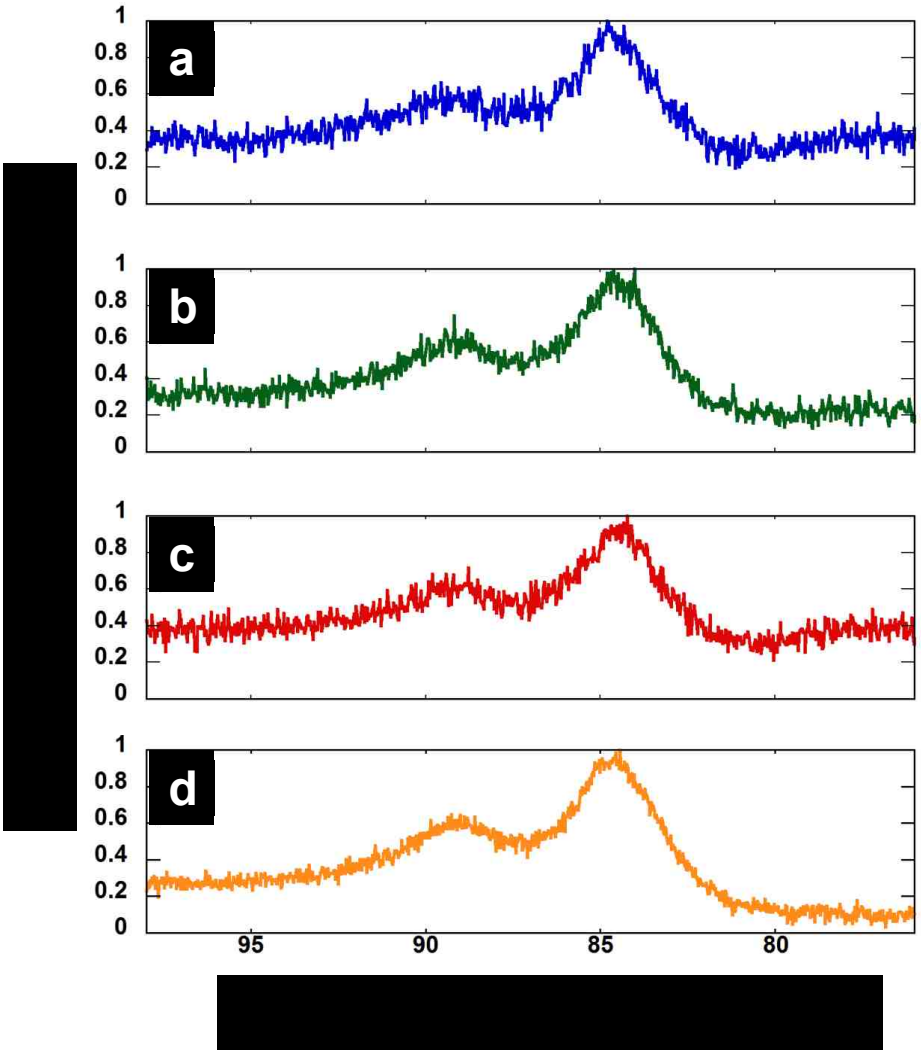

Figure 3.3: XPS data showing the splitting of the Mn 3s peaks a) 9.3% Cu, 0.50% Cu at surface, b) 7.8% Cu, 0.42% Cu at surface, c) 7.5 % Cu, 0.31% Cu at surface, and d) undoped α-MnO_2.

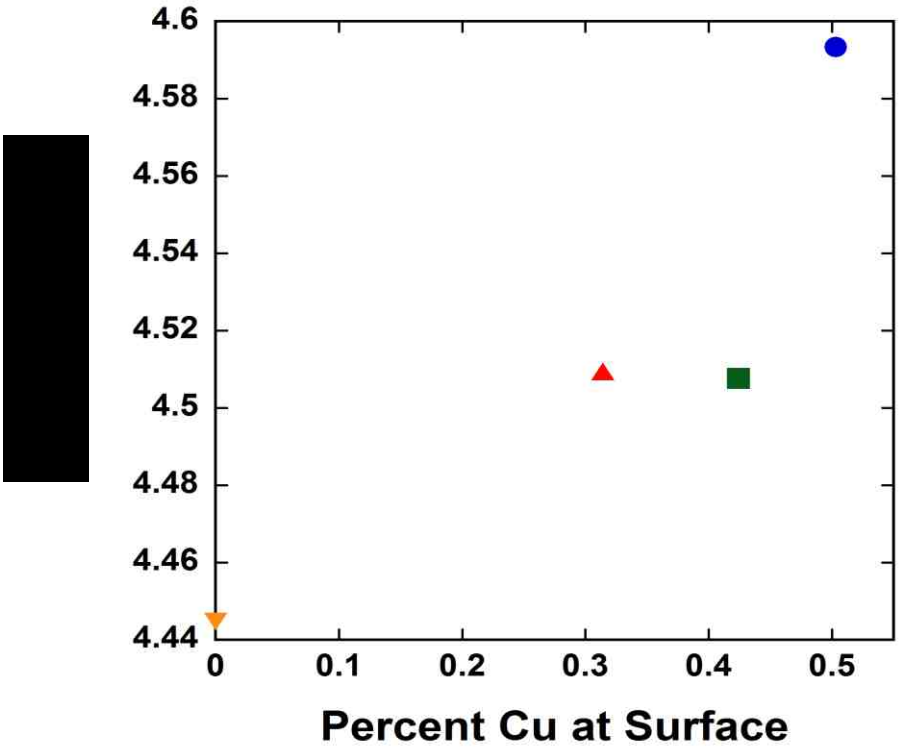

Figure 3.4: The splitting of the Mn 3s peaks (ΔBE, eV) plotted as a function of the percent Cu measured at the surface by XPS.

Table 3.5: Splitting of Mn 3s Peaks as Observed by XPS

Sample (Symbol)	Atomic % Cu (XPS)	ΔBE (eV)
α-MnO_2 (▼)	0%	4.445
Cu-α-MnO_2 (▲)	0.31%	4.523
Cu-α-MnO_2 (■)	0.42%	4.495
Cu-α-MnO_2 (●)	0.50%	4.589

The surface areas, average pore diameters, and pore volumes of the Cu-α-MnO_2 powders were analyzed using the Brunauer-Emmett-Teller (BET) method and the Barrett-Joyner-Halenda (BJH) method. The results of these studies are shown in Table 3.6, and corresponding isotherm plots are provided in Figure 3.5 a-c. The sample containing 9.3% Cu was determined to have a surface area of 81.5 m^2/g, an average pore diameter of 5.9 nm, and a pore volume of 0.24 cm^3/g. The sample containing 7.8% Cu was determined to have a surface area of 78.5 m^2/g, an average pore diameter of 4.7 nm, and a pore volume of 0.18 cm^3/g. Finally, the sample containing 7.5% Cu was determined to have a surface area of 59.1 m^2/g, an average pore diameter of 4.7 nm, and a pore volume of 0.14 cm^3/g. Clearly, as more Cu is introduced into the α-MnO_2 structure, the surface area, pore size, and pore volume increase as well.

Table 3.6: BET Measurements of Cu-α-MnO_2 Nanowires

Cu-content (avg. atomic %)	**BET Surface Area (m^2/g)**	**Average Pore Diameter (nm)**	**Pore Volume (cm^3/g)**
7.5%	59.1	4.7	0.14
7.8%	78.5	4.7	0.18
9.3%	81.5	5.9	0.24

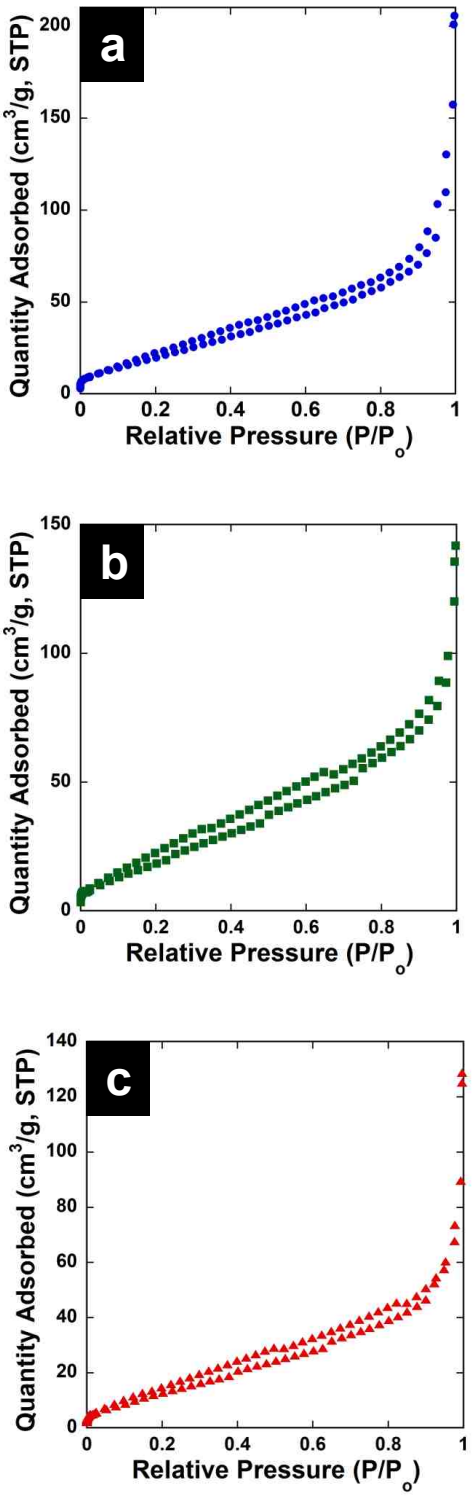

Figure 3.5: Nitrogen sorption isotherms for a) Cu-α-MnO_2, 9.3% Cu (81.5 m^2/g), b) Cu-α-MnO_2, 7.8% Cu (78.5 m^2/g), and c) Cu-α-MnO_2, 7.5% Cu (59.1 m^2/g).

Further analyses of PXRD data were pursued to determine the effects of the Cu dopant on the unit cell parameters of the α-MnO_2 lattice, Table 3.7. For the as-synthesized, undoped α-MnO_2 sample, the dimensions of the a-axis (9.836 Å), c-axis (2.858 Å), and unit cell volume (276.45 $Å^3$) were greater than the dimensions documented in JCPDS file 00-044-0141 (9.785Å, 2.863 Å, and 274.1 $Å^3$, respectively). Further expansions of the a-axis and cell volume were observed upon additional incorporation of Cu. For the sample containing 7.5% Cu, the a-axis was determined to be 9.838 Å and the c-axis was determined to be 2.859 Å, giving an overall cell volume of 276.74 $Å^3$. For the sample containing 7.8% Cu, the a-axis was determined to be 9.84 Å and the c-axis was determined to be 2.857 Å, giving an overall cell volume of 276.5 $Å^3$. For the sample containing 9.3% Cu, the a-axis was determined to be 9.866 Å, the c-axis was determined to be 2.857 Å, giving an overall cell volume of 278.12 $Å^3$. The tetragonal unit cell structure for α-MnO_2 is depicted in Figure 3.6.

Rietveld refinements for Cu-α-MnO_2 (9.3% Cu) and undoped α-MnO_2 provided information about the average Mn-O bond lengths in the [MnO_6] octahedra. The average Mn-O bond lengths in the Cu-α-MnO_2 sample (9.3% Cu) are 1.900 ± 0.010 Å. This stands in comparison to the average bond lengths in the undoped α-MnO_2, which were determined to be 1.915 ± 0.035 Å. It is hypothesized that the convergence of the Mn-O bond length on an average value of 1.9 Å can be partially attributed to Cu^{2+} ions occupying some of the metal sites.

Table 3.7: Unit Cell Parameters

Sample	Cu %	a (Å)	c (Å)	Volume (Å^3)
JCPDS 00-044-0141	0%	9.785	2.863	274.1
α-MnO_2 as synthesized	0%	9.836 (3)	2.858 (1)	276.45
Cu-α-MnO_2	7.5%	9.838 (3)	2.859 (1)	276.74
Cu-α-MnO_2	7.8%	9.84 (1)	2.857 (2)	276.5
Cu-α-MnO_2	9.3%	9.866 (5)	2.857 (1)	278.12

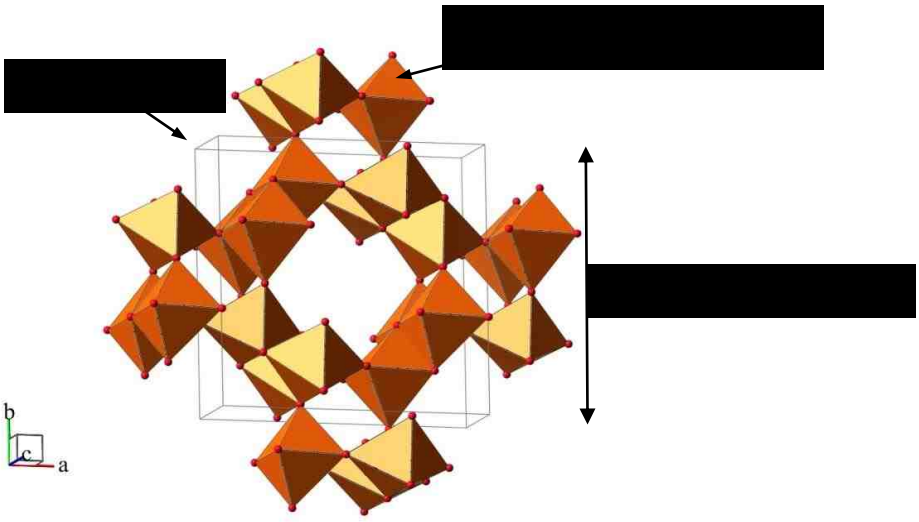

Figure 3.6: Tetragonal (I4/m) structure; [59] image courtesy of M. Rodriguez (Sandia National Laboratories)

3.3.2 Electrochemical Analysis

Films of the as-synthesized Cu-α-MnO_2 powders were prepared via a drop-cast technique in which an aliquot of the catalyst ink was deposited onto rotating disk electrodes as previously described. The electrodes were utilized for RDE studies, which enable the observation of kinetically controlled processes in the absence of mass-transfer phenomena. Figure 3.7 shows averaged linear scanning voltammograms (obtained for Cu-α-MnO_2 at 9.3% Cu (Figure 3.7 a), 7.8% Cu (Figure 3.7 b), and 7.5% Cu (Figure 3.7 c). For each individual set of data, there is an increase in the terminal current density that corresponds to an increase in the rotation rate of the working electrode. This is attributed to the change in flux of O_2 to the electrode surface that occurs as the rotation rate increases. As demonstrated by the composite plot of LSVs obtained at 2500 rpm (Figure 3.7 d), there is an observed increase in the terminal current density attained that correlates to increasing Cu-content of the catalyst. The terminal current density (-0.6 V vs. Ag/AgCl) attained by the catalyst containing 7.5% Cu was -1.93 mA/cm^2; for the catalyst containing 7.8% Cu, the terminal current density was -2.14 mA/cm^2. Finally, for the catalyst containing 9.3% Cu, the terminal current density attained was -2.82 mA/cm^2. When compared to the average terminal current density of for undoped α-MnO_2 of -1.62 mA/cm^2, it is apparent that the addition of Cu causes an increase in the terminal current density.

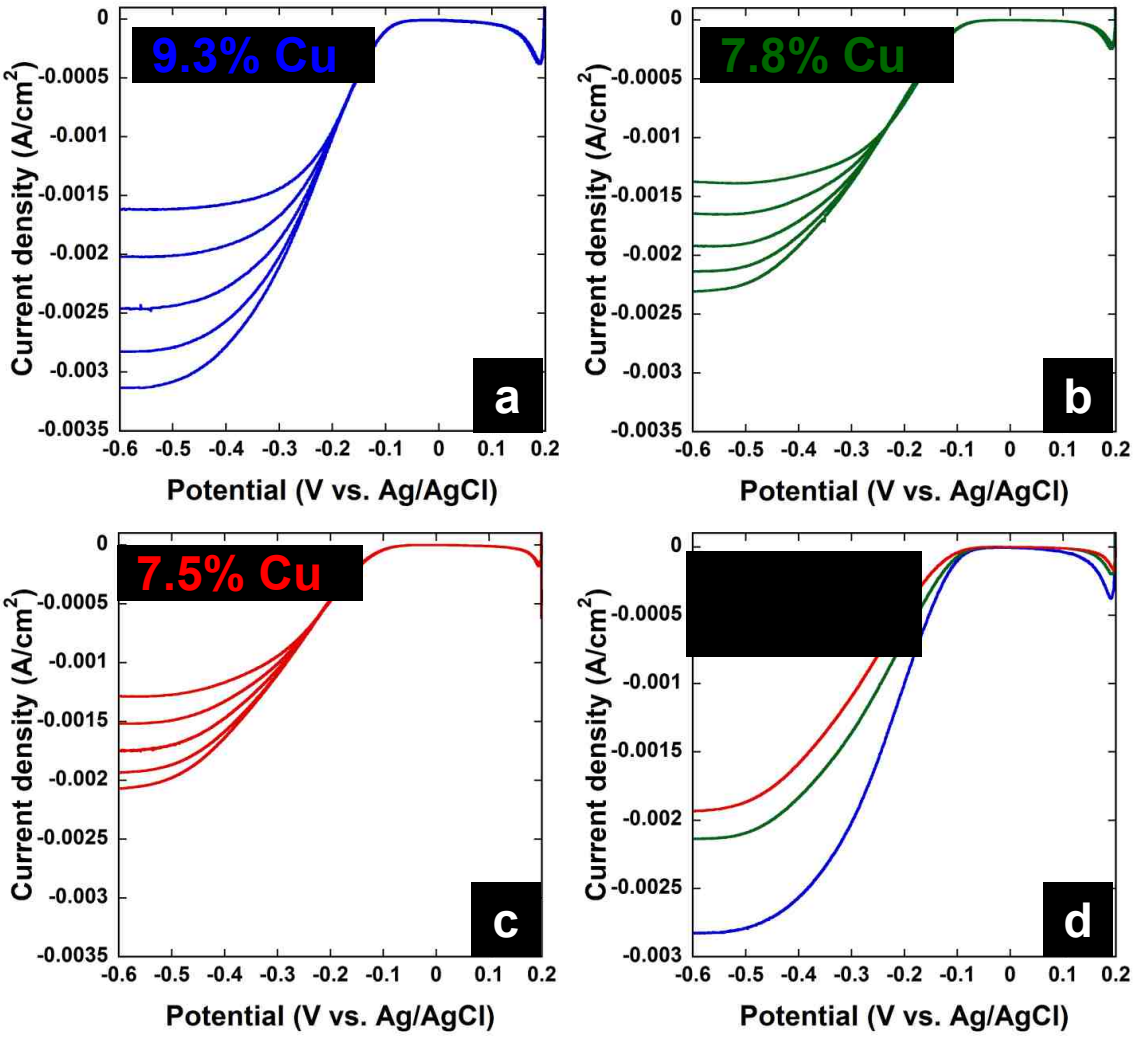

Figure 3.7: a-c) Averaged linear scanning voltammograms obtained for Cu-α-MnO_2 at 500, 900, 1600, 2500, and 3600 rpm. d) Comparative overlay of averaged LSVs obtained at 2500 rpm, revealing an increase in terminal current density that trends with Cu-content.

The linear scanning voltammograms contain a wealth of information that is useful in the comparison of various catalysts. As previously outlined in Chapter 1, the *n*-value, which is indicative of the reaction pathway that is predominant for a given catalyst, can be calculated by employing the Koutecky-Levich equation. Surprisingly, the average *n*-values calculated using the Koutecky-Levich equation revealed little difference between samples of varying Cu content. The calculated *n*-value for the Cu-α-MnO_2 sample containing 9.3% Cu was 3.20 e^-, the calculated *n*-value for the Cu-α-MnO_2 sample containing 7.8% Cu was 3.31 e^-, and finally, the calculated *n*-value for the Cu-α-MnO_2 containing 7.5% Cu was 3.28 e^-. The *n*-value for undoped α-MnO_2 of 3.1 e^- has been calculated in previous studies by Cheng *et al.* and our own group. [19, 24] Our data suggests that the presence of Cu-dopants in α-MnO_2 does cause a slight improvement in the attained *n*-value relative to undoped α-MnO_2, though there is not a significant difference in *n*-value that can be detected between Cu-doping levels ranging from 7.5% to 9.3%.

The kinetic rate constants, extracted from the y-intercept of the Koutecky-Levich plots, do indicate an increase in reaction rate that correlates with an increase in the Cu-content. This is clearly shown in Figure 3.8, which shows an overlay of the averaged Koutecky-Levich lines for each sample. The two factors of average *n*-value and reaction rate, when considered together, suggest that while the ORR mechanism is not highly influenced by the Cu-content of the α-MnO_2 catalyst, the kinetic rate constant of the reaction increases as more Cu-dopant is added. When employed as a catalyst, the Cu-α-MnO_2 containing 9.3% Cu was shown to have an average kinetic rate constant of 1.9 x 10^{-2} cm/s, the sample containing 7.8% Cu gave an average rate constant of 9.7 x 10^{-3} cm/s, and the rate constant for the sample containing 7.5% Cu gave an average rate

constant of 7.8 x 10^{-3}cm/s. When the kinetic rate constant obtained under identical conditions for α-MnO_2 is considered (7.5 x 10^{-3} cm/s), it is evident that Cu enhances the ORR kinetics.

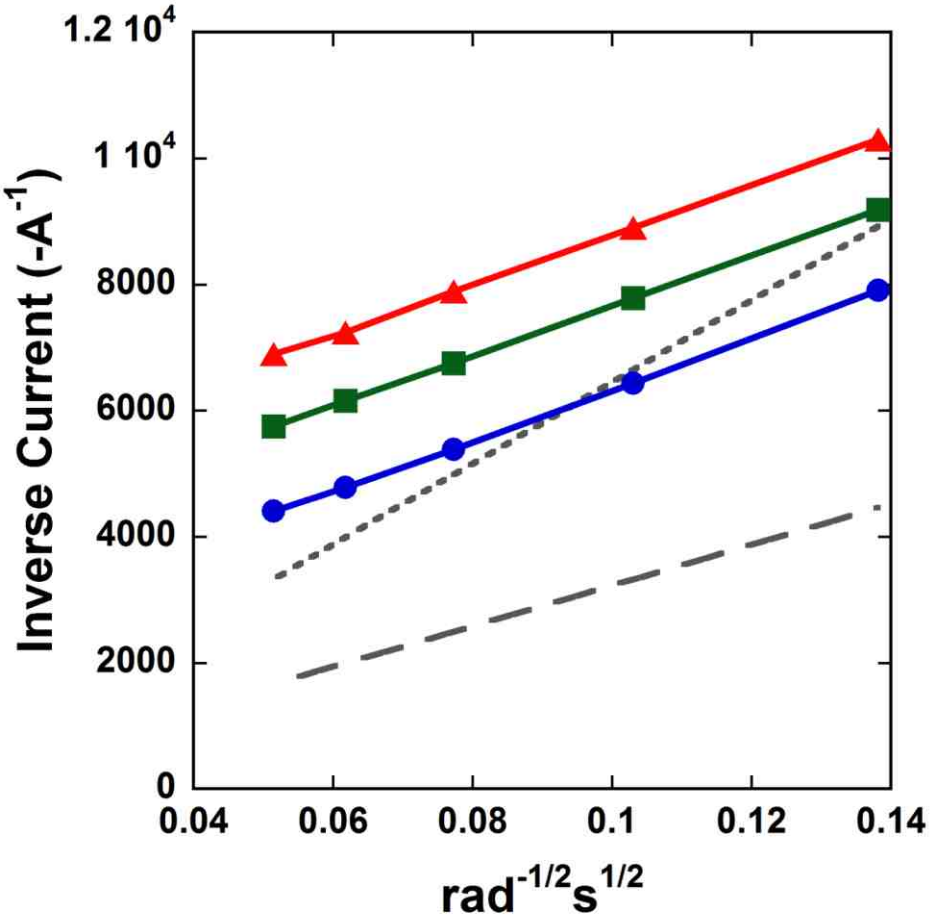

Figure 3.8: Overlay of Koutecky-Levich lines for Cu-α-MnO_2 catalyst samples; 7.5% Cu is shown in red, 7.8% Cu is shown in green, and 9.3% Cu is shown in blue. Idealized slopes for n = 2 e^- (short dashes) and n = 4 e^- (long dashes) are included for comparison.

The assertion that Cu-dopants enhance the kinetics of the ORR appears to be true for the reactions in which peroxide is reduced or catalytically decomposed. Manganese oxides are acknowledged to promote the disproportionation and decomposition of peroxide intermediates. [19, 23] To study peroxide formation on our Cu-α-MnO_2 catalysts, RRDE experiments were performed. The amount of evolved peroxide was calculated by $X_{H2O2} = 2(I_R/N) / [(I_R/N)+(I_D)]$ where I_R is the ring current, N is the collection efficiency of the ring electrode, and I_D is the disk current. The percentage of evolved peroxide can be easily obtained by X_{H2O2} x 100%. [14, 21, 22] Figure 3.9 illustrates the data extracted from RRDE experiments at 500 rpm from the approximate half-wave potential (-300 mV) to the terminal potential (-600 mV) and demonstrates that while the percentage of evolved peroxide is low (< 6%) for all samples, an increasing amount of Cu does appear to correlate to a decrease in the amount of peroxide that is generated.

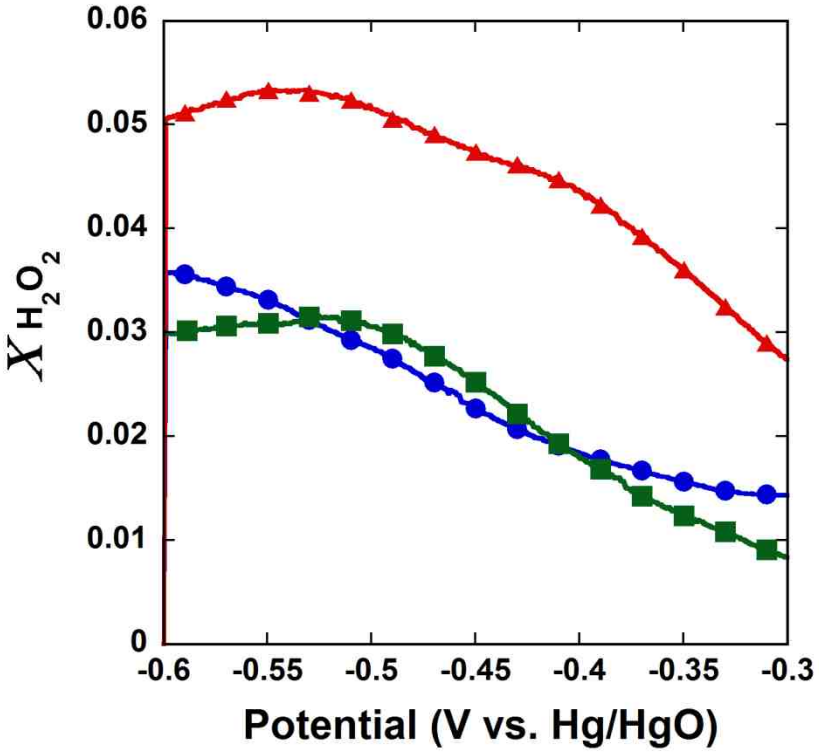

Figure 3.9: RRDE data for Cu-α-MnO_2 catalysts; data for 9.3% Cu is shown in blue circles, 7.8% Cu is shown in green squares, and 7.5% Cu is shown in red triangles.

The onset potential is typically defined as the potential at which the current first becomes negative, as outlined in Chapter 1. An alternative approach to determining the onset potential in this study utilized the intersection of tangential lines fit to the curved portion of the LSV (half-wave region) and the region in which negligible current is generated. This point defines the onset potential as the point at which the slope of the LSV visibly changes. As shown in Table 3.8, Cu-α-MnO_2 catalysts have onset potentials ranging from -100.3 mV vs. Ag/AgCl for the highest Cu-content (9.3%) to -107.7 mV vs. Ag/AgCl for the lowest Cu-content (7.3%). However, the average onset potential for α-MnO_2 in this study was determined to be -85 mV vs. Ag/AgCl. The average onset potential obtained in the same fashion for the benchmark catalyst, 20% Pt on Vulcan XC-72 Carbon (E-Tek), was found to be -51 mV vs. Ag/AgCl. Our previous study indicated that the addition of Cu-dopants improved the onset potential relative to α-MnO_2. [24] Therefore, the work performed thus far has not determined there to be a definitive effect of Cu-dopants on the onset potential of α-MnO_2 nanowire catalysts. As stated in Chapter 1, the standard reduction potential for oxygen is 401 mV vs. SHE, or 192 mV vs. Ag/AgCl. [1, 7] The onset potentials measured in this study, including those for the Pt/C benchmark, are at higher (more negative) overpotentials than the ideal standard value, indicating that the thermodynamic potentials of the reduction reactions at the catalyst surfaces are less than the maximum potential.

The effect of Cu-dopants on the average half-wave potential is not conclusive. The average half-wave potentials of the Cu-α-MnO_2 samples do become increasingly positive as more Cu-dopant is introduced. However, when compared to the undoped α-MnO_2 sample ($E_{1/2}$ = -302 mV), only the Cu-α-MnO_2 catalyst containing 9.3% Cu

demonstrates only a slight favorable increase of +10 mV ($E_{1/2}$ = -292 mV). The half-wave potential for the catalyst containing 7.8% Cu was determined to be -303 mV, which is essentially equivalent to that of α-MnO_2. For the 7.5% Cu sample, $E_{1/2}$ was determined to be -312 mV.

Charge transfer resistances were calculated from the slope of the linear portion of the current-potential curve at low overpotentials (± 10 mV of the onset). When the amount of Cu-dopant reaches 9.3%, the average charge transfer resistance (3430 ± 1391 Ω) has decreased by ~1800 Ω relative to that of α-MnO_2 (5229 ± 1010 Ω). These data indicate that the electronic resistance posed to the charge transfer steps of the reduction reaction is decreased most significantly for the catalyst with the greatest Cu content, Table 3.8. Interestingly, one trial with Cu-α-MnO_2 (9.3% Cu) gave a charge transfer resistance of 2089 Ω, which is comparable to the average charge transfer resistance of 2040 Ω obtained with 20% Pt/C. The calculated resistances for samples containing 7.5% Cu (5744 ± 2357 Ω) and 7.8% Cu (4380 ± 974 Ω) were roughly equivalent to that of α-MnO_2.

Table 3.8: Electrocatalytic Data Extracted from Averaged Linear Scanning Voltammograms

Cu-content (atomic %)	**terminal current density (mA cm^{-2})**	**n (e^-)**	**onset potential (V)**	**$E_{1/2}$ (V)**	***k*** **(cm/s)**	**R_{CT} (Ω)**
0% α-MnO_2	-1.62	3.1	-0.085	-0.302	7.5 x 10^{-3}	5229.3
7.5%	-1.93	3.28	-0.107	-0.312	7.8 x 10^{-3}	5743.7
7.8%	-2.14	3.31	-0.097	-0.303	9.7 x 10^{-3}	4379.7
9.3%	-2.82	3.20	-0.100	-0.292	1.9 x 10^{-2}	3430.3

The electrochemical data presented in Table 3.8 suggest that doping α-MnO_2 nanowires with Cu can result in improved electrocatalytic performance relative to the undoped α-MnO_2, especially for the catalyst containing the highest level of Cu. When compared to the undoped α-MnO_2 catalyst, the most notable improvements for the Cu-doped species are in terminal current densities, *n*-values, and kinetic rate constants. The goal of this research is to elucidate the role of Cu-dopant ions in α-MnO_2 electrocatalysts. Therefore, a more thorough understanding of the relationship between the physicochemical properties of the Cu-doped α-MnO_2 nanowires and the observed electrochemical performance is needed.

In 1979, Brenet considered possible relationships between the physicochemical properties of metallic and mixed metallic oxides used as electrocatalysts and the demonstrated electrochemical reactivity. [60] One physicochemical property of interest in electrochemical applications is the surface area. An increase in surface area can generally be correlated to enhanced electrochemical performance. [60] This was demonstrated by studies of the electrochemical capacitance of α-, β-, γ-, δ-, and λ-MnO_2 conducted by Devaraj *et al*. [30] The two samples of α-MnO_2 nanoparticles (surface areas of 17.29 m^2/g and 123.39 m^2/g) studied were found to demonstrate specific capacitances that correlated to the respective surface area. [30] While the crystalline phase of MnO_2 is known to have a significant impact on the electrochemical performance, a comparison of varied surface areas for a given phase is also relevant. For α-MnO_2 species utilized as catalysts for ORR, higher surface areas are hypothesized to facilitate increased interactions between the Mn-species and O_2 and improve the adsorption and diffusion processes pertaining to O_2. [19]

Therefore, the analysis of the surface areas, average pore diameters, and pore volumes of the synthesized Cu-α-MnO_2 can provide some insight for relative catalytic behaviors observed in this study.

As demonstrated in the linear scanning voltammograms of the Cu-α-MnO_2 nanowires, a trend of increasing surface area correlates to an increase in the reductive current that is generated in the LSVs. The surface area, average pore diameter, and pore volume of the most active Cu-α-MnO_2 sample (9.3% Cu) were measured as being 81.5 m^2/g, 5.9 nm, and 0.24 cm^3/g, respectively. In contrast, the surface area, average pore diameter, and pore volume of the least active Cu-α-MnO_2 sample (7.5% Cu) were measured as being 59.1 m^2/g, 4.7 nm, and 0.14 cm^3/g, respectively (Table 3.6). These results indicate that as the surface area, average pore diameter, and pore volume of the doped α-MnO_2 catalyst increase, there is an increased capacity for the adsorption and sequential reduction of O_2.

While surface area measurements can provide some insight to rationalize demonstrated electrocatalytic performance, previous work by our group has demonstrated that the surface area of a catalyst is not a sole indicator of catalytic behavior. Preliminary studies of previously synthesized α-MnO_2 and Cu-α-MnO_2 (~10% Cu) nanowires revealed that the Cu-doped sample (43.7 m^2/g) demonstrated improved electrocatalytic behavior relative to the undoped α-MnO_2 (73.6 m^2/g). [24] Therefore, developing optimized synthetic procedures that enable precise control of both the amount of dopant and the catalyst surface area would be an objective of future studies.

Possible correlations between structural properties and catalytic activity are also of interest. As demonstrated through further analysis of the PXRD data, the a-axis and

cell volume increase upon addition of Cu-dopants. The open structure of α-MnO_2 facilitates the adsorption and diffusion of O_2, thereby promoting its reduction at the surface of the catalyst. Therefore, it stands to reason that even a slight increase in the unit cell parameters would increase this effect and improve the catalytic performance. As Cheng *et al*. demonstrated with β-MnO_2, even a slight increase of approximately 0.2% in the lattice parameters corresponds to an enhanced ORR process. [45] The observed increase in lattice parameters in β-MnO_2 was attributed to induced oxygen vacancies in the structure, as well as an increasing presence of Mn^{3+}. In our structure, the substitution of a Cu^{2+} ion (ionic radii = 0.73 Å) in a metal site previously occupied by a Mn^{4+} ion (ionic radii = 0.530 Å) would account for some degree of expansion in the lattice. It is also possible that an increase in Mn^{3+} (ionic radii = 0.645 Å, high spin) could be responsible for the observed increase in the crystalline lattice. [61]

Catalytic activity for the ORR can be related to the oxidation state of the Mn species. [23, 38-40] The presence of the Mn^{3+}/Mn^{4+} redox couple enhances the electron mobility between the bulk sample and the surface, thereby enhancing the redox processes of the ORR by facilitating the rapid conversion between $Mn^{3+}OOH$ and $Mn^{4+}O_2$. [62] This reversible conversion was described by Cao *et al*. as follows: [38]

$$MnO_{2\ surface} + MnOOH_{\ bulk} \rightarrow MnOOH_{\ surface} + MnO_{2\ bulk}$$

The Mn^{3+}/Mn^{4+} couple (present in MnOOH and MnO_2 species) has been demonstrated to act as a mediator that assists in charge transfer to adsorbed oxygen during ORR. [23, 38] Considering the Mn-ion center and one O^{2-} ligand, the following equations involving Mn^{3+}/Mn^{4+} can be proposed: [1, 63]

Formation of surface hydroxide	$Mn^{4+}O^{2-} + H_2O + e^- \rightarrow Mn^{3+}\text{-}OH^- + OH^-$
Displacement of surface hydroxide	$Mn^{3+}\text{-}OH^- + O_2^{-}{}_{(adsorbed)} + e^- \rightarrow Mn^{4+}\text{-}O\text{-}O^{2-} + OH^-$
Formation of surface peroxide	$Mn^{4+}\text{-}O\text{-}O^{2-} + H_2O + e^- \rightarrow Mn^{3+}\text{-}O\text{-}OH^- + OH^-$
Formation of surface oxide	$Mn^{3+}\text{-}O\text{-}OH^- + e^- \rightarrow Mn^{4+}O^{2-} + OH^-$
(followed by regeneration of surface hydroxide)	

X-ray photoelectron spectroscopy (XPS) revealed that there was some correlation between Cu-content at the surface and a slight increase in Mn^{3+} character. Because the amount of Cu detected at the surface was approximately 0.5% for the most highly Cu-doped sample, the observed difference in Mn^{3+} content is very subtle. However, other reports have cited Mn^{3+} content increasing as the amount of Cu-dopant in the Mn_xO_y species increases [40, 64] Despite the fact that the atomic percentages of Cu obtained by EDS (Tables 3.1-3.3) were much greater, it is likely that the amount of Cu at the surface is closely related to the observed catalytic behavior. When the peak separation (ΔBE, eV) for the Mn 3s peaks is plotted against the amount of Cu detected by XPS at the surface, a linear relationship is observed as shown in Figure 3.4. This indicates that an increase in the Cu-dopant at the surface could be consistent with a decrease in the average oxidation state of Mn in the catalyst. Many sources have cited the importance of the Mn^{3+}/Mn^{4+} couple of the oxygen reduction reaction; however, the majority of these discussions simply claim that this redox pair facilitates the charge transfer processes involved in ORR. While this is supported by the data, it provides only a limited explanation of the role of Mn^{3+} in the catalyst.

In 2011, Suntivich *et al.* presented design principles for perovskite oxide oxygen reduction catalysts for fuel cells and metal-air batteries. [63] These discussions focused primarily upon the *d*-orbital occupancies of the B-site cation, which resides at the center

of the octahedral complex in the perovskite structure. Therefore, their findings are relevant in this study as well due to the fact that MnO_2 is made of [MnO_6] octahedra with the B-site cation analogous to the Mn center. Suntivich's study reported correlations between *d*-electron number of the B-site cation and ORR activity, and found that the catalytic activity reaches a maximum for cations that are d^4 or d^7. [63] Interestingly, Mn^{3+} is a d^4 species with an electronic configuration that promotes the reduction of oxygen.

Figure 3.10, originally presented by Suntivich *et al.*, illustrates the *d*-electron configuration for a B-site cation (Mn^{3+}). When the cation is in the octahedral complex with six oxygen ligands, the *d*-orbitals split into the t_{2g} and e_g sets, leaving the degenerate e_g orbitals asymmetrically filled in the high-spin state. This degeneracy is removed upon a geometric distortion to tetragonal symmetry. The e_g electron resides in the d_z^2 orbital, which is oriented toward the surface OH^- group and is slightly lower energetically than the $d_{x^2-y^2}$ orbital. [63]

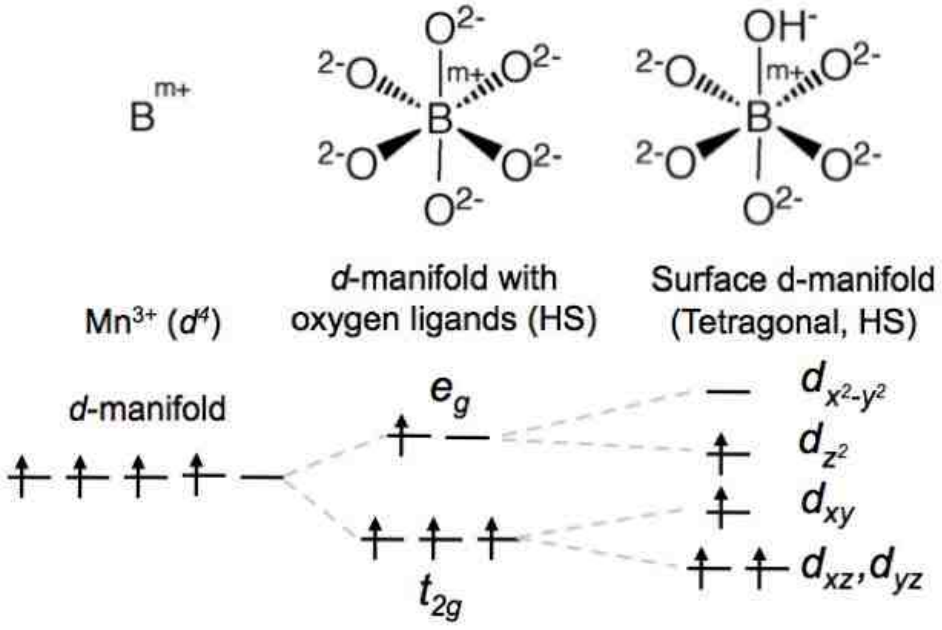

Figure 3.10: The d-orbitals of the Mn^{3+} free ion (far left), the Mn^{3+} ion in the octahedral complex (center), and the distorted tetragonal high spin state (far right). [63]

As seen in step one of the reaction schematic below (Figure 3.11), there is an exchange that must occur between O_2^{2-} and OH^- on the transition metal site. It is proposed that the rate-limiting step of the ORR is the displacement of the surface hydroxide species, which is driven by the transfer of the unpaired e_g electron to the O-O π^2 orbital. The presence of the e_g electron destabilizes the B-OH^- bond, thereby enabling the formation of B-O_2^{2-}. [63]

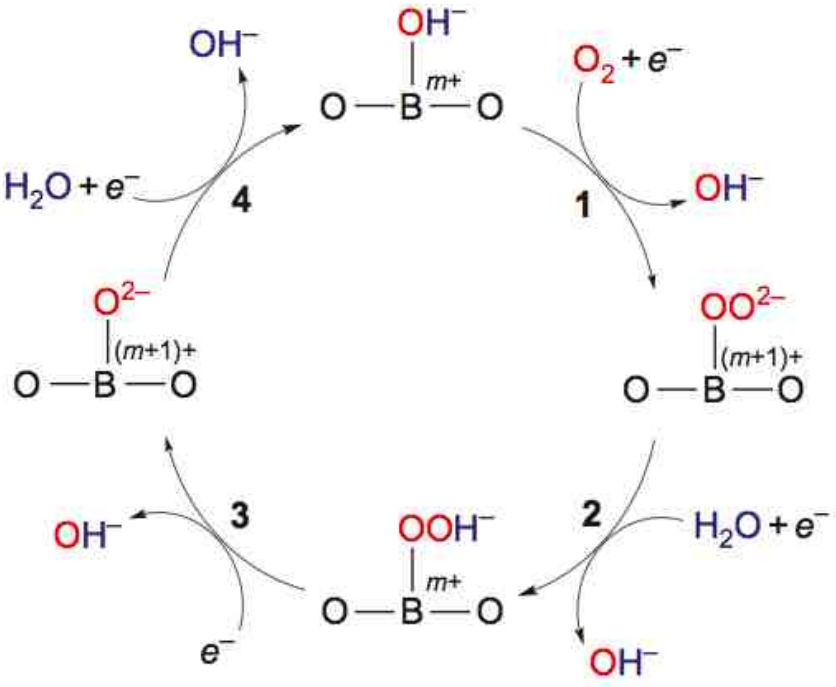

Figure 3.11: A proposed reaction schematic for the ORR on the cationic transition metal B-site. [63]

Step two of the cycle is the formation of surface peroxide, which is reduced to the surface oxide in step three. Finally, step four involves the regeneration of the surface hydroxide. It is evident that the redox of the Mn center between the 3+ and 4+ states is involved, but this mechanism provides a basis for understanding how the electronic configuration of the Mn^{3+} ion contributes to the reaction. [63]

Since the majority of the Cu-dopant species resides within the nanowire, it is currently hypothesized that the conductivity of the nanowires would demonstrate a trend that correlates to the Cu-content observed by EDS. Performing a series of measurements in which the conductivity of a single nanowire, or even a small cluster of nanowires, for α-MnO_2 samples of varying Cu-content could potentially provide additional insight into the underlying role of Cu-dopants in α-MnO_2 nanowire electrocatalysts. While obtaining this data via conductive tip atomic force microscopy (AFM) is a future objective of this study, some insight can be drawn from recent literature that will support the hypothesis of Cu-doping enhancing the conductivity of α-MnO_2.

A previous report has stated that the measured conductivity of α-MnO_2 nanowires synthesized by a hydrothermal route to be 0.086 S/cm. [19] Manganese oxide (MnO_2) has been cited as being a semiconductor at ambient temperatures, [65] but it is acknowledged that manganese oxides inherently possess low conductivities. [28] As a result, conductive carbon additives are commonly utilized in composite electrode materials to enhance the overall conductivity. However, some recent reports have demonstrated an enhanced electrical conductivity for manganese oxides achieved by Cu-doping. Li *et al.* demonstrated the synthesis of Cu-doped Mn_2O_3 mesocrystals with charge transfer abilities that are more favorable than the un-doped Mn_2O_3 mesocrystals. [66] Similarly, a Cu-doped MnO_2 sample prepared by cyclic voltammetry also demonstrated improved charge transfer relative to the undoped film. [67] A study of $Cu_{1+x}Mn_{1-x}O_2$ ($0 \leq x \leq 0.2$) solid solutions revealed that as the Cu-content increased, the activation energy related to electrical conductivity decreased, which is indicative of a correlation between increased Cu-content and improved charge carrier mobility. [68]

3.4 Summary and Conclusions

The synthesis of Cu-doped α-MnO_2 was achieved by the addition of $Cu(NO_3)_2 \cdot 3H_2O$ into the hydrothermal reaction previously used to prepare α-MnO_2 nanowires. [19, 24] By varying the amount of Cu-precursor in discrete molar ratios of 1:1, 1:0.5, and 1:0.25 (Mn:Cu), varying atomic percentages of Cu were attained, 9.3%, 7.8%, and 7.3%, respectively. The α-MnO_2 crystalline phase and the nanowire morphology were retained upon doping, both factors known to be critical to the overall catalytic performance. The inclusion of Cu was demonstrated to increase the lattice parameters of α-MnO_2 that trended with Cu content. In addition, the BET surface areas, average pore diameters, and pore volumes demonstrated increases that correlated with Cu content.

Doping α-MnO_2 nanowires with Cu improves their performance as catalysts for the ORR in alkaline electrolyte. Specifically, the inclusion of this dopant species provides for not only a higher terminal current density, but also enhanced kinetic rate constants that exceed rates attained by α-MnO_2 alone. Data obtained through RRDE studies indicates that the production of peroxide decreases as the amount of Cu increases. The charge transfer resistances demonstrate similar trends; the average resistance decreases as the amount of Cu in the catalyst increases.

The inclusion of Cu also has an effect on the oxidation state of Mn, and more specifically, the Mn^{3+}/Mn^{4+} couple. The oxidation state of surface Mn was estimated by examining the splitting of the Mn 3s peaks by XPS, which revealed that as the amount of Cu in the sample increased, the concentration of Mn^{3+} increased as well. Mn^{3+} has a *d*-electron count of four (d^4), which indicates the presence of an unpaired electron in the degenerate e_g set in octahedral geometry. Through a distortion to the tetragonal geometry,

the e_g orbitals split, leaving the unpaired electron in the d_z^2 orbital at a lower energy, oriented toward the surface OH^-. This electron destabilizes the bond between the Mn^{3+} ion and the surface hydroxide, promoting the formation and subsequent reduction of $O_2^{2=}$ on the surface. [63]

The presence of the Cu-dopant ions in α-MnO_2 nanowires increases the Mn^{3+} content at the catalyst surface, thereby promoting the reduction of oxygen. In addition, it is likely that the Cu-species enhance the conductivity of the α-MnO_2 electrocatalyst. Future research efforts will attempt to measure the conductivity of the Cu-α-MnO_2. Also, the development of optimized synthetic procedures that enable the precise control of Cu-content and Mn oxidation state is of interest.

Chapter 4

Efforts to Understand the Role of Ni-dopants in α-MnO_2 Nanowire Catalysts for the Oxygen Reduction Reaction in Alkaline Media

4.1 Introduction

Doping manganese oxide electrocatalysts with nickel has been demonstrated to enhance the catalytic performance in several electrochemical studies. [23, 24, 41, 42] These doped species have demonstrated catalytic activities reported to be comparable to that of Pt/C commercial benchmarks, indicating their potential to serve as cost-effective alternatives to precious metal catalysts. [23, 24] Other studies have noted demonstrated abilities to efficiently decompose peroxide [36, 41] and operate in both aqueous and organic electrolytes, [42] as well as exhibit tolerance to methanol crossover. [24] Ongoing efforts to gain insight into the role of the Ni-dopants in α-MnO_2 nanowire electrocatalysts are presented.

4.2 Experimental

4.2.1 General

All chemicals were obtained commercially and used as received, without further purification. $MnSO_4 \cdot H_2O$ and $Ni(NO_3)_2 \cdot 6H_2O$ were purchased from Alfa Aesar. $KMnO_4$, isopropanol, and Nafion solution (5 wt. % solution in water and lower aliphatic alcohols) were used as received from Sigma-Aldrich.

4.2.2 Synthesis

The synthesis of Ni-α-MnO_2 nanowires was performed via a modified hydrothermal reaction in an acid digestion bomb (PTFE liner, 45 mL capacity, Parr™ reactor), adapted from a previously published synthesis for α-MnO_2 and introduced in our previous studies. [19, 24] Solutions of $MnSO_4 \cdot H_2O$ (0.2 g, 1.18 mmol), $KMnO_4$ (0.5 g, 3.16 mmol) and a specified amount of $Ni(NO_3)_2 \cdot 6H_2O$ in deionized water were heated in the acid digestion bomb at 140 °C for 120 hours to ensure nanowire morphology. $Ni(NO_3)_2 \cdot 6H_2O$ was added in specific molar ratios to the manganese-containing precursor of 1:1, 1:0.5 and 1:0.25 (Mn:Ni) to achieve different copper doping levels. Phase-pure α-MnO_2 was obtained by a hydrothermal reaction that excluded the copper precursor. [19, 24] Following heating for 120 hours at 140 °C, all reactions were cooled to room temperature, and the solids were isolated by centrifugation (3000 rpm). The solids were washed with deionized H_2O (4x, 10 mL) and ethanol (4x, 10 mL), isolated via centrifugation, and dried in a vacuum oven overnight at 65 °C.

4.2.3 Materials Characterization

Powder X-ray Diffraction (PXRD). Catalyst powders were mounted directly onto a zero background holder purchased from The Gem Dugout. Samples were scanned at a rate of 0.02°/2 s in the 2θ range of 10-80° on a Bruker D8 Advance Diffractometer in Bragg-Brentano geometry with Cu Kα radiation and a diffracted beam graphite monochromator. Phase identification was achieved through use of the Jade 9.0 software suite and the Joint Committee on Powder Diffraction Standards (JCPDS).

Transmission Electron Microscopy (TEM). TEM analysis was carried out on a JEOL 2010F electron microscope at 200kV acceleration voltage. Energy Dispersive

Spectroscopy (EDS) was collected using its attachment of Oxford Instruments ISIS/Inca System with Oxford Pentafet Ultrathin Window Detector (UTW).

Scanning Electron Microscopy (SEM). The samples were dispersed onto carbon tape and imaged using a Zeiss Supra 55VP field emitter gun scanning electron microscope (FEGSEM). Samples were sputter coated with gold-palladium prior to analysis. A Noran EDS detector and Noran System Six software were used for the acquisition of the EDS spectra. EDS data were plotted with Kaleidagraph software for presentation purposes.

Brunauer-Emmett-Teller (BET) Surface Area Analysis. Gas sorption experiments were performed on an Autosorb iQ2-Chemi instrument (Quantachrome Instruments, Boynton Beach FL, USA) at 77 K (liquid nitrogen temperature) using ultra-high purity (UHP) nitrogen as adsorbate. Specimens were degassed at 140 ºC for between 2 and 3 hours (the exact degas time was determined automatically based upon periodic evaluation of rate of gas evolution from each specimen). The specimen cells were quartz glass with a 9 mm outer diameter, and filler rods were inserted to reduce dead volume above the sample. Cell volumes were determined prior to each run using UHP helium.

Isotherms were typically measured using 40 adsorption points and 40 desorption points, with an optional 30 additional adsorption points in the micropore range. Surface areas were calculated using the Brunauer-Emmett-Teller (BET) method using seven adsorption points in the range P/P_0 = 0.05 to 0.3. Total pore volumes were calculated based on the total gas adsorbed at P/P_0 values of 0.996. Pore sizes were determined using the Barrett-Joyner-Halenda (BJH) method during the desorption branch of the isotherm, ignoring P/P_0 points below 0.35.

X-ray Photoelectron Spectroscopy (XPS). X-ray photoelectron spectroscopy (XPS) was performed with a Kratos Axis Ultra DLD instrument with base pressures less than 5 x 10^{-9} Torr. Powder samples were pressed into carbon tape for analyses. No interferences from the carbon tape were observed. Charge neutralization was not required; however, the neutralizer was used for all samples to ensure that differential charging did not influence the spectral lineshapes. XPS was performed with a monochromatic Al-Kα (1486.7 eV) source operated at 150 W with an elliptical spot size of 300x700 microns. Survey spectra were taken with an 80 eV pass energy, 600 meV step, and 100 ms dwell times. With Al-Kα X-rays the Ni 2p 3/2 appears as a relatively sharp peak on a much broader Mn LMM Auger peak. XPS was also performed with a non-monochromatic Mg X-ray source (1253.6 eV) operated at 180 W to confirm the presence of nickel. The energy resolution is lower with the non-monochromatic source, so step sizes were 800-1000 meV for survey spectra. XPS with the Mg source was helpful for resolving the Ni 2p peaks on a relatively flat background. High resolution spectra were recorded with a 20 eV pass energy, 200 ms dwell time, and step sizes ranging from 30-50 meV (100 meV for Mg X-ray XPS). Data processing was performed with CasaXPS. Quantifications were performed using the built-in relative sensitivity factors. Mn 3s peak fitting was performed with a linear background and two unconstrained Gaussian/Lorentzian (70/30) peaks.

4.2.4 Electrochemical Studies

Oxygen reduction studies were performed using rotating disk electrode assembly. Catalyst inks consisting of 5.0 mg of catalyst material, 200 µL isopropanol, and 300 µL Nafion solution were sonicated for approximately 20 minutes. For RDE, a 5 µL aliquot

was drop-cast on a glassy carbon RDE electrode (BASi, active area= 0.0788 cm^2). Prior to each drop-coating process, the RDE glassy carbon electrode surface was polished with 0.05 μm alumina slurry and rinsed with deionized water and ethanol.

Linear Scanning Voltammograms were executed in a potential window from 0.2 V to -0.6 V (V vs. Ag/AgCl) at a scan rate of 1 mV/s. For RDE, LSVs were run at rotation rates of 500, 900, 1600, 2500, and 3600 rpm. All experiments were run in 0.1 M KOH electrolyte that had been thoroughly purged with UHP oxygen (or UHP nitrogen for background measurements) prior to each run. The appropriate gaseous atmosphere was preserved by blanketing for the extent of the experiment.

RDE experiments were performed in a three electrode cell, manufactured by Bioanalytical Systems, Inc. connected to a Versastat 4 potentiostat operated by VersaStudio software. Electrodes (from BASi) included the glassy carbon working electrode prepared as previously described, a Pt coil counter electrode, and a Ag/AgCl reference electrode (3 M NaCl, potential= 0.209 V vs. NHE).

4.3 Results and Discussion

4.3.1 Synthesis and Characterization

Initially, the synthesized materials were examined by X-ray diffraction (XRD) and scanning electron microscopy (SEM) coupled with energy dispersive spectroscopy (EDS). Previous studies have established that α-MnO_2 nanowires contain the most active phase and morphology for manganese oxide catalysts for the ORR in alkaline electrolyte. Therefore, upon attempted doping with Ni, it was critical that the α-MnO_2 phase and

nanowire morphology be retained. As shown in Figure 4.1 a-c, SEM imaging confirmed that the reaction products were of the nanowire morphology. The obtained XRD patterns in Figure 4.1 d-f indexed to JCPDS number 00-044-0141, serving as a clear indication that the crystalline phase of α-MnO_2 was retained.

EDS obtained in conjunction with SEM imaging served as preliminary confirmation of the presence of Ni in the nanowires; however, further data were desired in order to quantify the amount of Ni in the synthesized samples. Therefore, EDS measurements were obtained via transmission electron microscopy (TEM). The complete set of data is provided in Tables 4.1, 4.2, and 4.3; corresponding averages and standard deviations are also included. EDS of the sample prepared at the 1:1 Mn:Ni ratio contained 6.13 ± 1.55% Ni; the sample prepared at the 1:0.5 Mn:Ni ratio contained 4.43 ± 0.60% Ni, and the sample prepared at 1:0.25 Mn:Ni ratio contained 2.02 ± 0.43% Ni. A TEM image (Figure 4.2) of a Ni-α-MnO_2 nanowire (~ 100 nm wide) reveals that it is actually comprised of many small, very thin wires (~ 10 nm wide) bundled together.

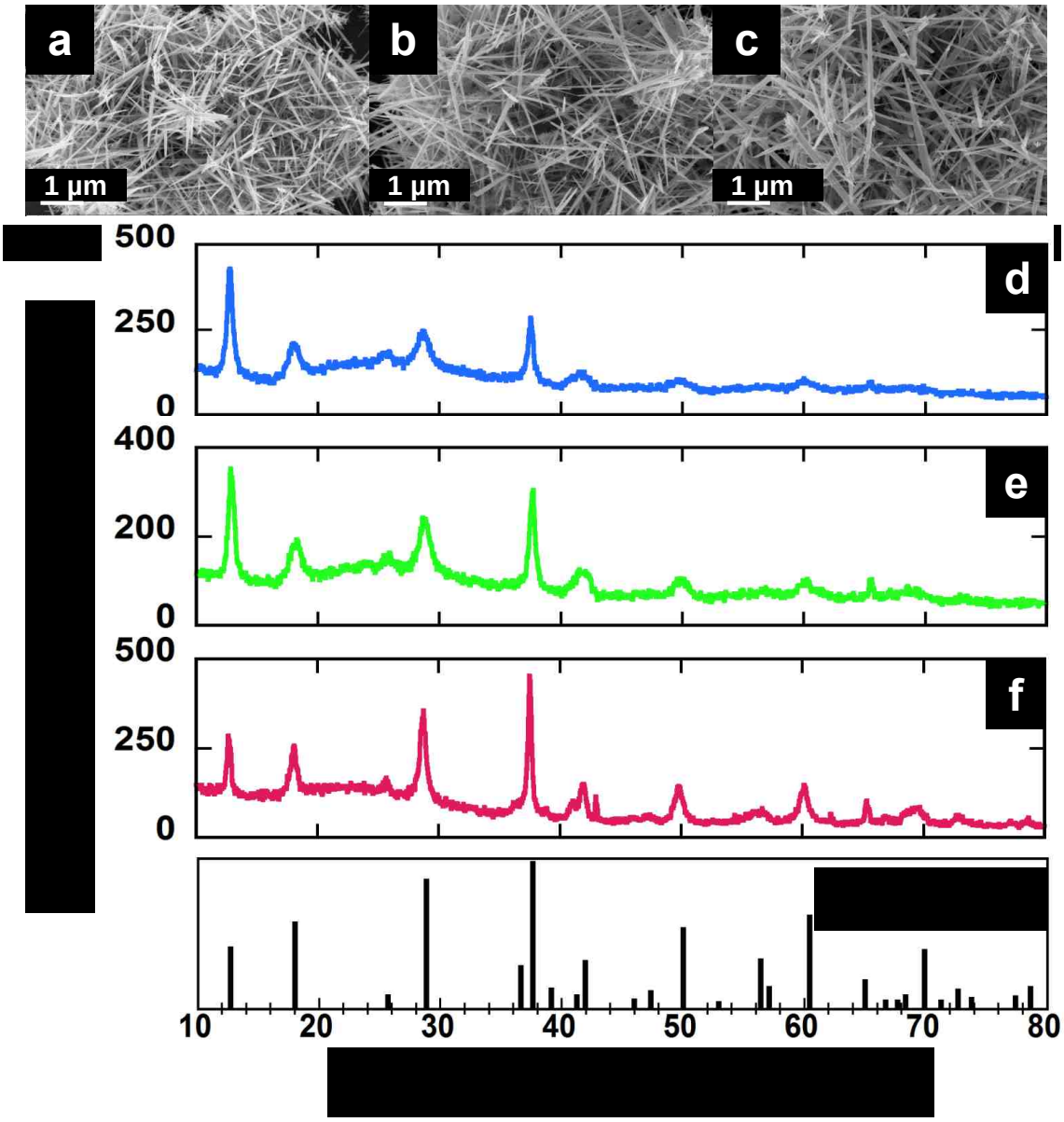

Figure 4.1: Characterization data for the synthesized Ni-doped α-MnO_2 nanowires. a-c) SEM images of the nanowires synthesized at a Mn:Ni ratio of 1:1, 1:0.5, and 1:0.25, respectively. d-f) XRD patterns for Ni-α-MnO_2 nanowires synthesized at a Mn:Ni ratio of 1:1, 1:0.5, and 1:0.25, respectively.

Table 4.1: EDS Measurements of Atomic Percent Content of Ni-α-MnO_2, prepared at reactant ratio 1:1, Mn:Ni

	Ni	Mn	O	K
Ni-α-MnO_2	6.13	43.55	49.89	0.43
	6.41	43.56	49.99	0.04
	7.42	42.38	49.93	0.26
	10.1	39.85	49.98	0.06
	5.54	43.29	49.61	1.56
	5.93	42.78	49.57	1.72
	5.5	43.17	49.56	1.78
	4.96	42.11	49.02	3.91
	4.75	42.46	49.07	3.72
	4.53	42.45	48.99	4.02
AVERAGE	**6.13**	**42.56**	**49.56**	**1.75**
STD. DEV.	1.55	1.03	0.38	1.53

Table 4.2: EDS Measurements of Atomic Percent Content of Ni-α-MnO_2, prepared at reactant ratio 1:0.5, Mn:Ni

	Ni	Mn	O	K
Ni-α-MnO_2	3.94	42.82	48.92	4.32
	3.92	42.84	48.92	4.32
	4.02	43.48	49.16	3.34
	3.52	43.78	49.1	3.6
	4.13	43.14	49.09	3.65
	4.79	42.54	49.11	3.56
	3.99	43.34	49.11	3.56
	5.37	44.44	49.93	0.26
	4.84	44.96	49.93	0.28
	5.14	44.65	49.93	0.28
	5.09	44.65	49.93	0.27
AVERAGE	**4.43**	**43.70**	**49.38**	**2.49**
STD. DEV.	0.60	0.82	0.43	1.71

Table 4.3: EDS Measurements of Atomic Percent Content of Ni-α-MnO_2, prepared at reactant ratio 1:0.25, Mn:Ni

	Ni	**Mn**	**O**	**K**
Ni-α-MnO_2	1.84	44.35	48.73	5.08
	1.46	44.76	48.74	5.04
	1.93	44.24	48.72	5.11
	2.78	43.33	48.7	5.18
	1.79	44.42	48.74	5.05
	2.14	44.11	48.75	5.00
	1.61	44.55	48.72	5.13
	1.84	44.29	48.71	5.16
	1.83	44.42	48.75	5.00
	2.07	44.2	48.76	4.97
	2.93	43.49	48.81	4.78
AVERAGE	**2.02**	**44.20**	**43.74**	**5.05**
STD. DEV.	0.43	0.41	0.03	0.11

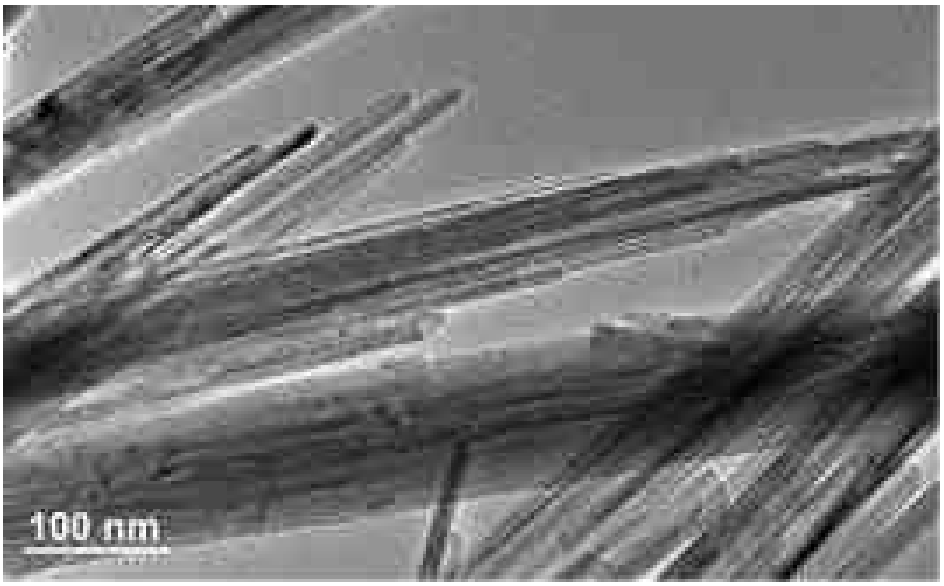

Figure 4.2: TEM image of Ni-α-MnO_2 nanowires.

X-ray photoelectron spectroscopy (XPS) was utilized to analyze the content at the surface of the nanowires. As expected, the Ni content at the surface was much lower than the atomic percentages measured with EDS. The data are presented in Table 4.4.

Table 4.4: Atomic Percentage of Ni as Measured by XPS

Percentages obtained by EDS are included for comparison.

Sample (Mn:Ni Ratio)	Atomic % Ni (XPS)	Atomic % Ni (EDS)
α-MnO_2	0%	0%
Ni-α-MnO_2 (1:0.25)	0.29%	2.0%
Ni-α-MnO_2 (1:0.5)	0.54%	4.4%
Ni-α-MnO_2 (1:1)	0.57%	6.1%

XPS was also utilized to gain a more thorough understanding of the oxidation states of the Mn ions within the Ni-α-MnO_2 catalysts. The difference in binding energy between the Mn 3s peaks can be used to approximate the oxidation state, as shown in Figures 4.3 and 4.4. As the amount of Ni in the sample increases, the extent of splitting between the Mn 3s peaks becomes greater, indicating that more Mn^{3+} is present. [57, 58] Interestingly, the greatest Mn 3s splitting (4.6356 eV) was observed for the sample synthesized at the Mn:Ni ratio of 1:0.5 (0.54% Ni at surface, 4.4% Ni by EDS). The Mn 3s splitting obtained for the sample synthesized at the Mn:Ni ratio of 1:1 was only slightly lower (4.6205 eV). The Mn 3s spectra are shown in Figure 4.3. Figure 4.4 shows the

relationship between Ni-content at the surface and the splitting between the Mn 3s peaks (Δ BE, eV). The splitting values are presented in Table 4.5.

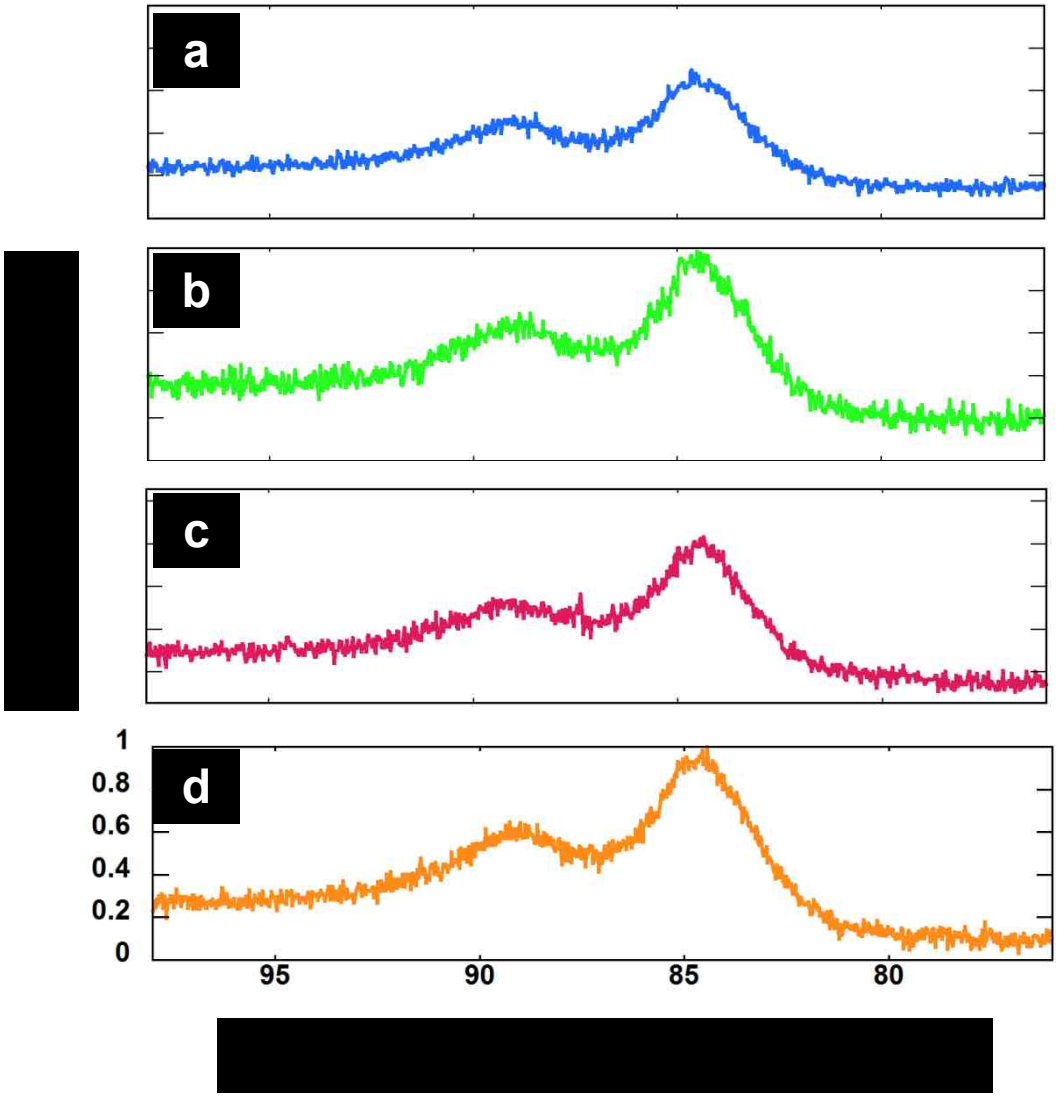

Figure 4.3: XPS data showing the splitting of the Mn 3s peaks a) 6.1% Ni, 0.57% Ni at surface, b) 4.4% Ni, 0.54% Ni at surface, c) 2.0% Ni, 0.29% Ni at surface, and d) undoped α-MnO_2.

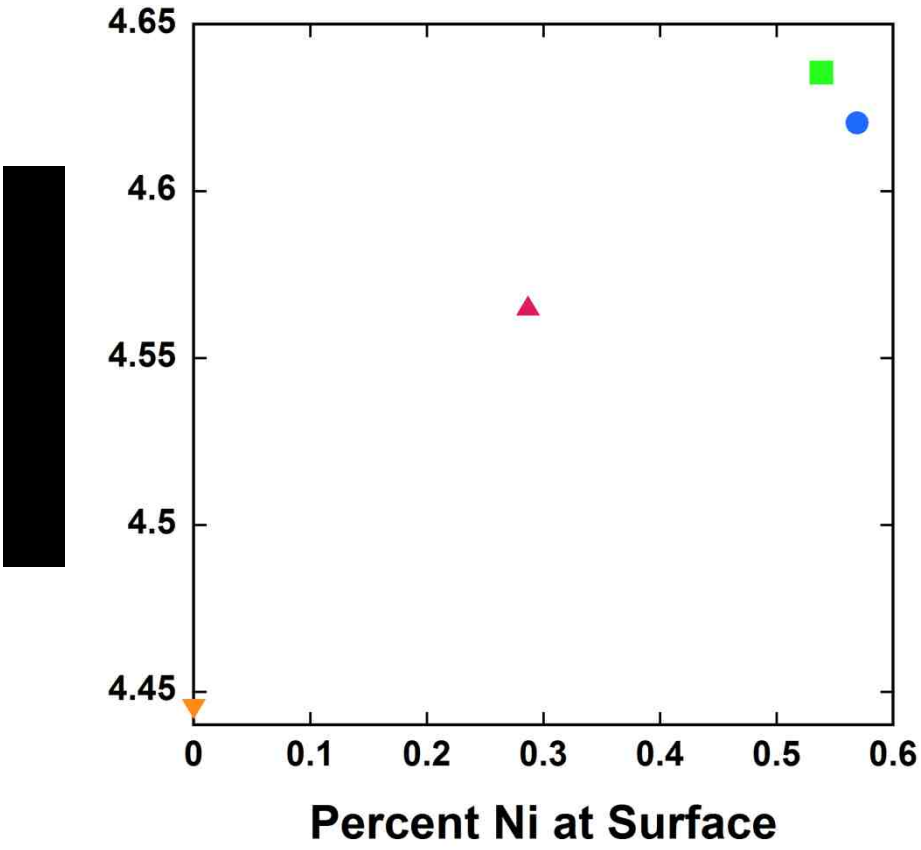

Figure 4.4: The splitting of the Mn 3s peaks (ΔBE, eV) plotted as a function of the percent Ni measured at the surface by XPS.

Table 4.5: Splitting of Mn 3s Peaks as Observed by XPS

Sample (Symbol)	Atomic % Ni (XPS)	ΔBE (eV)
α-MnO_2 (▼)	0%	4.4448
Ni-α-MnO_2 (▲)	0.29%	4.5657
Ni-α-MnO_2 (■)	0.54%	4.6356
Ni-α-MnO_2 (●)	0.57%	4.6205

The surface areas, average pore diameters, and pore volumes of the Ni-α-MnO_2 powders were analyzed using the Brunauer-Emmett-Teller (BET) method and the Barrett-Joyner-Halenda (BJH) method. The results of these studies are shown in Table 4.6; corresponding isotherm plots are provided in Figure 4.5 a-c. The sample containing 6.1% Ni was determined to have a surface area of 60.8 m^2/g, an average pore diameter of 12.42 nm, and a pore volume of 0.35 cm^3/g. The sample containing 4.4% Ni was determined to have a surface area of 52.3 m^2/g, an average pore diameter of 8.65 nm, and a pore volume of 0.22 cm^3/g. Finally, the sample containing 2.0% Ni was determined to have a surface area of 51.8 m^2/g, an average pore diameter of 4.6 nm, and a pore volume of 0.12 cm^3/g. Clearly, as more Ni is introduced into the α-MnO_2 structure, the surface area, average pore diameter, and pore volume increase as well.

Table 4.6: BET Measurements for Ni-α-MnO_2 Nanowires

Ni-content (avg. atomic %)	**BET Surface Area (m^2/g)**	**Average Pore Diameter (nm)**	**Pore Volume (cm^3/g)**
2.0%	51.8	4.6	0.12
4.4%	52.3	8.65	0.22
6.1%	60.8	12.42	0.35

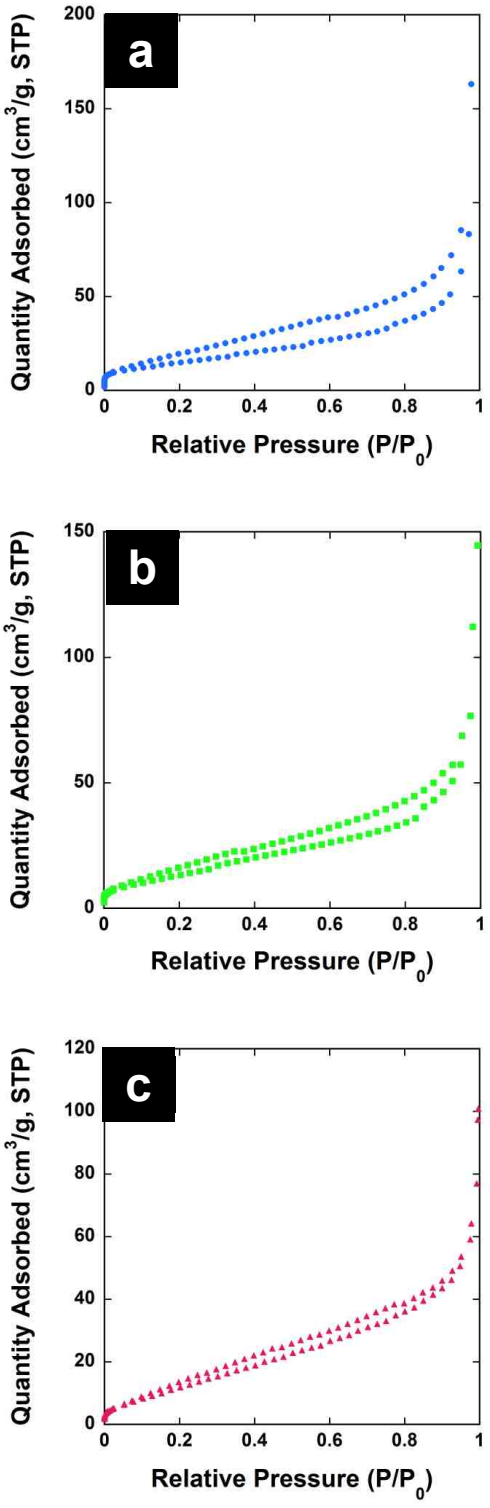

Figure 4.5: Nitrogen sorption isotherms for a) Ni-α-MnO_2, 6.1% Ni (60.8 m^2/g), b) Ni-α-MnO_2, 4.3% Ni (52.3 m^2/g), and c) Ni-α-MnO_2, 2.0% Ni (51.8 m^2/g).

4.3.2 Electrochemical Analysis

Films of the as-synthesized Ni-α-MnO_2 powders were prepared via a drop-cast technique in which an aliquot of the catalyst ink was deposited onto rotating disk electrodes as previously described. The electrodes were utilized for RDE studies, which enable the observation of kinetically controlled processes in the absence of mass-transfer phenomena. Figure 4.6 shows averaged linear scanning voltammograms obtained for Ni-α-MnO_2 at 6.0% Ni (Figure 4.6 a), 4.4% Ni (Figure 4.6 b), and 2.0% Ni (Figure 4.6 c). For each individual set of data, there is an increase in the terminal current density that corresponds to an increase in the rotation rate of the working electrode; this is attributed to the change in flux of O_2 to the electrode surface that occurs as the rotation rate increases. The terminal current density (-0.6 V vs. Ag/AgCl) attained by the catalyst containing 2.0% Ni was -1.46 mA/cm^2; and for the catalyst containing 4.4% Ni the terminal current density was -2.53 mA/cm^2. Finally, for the catalyst containing 6.1% Ni, the terminal current density attained was -1.78 mA/cm^2. When compared to the average terminal current density for undoped α-MnO_2 of -1.62 mA/cm^2, only the Ni-α-MnO_2 samples containing 4.4% Ni and 6.1% Ni demonstrate improvements relative to the undoped sample. The terminal current density for the sample containing 2.0% Ni was less than that attained by the undoped α-MnO_2. Figure 4.6 d shows an overlay of averaged LSVs obtained at 2500 rpm for each Ni-α-MnO_2 catalyst sample. The terminal current densities do not trend in accordance with the Ni-content of the nanowires as the sample containing 4.4% Ni attains the highest current density.

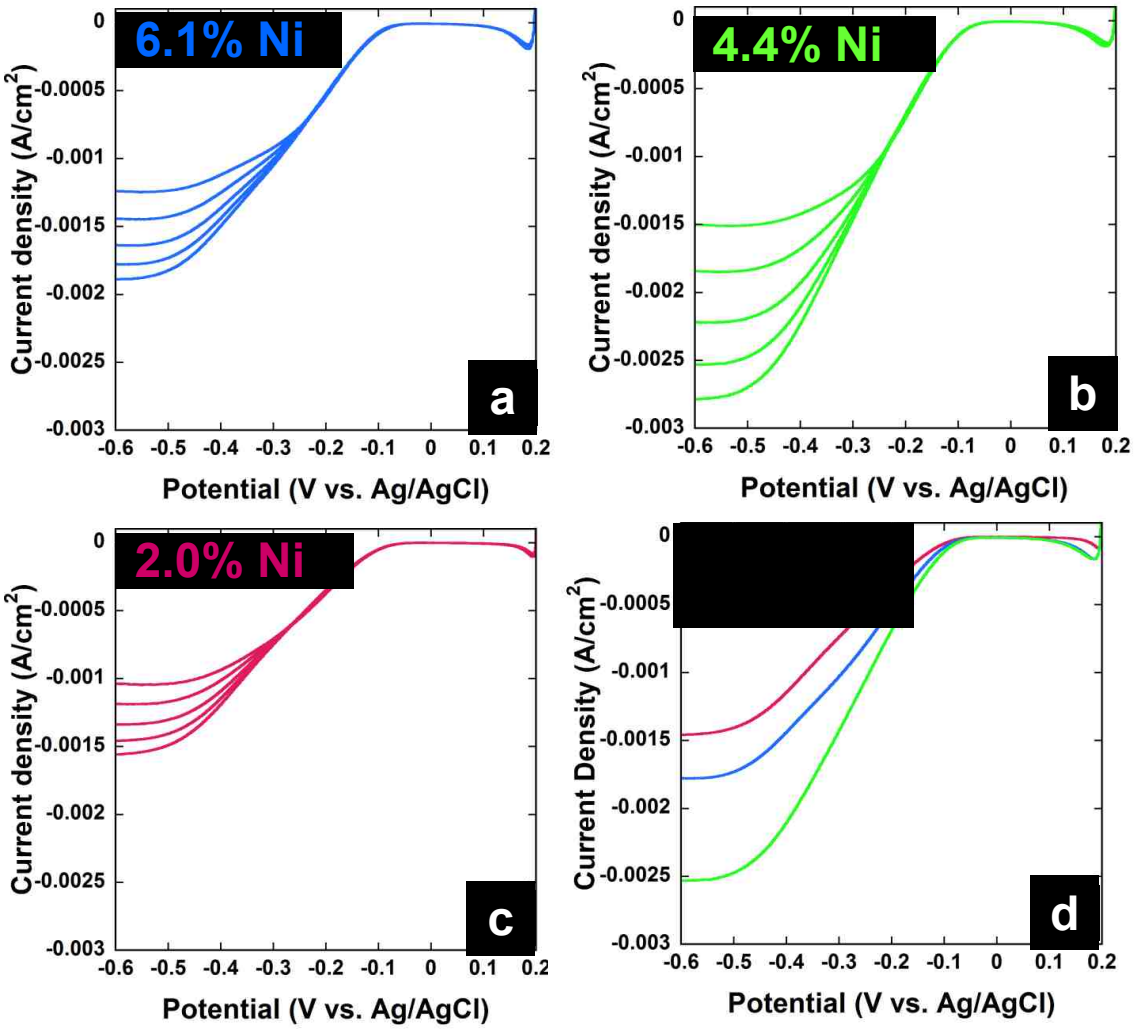

Figure 4.6: a-c) Averaged linear scanning voltammograms obtained for Ni-α-MnO_2 at 500, 900, 1600, 2500, and 3600 rpm. d) Comparative overlay of averaged LSVs obtained at 2500 rpm, revealing an increase in terminal current density that does not trend directly with Ni-content.

Further analysis of the linear scanning voltammograms provides a number of metrics of comparison for Ni-α-MnO_2 catalysts. As stated in Chapter 1, applying the Koutecky-Levich equation to the LSV data enables the *n*-value to be calculated. The *n*-value can provide some insight into the predominant reaction pathway. The calculated *n*-value for the Ni-α-MnO_2 sample containing 6.1% Ni was 3.45 e^-, the calculated *n*-value for the sample containing 4.4% Ni was 3.29 e^-, and the calculated *n*-value for the sample containing 2.0% Ni was 3.26 e^-. Clearly, there is a demonstrated improvement relative to the undoped α-MnO_2 (n = 3.1 e^-). [19, 24] These data suggest that the *n*-value increases as the amount of Ni-dopant increases, though the most significant improvement is attained with the catalyst containing 6.0% Ni.

The kinetic rate constants, calculated using the y-intercept of the Koutecky-Levich lines, demonstrate a trend that is similar to the trend observed for terminal current density. Specifically, the sample containing 4.4% Ni was shown to give a kinetic rate constant of 1.4 x 10^{-2} cm/s. In contrast, the calculated kinetic rate constants for the samples containing 6.1% Ni and 2.0% Ni were 6.50 x 10^{-3} cm/s and 5.75 x 10^{-3} cm/s, respectively. Therefore, only the sample containing 4.4% Ni yielded an improved kinetic rate constant relative to that of the undoped α-MnO_2 (7.5 x 10^{-3} cm/s). An overlay of the Koutecky-Levich lines for the Ni-α-MnO_2 catalyst series is shown in Figure 4.7.

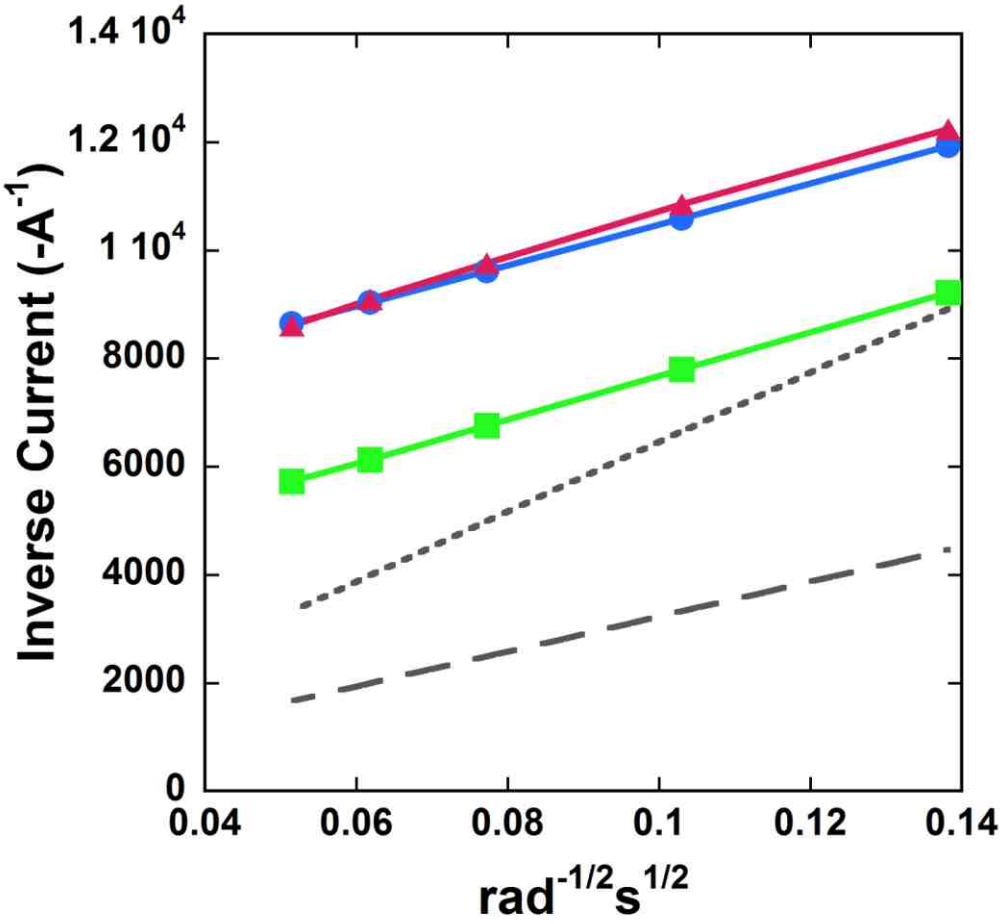

Figure 4.7: Overlay of Koutecky-Levich lines for Ni-α-MnO_2 catalyst samples; 2.0% Ni is shown in pink, 4.4% Ni is shown in green, and 6.1% Ni is shown in blue. Idealized slopes for n = 2 e^- (short dashes) and n = 4 e^- (long dashes) are included for comparison.

As described in Chapter 1, the onset potential is typically defined as the potential at which the current first becomes negative. An alternative approach to determining the onset potential in this study utilized the intersection of tangential lines fit to the curved portion of the LSV (half-wave region) and the region in which negligible current is generated. This point defines the onset potential as the point at which the slope of the LSV visibly changes. The onset potentials of the Ni-α-MnO_2 catalysts are all within 5 mV of each other, only ranging from -0.093 V (4.4% Ni) to -0.098 V (6.1% Ni). These are slightly more negative than the onset potential for the undoped α-MnO_2 (-0.085 V). Therefore, this study did not reveal that Ni-doping has a significant effect on exhibited onset potentials.

An increase in catalyst Ni-content from 2.0% to 6.1% gives a slight improvement in half-wave potential (+ 0.013 V). As compared to undoped α-MnO_2 ($E_{1/2}$= -0.301 V), the half-wave potentials of the 4.4% Ni and 6.1% Ni catalysts are roughly equivalent ($E_{1/2}$=-0.297 V). Therefore, the data indicate that there is not a significant effect on the half-wave potential that correlates to Ni-content.

Charge transfer resistances were calculated from the slope of the linear portion of the current-potential curve at low overpotentials (± 10 mV of the onset). The charge transfer resistance for the catalyst containing 6.1% Ni (5252.5 ± 595 Ω) was roughly equivalent to that of the undoped α-MnO_2 (5229 ± 1010 Ω). While the calculated charge transfer resistance for the catalyst containing 4.4% Ni (4839.8 ± 2670 Ω) was slightly less than that of the undoped material, the inclusion of the significant standard deviation does not allow any definitive conclusions to be drawn. The catalyst containing the least amount of Ni-dopant (2.0% Ni) was found to have a higher charge transfer resistance

(7918.7 ± 1982 Ω) than that of the undoped sample. The electrocatalytic data for the Ni-α-MnO_2 catalyst series are summarized in Table 4.7.

Table 4.7: Electrocatalytic Data Extracted from Averaged Linear Scanning Voltammograms

Ni-content (atomic %)	terminal current density (mA cm^{-2})	n (e^-)	onset potential (V)	$E_{1/2}$ (V)	*k* (cm/s)	R_{CT} (Ω)
2.0%	-1.46	3.26	-0.095	-0.310	5.75 x 10^{-3}	7918.7
4.4%	-2.53	3.29	-0.093	-0.297	1.42 x 10^{-2}	4839.8
6.0%	-1.78	3.45	-0.098	-0.297	6.50 x 10^{-3}	5252.5

The data do not definitively demonstrate trends of improved catalytic performance that correlate directly with the Ni-content of the catalyst. The catalyst containing 4.4% Ni outperforms the catalyst containing 6.1% Ni in terminal current density, onset potential, and kinetic rate constant, most notably. However, the catalyst containing 6.1% Ni has the highest calculated *n*-value.

As previously stated, data obtained by XPS indicated that the sample containing 4.4% Ni contained slightly more Mn^{3+} than the sample which contained 6.1% Ni. Chapter 3 extensively outlined the role of Mn^{3+} in the ORR. Because Mn^{3+} is d^4, the unpaired electron in the e_g orbital set promotes a geometric distortion. The presence of this unpaired electron also destabilizes the bond between the Mn and the surface OH^-, thereby promoting its displacement and the reduction of oxygen that follows. Previously, it has been hypothesized that Ni-dopants stabilize the formation of Mn^{3+} ions. [23] Therefore, it would be expected that Ni-content could serve as a fairly accurate basis for predicting the relative amounts of Mn^{3+} in the catalyst. However, our data do not indicate that this is the

case. While Ni-content is a factor that influences the catalytic performance, the trends in our electrocatalytic data do not directly coincide with the amount of Ni in the catalyst. A previous study by Garcia *et al.* also demonstrated that although the addition of Ni to MnO_x/C does enhance ORR catalysis initially, adding more Ni to the composite does not correspond to a linear increase in performance. [41]

The electrochemical data also demonstrate that catalyst surface area is not a sole predictor of catalytic performance. Despite the 6.1% Ni catalyst having the highest surface area in the series, it only outperforms the 4.4% Ni catalyst in *n*-value. In the future, RRDE studies should provide further insight regarding the predominant ORR pathway that occurs on Ni-α-MnO_2 catalysts. Ni-dopants in MnO_x catalysts have been cited as promoting the two-electron reduction and catalytic decomposition of peroxide. [23] Therefore, RRDE studies with these catalyst materials are expected to reveal if the formation of peroxide is decreased for the catalyst containing 6.1% Ni catalyst, indicating that the greater Ni-content corresponds to a more rapid reduction of the intermediate species.

This study demonstrates that the catalysis of the ORR is a complex process that is influenced by multiple physicochemical factors of the catalyst, such as surface area and Mn oxidation state. Further studies of Ni-α-MnO_2 nanowire catalysts are of interest, as the puzzling catalytic performance of these materials is not entirely explained by the physicochemical data collected thus far.

4.4 Summary and Conclusions

The synthesis of Ni-doped α-MnO_2 nanowires was achieved by the addition of $Ni(NO_3)_2 \cdot 6H_2O$ into the hydrothermal reaction previously used to prepare α-MnO_2 nanowires. [19, 24] By varying the amount of Ni-precursor in discrete molar ratios of 1:1, 1:0.5, and 1:0.25 (Mn:Ni), varying atomic percentages of Ni were attained in the reaction product – 6.1%, 4.4%, and 2.0%, respectively. The α-MnO_2 crystalline phase and the nanowire morphology were retained upon doping, factors known to be critical to the overall catalytic performance. The BET surface areas, average pore diameters, and pore volumes demonstrated an increase that correlated with Ni content.

There is some experimental evidence that doping α-MnO_2 nanowires with Ni improves their performance as catalysts for the ORR in alkaline electrolyte relative to the undoped α-MnO_2. Catalysts containing 4.4% and 6.1% Ni demonstrated higher terminal current densities than the undoped species. Also, the kinetic rate constant for the sample containing 4.4% Ni was greater than that of the undoped α-MnO_2 catalyst.

The addition of Ni–dopants in α-MnO_2 has some impact on the oxidation state of Mn, and specifically, the Mn^{3+}/Mn^{4+} redox couple. The oxidation state of Mn was approximated by examining the splitting of the Mn 3s peaks in the x-ray photoelectron spectra, which revealed that the greatest Mn^{3+} character exists in the sample containing 4.4% Ni (0.54% Ni at the surface). Mn^{3+} has a d-electron count of four (d^4), which indicates the presence of an unpaired electron in the degenerate e_g set in octahedral geometry. Through a distortion to the tetragonal geometry, the e_g orbitals split, leaving the unpaired electron in the d_z^2 orbital at a lower energy, oriented toward the surface OH^-. This electron destabilizes the bond between the Mn^{3+} ion and the surface hydroxide,

promoting the formation and subsequent reduction of O_2^{2-} on the surface. [63] Future studies will measure the amounts of peroxide formed for each Ni-α-MnO_2 catalyst, providing some additional insight into the predominant reaction pathway. Also, conductivity studies would enable further comparison to undoped α-MnO_2 and other catalytic species.

Chapter 5

Silver-Graphene Nanoribbon Composite Catalyst for the Oxygen Reduction Reaction in Alkaline Electrolyte

5.1 Introduction

Graphene has been described as the basic building block for all graphitic materials. [50] Graphite, fullerenes, and carbon nanotubes are graphitic materials of varying dimensionalities that are made of graphene, as illustrated in Figure 5.1.

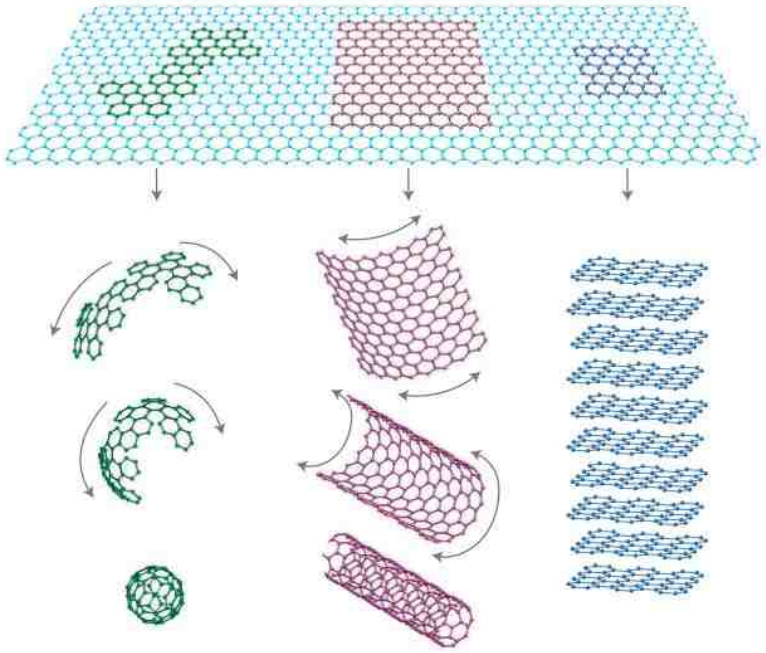

Figure 5.1: A graphene sheet can be formed into fullerene (left), carbon nanotubes (center), and graphite (right). [50]

Comprised of a network of sp^2 hybridized carbons arranged in a honeycomb structure, graphene is widely acknowledged for its unique electronic properties and high surface area, theoretically 2630 m^2/g for single-layer graphene. [50, 69] This unique material is often

utilized for applications in energy storage and conversion and has been employed in composite catalysts for the ORR. [70-73] Composite catalysts containing graphene are obtained through *in situ* syntheses or simple blending techniques. [70, 71] In a composite, the graphene component can offer enhanced conductivity and promote the apparent four-electron reduction pathway. Though graphene alone catalyzes the ORR via the less preferred two-electron process generating peroxide, the apparent four-electron process is favored when graphene is employed in a composite, preventing the accumulation of corrosive peroxide species. [24]

Graphenes utilized in composite catalysts have been obtained through chemical vapor deposition (CVD) methods and other synthetic techniques that yield chemically modified graphenes (CMGs). [71] CMGs include heteroatom-doped graphene, chemically reduced graphene oxide (RGO), and functionalized graphene. [71] Carbon nanotubes have also been used in composite catalysts. However, the electrocatalytic properties of graphene nanoribbons (GNRs) and related composites have not been fully investigated.

Graphene nanoribbons are thin, elongated strips of graphene obtained by the splitting of carbon nanotubes. [74, 75] A schematic of a gradual unzipping process is illustrated in Figure 5.2.

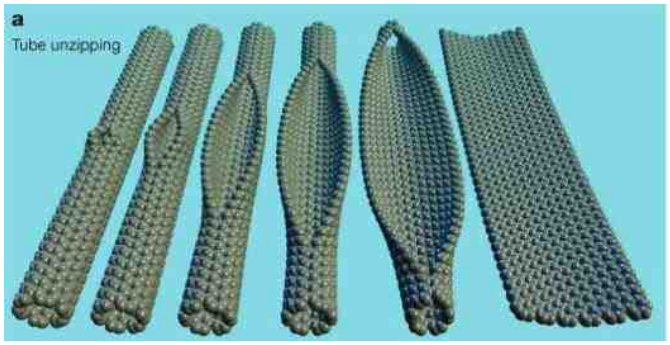

Figure 5.2: Generalized schematic demonstrating the unzipping of a nanotube, forming a nanoribbon. [74]

The edges of graphene nanoribbons have been reported to be uniquely reactive, both chemically and electronically. [76, 77] Density functional calculations have suggested that the nature of the nanoribbon edge lowers the barrier posed to oxygen adsorption and the first electron transfer of the ORR. [78] Therefore, the properties of graphene nanoribbons could provide for enhanced electrocatalytic performance.

Numerous studies have shown Ag and related composites to be active ORR catalysts. A recent report describes a reduced graphene oxide (RGO)-Ag composite with catalytic activities surpassing that of a commercial Ag/Vulcan Carbon composite (referred to as Ag/C) with similar Ag content. [79] The enhanced catalytic behavior was attributed to Ag nanoparticles that were smaller and more disperse than what existed on the Vulcan Carbon. Ag-MWCNTs (multi-walled carbon nanotubes) composites have also been reported to operate by a four-electron process. [20, 80] Another composite catalyst containing Ag was reported to achieve mass activities on the same order of magnitude as Pt/C catalysts. [81] Considering the demonstrated synergistic effects achieved by Ag and graphene-based materials, novel composite catalysts containing both Ag and GNRs are of interest.

5.2 Experimental

5.2.1 General

Full descriptions of the syntheses of the graphene nanoribbons and silver-graphene nanoribbon (Ag-GNR) composite catalyst are available in the recent publication that corresponds to this chapter. [82] Isopropanol and Nafion solution (5 wt. % solution in water and lower aliphatic alcohols) were used as received from Sigma-Aldrich. The

commercial benchmark used in this study, 20% Pt on Vulcan XC-72, was used as received from E-Tek. A commercial Ag/C composite, 60% Ag on Vulcan XC-72, was used as received from Premetek.

5.2.2 Synthesis and Characterization

A detailed description of the synthesis and characterization of Ag-GNRs is provided in Davis *et al*. [82] Briefly, Ag-GNRs were obtained by the unzipping of multi-walled carbon nanotubes (MWCNTs) achieved through the intercalation of Na/K alloy. Treating the partially split nanotubes with $Ag(O_2CCH_3)$ in the presence of Na/K causes reduction of the Ag ions, and Ag nanocrystals form on the carbon scaffold. Quenching the reaction with methanol completes the unzipping of the nanotubes. Transmission electron microscopy (TEM) revealed the Ag nanocrystals to range in size from 5 to 25 nm. TEM imaging and X-ray diffraction (XRD) confirmed the nanocrystallinity of the Ag species. Thermogravimetric analysis (TGA) revealed the Ag-GNR composite to be 70% percent Ag by weight. [82]

5.2.3 Electrochemical Analysis

To prepare the catalyst ink, the Ag-GNR composite (5.0 mg) was combined with isopropanol (200 μL) and Nafion solution (300 μL) in a small vial and thoroughly dispersed via ultrasonication for 20 minutes. Immediately following, 5.0 μL of the ink solution was deposited by micropipette onto the surface of a glassy carbon rotating disk electrode (RDE, BASi, active area = 0.0788 cm^2). The electrode was then allowed to dry at ambient temperature overnight. For rotating ring disk electrode studies, 10.0 μL of the prepared ink was drop-cast onto the glassy carbon disk, surrounded by a platinum ring electrode (Pine, disk area = 0.2475 cm^2, ring area= 0.1866 cm^2). Prior to each drop-

coating process, the RDE or RRDE glassy carbon electrode surface was polished with 0.05 μm alumina slurry and rinsed with deionized water and ethanol. The films were dried overnight at ambient temperature.

Linear Scanning Voltammograms were executed in a potential window from 0.2 V to -0.6 V (V vs. Ag/AgCl) at a scan rate of 1 mV/s. For RDE studies, a preliminary break-in scan at 500 rpm was conducted, followed by LSVs run at rotation rates of 500, 900, 1600, 2500, and 3600 rpm. For RRDE, LSVs were obtained at 500 and 2500 rpm in a potential window from 0.2 V to -0.6 V, and the reference was Hg/HgO. The collection efficiency of the ring electrode (*N*) was determined to be 37%. All experiments were run in 0.1 M KOH electrolyte that had been thoroughly purged with UHP oxygen (or UHP nitrogen for background measurements) prior to each run. The appropriate gaseous atmosphere was preserved via blanketing for the duration of the experiment.

RDE experiments were performed in a three-electrode cell, manufactured by Bioanalytical Systems, Inc. connected to a Versastat 4 potentiostat operated by VersaStudio software. Electrodes (from BASi) included the glassy carbon working electrode prepared as previously described, a Pt coil counter electrode, and a Ag/AgCl reference electrode (3 M NaCl, potential= 0.209 V vs. NHE). RRDE experiments were performed in a three-electrode cell, manufactured by Gamry Instruments connected to a Gamry Series G 750 Test System Bipotentiostat. Electrodes included the Gamry RDE710 rotating working electrode prepared as described, Pt foil as the counter electrode, and a Hg/HgO reference electrode (Hach, 0.1 M KOH, potential= 0.171 V vs. NHE). The percent peroxide was calculated from RRDE data using 100% x $X(H_2O_2)$;

$X(H_2O_2) = [2I_r / N]/[I_d + I_r/N]$. [6] I_r and I_d are the respective ring and disk currents, respectively, and N is the measured collection efficiency of the ring electrode. [6]

Charge transfer resistances were calculated from the slope of the linear portion of the current-potential curve at low overpotential (within ± 10 mV), recorded at 2500 rpm. Similar values were obtained using the 500 rpm data. Onset potentials were calculated from the intersection of approximated tangent lines from 0 V (base region before activation) and the half-wave potential ($E_{1/2}$), recorded at 2500 rpm.

Chronoamperometric studies were performed in a three-electrode configuration as described. The working electrode was subjected to a linear scan (2500 rpm) for which the terminal potential was -0.350 V vs. Ag/AgCl unless otherwise stated. The electrode was held at this potential for 250 seconds, at which time 2 weight percent methanol was rapidly injected into the electrochemical cell. The experiment continued for 600 seconds following the methanol injection, and the current response was monitored.

5.3 Results and Discussion

Rotating disk electrode studies were used to analyze the catalytic behavior of pure GNRs prepared by the unzipping procedure. The linear scanning voltammograms are shown in Figure 5.3.

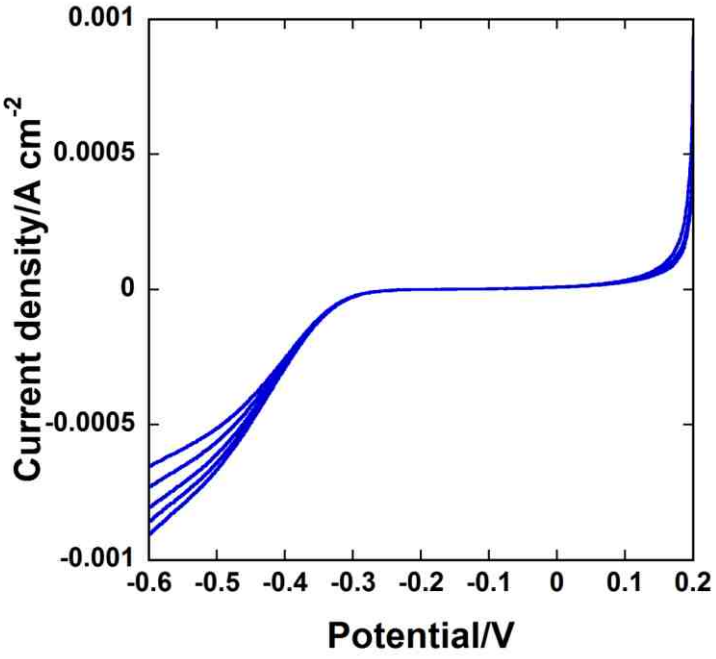

Figure 5.3: Linear scanning voltammograms for GNRs at 500, 900, 1600, 2500, and 3600 rpm.

As expected, an increase in electrode rotation rate causes an increase in observed current density. This is due to the resulting increase of O_2 flux to the surface of the catalyst. Applying the Koutecky-Levich equation to the LSV data yields an *n*-value of 1.97 e^-, indicating that the ORR is proceeding solely by the peroxide pathway.

High surface area carbons are commonly used in composite catalysts to enhance conductivities of the electrode materials. While the surface area for the GNRs (layers of ~30 to 40 ribbon sheets) was estimated to be 30 to 50 m^2/g, a comparison to a commercially available carbon of higher surface area, Vulcan Carbon, was performed. Because Vulcan Carbon is conductive and possesses a reasonably high surface area, it is commonly used in commercial electrocatalysts, such as the Ag/C and 20% Pt/C catalysts

utilized in this study. A comparison of the LSVs obtained at 2500 rpm for GNRs and Vulcan Carbon is provided in Figure 5.4.

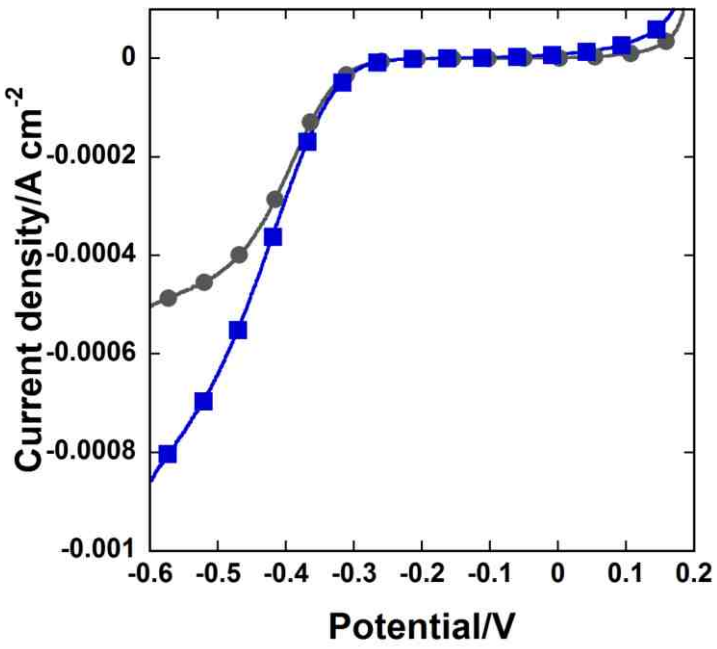

Figure 5.4: Comparison of commercial Vulcan Carbon (gray circles) to GNRs (blue squares) at 2500 rpm.

Even though the surface area of Vulcan Carbon (230 - 250 m^2/g) is significantly greater than that of the GNRs, the GNRs attain a greater terminal current density. As shown in the LSVs, the onset potentials for the Vulcan Carbon and the GNRs are similar (~ -0.322 V vs. Ag/AgCl). However, the kinetic rate constant obtained with GNRs (3.51 x 10^{-3} cm/s) is slightly greater than that obtained with Vulcan Carbon (2.69 x 10^{-3} cm/s). Also, the charge transfer resistance for the GNR catalyst (7998 Ω) is less than that of Vulcan Carbon (9068 Ω), providing some evidence to support that claim that GNRs lower the energetic activation barriers posed to oxygen adsorption and the initial charge transfer. [78]

Electrochemical testing of the synthesized Ag-GNR composite catalyst was performed. The LSVs obtained at increasing rotation rates are shown in Figure 5.5.

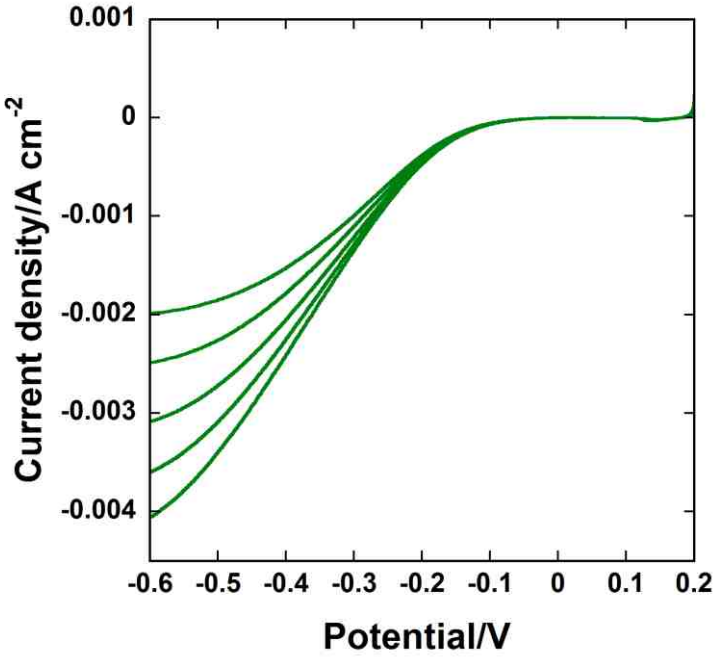

Figure 5.5: Linear scanning voltammograms for Ag-GNR.

It is immediately apparent that the terminal current density for the Ag-GNR composite at 2500 rpm is approximately 4 times greater than that attained by the GNRs alone. The Koutecky-Levich equation yielded an average *n*-value of 3.51 e^-. A value of 3.84 e^- was obtained for one trial, which is similar to the reported *n*-value of 3.9 e^- for a Ag-RGO composite. [79] The kinetic rate constant of 1.66 x 10^{-2} cm/s was also substantially improved relative to that attained with the GNRs alone. Also, the charge transfer resistance for the Ag-GNR composite (4328 Ω) was much lower than that of the GNRs, indicating that the Ag nanocrystals contribute significantly to the ORR catalysis.

A commercially available Ag/C composite was analyzed along with 20% Pt/C, commonly regarded to be a benchmark catalyst for the ORR. A composite plot of LSVs obtained at 2500 rpm is shown in Figure 5.6 and accompanied by corresponding electrocatalytic data, presented in Table 5.1.

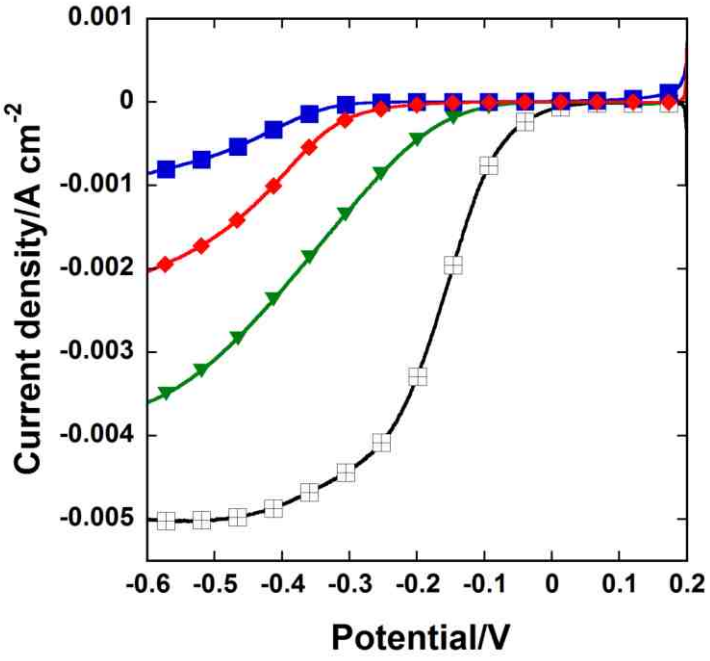

Figure 5.6: Composite plot for GNRs (blue squares), Ag/C (red diamonds), Ag-GNR (green triangles), and 20% Pt/C (black crossed squares), 2500 rpm.

Table 5.1: Electrocatalytic Data for GNRs, Ag/C, Ag-GNR, and 20% Pt/C

Sample	***n*-value (e^-)**	***k* (cm/s)**	**Onset (V)**	**$E_{1/2}$ (V)**	**R_{CT} (Ω)**
GNR	1.97	3.51×10^{-3}	-0.322	-0.445	7998
Ag/C	3.09	7.51×10^{-3}	-0.287	-0.428	4590
Ag-GNR	3.51	1.66×10^{-2}	-0.133	-0.352	4328
20% Pt/C	3.8	5.84×10^{-2}	-0.051	-0.214	2040

The Ag-GNR composite yields improved onset potentials and half-wave potentials relative to both the GNR and Ag/C catalyst. Compared to the Ag/C composite, the onset potential of the Ag-GNR catalyst is improved by 0.154 V while the half-wave potential improves by 0.076 V. A slight improvement in charge transfer resistance is noted for Ag-GNR as well. However, as expected, the 20% Pt/C benchmark catalyst drastically outperforms the Ag-GNR.

Rotating ring disk electrode studies were conducted to provide additional insight into the predominant reaction pathway for each catalyst material. Figure 5.7 shows $X(H_2O_2)$ plotted as a function of potential where $X(H_2O_2) = [2I_r/N]/[I_d + I_r/N]$. [6] The percent of evolved peroxide can be obtained by 100% x $X(H_2O_2)$.

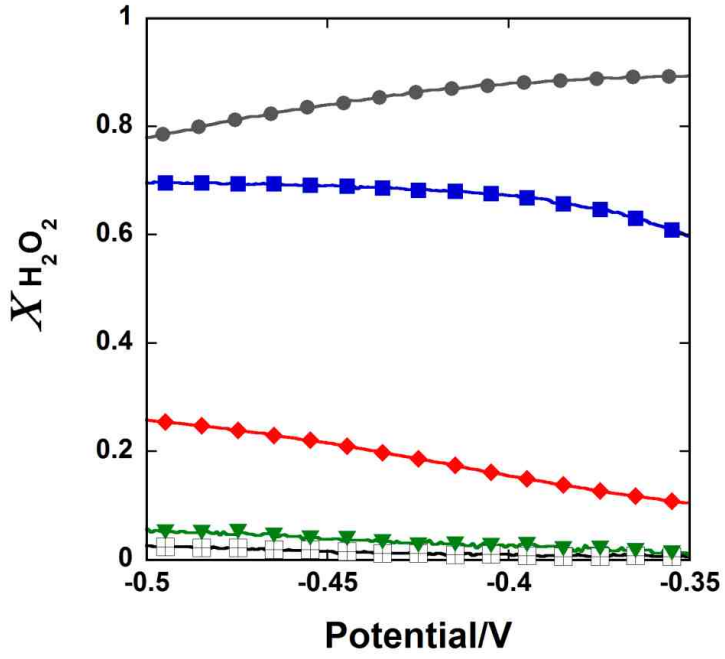

Figure 5.7: RRDE data obtained at 500 rpm for Vulcan Carbon (gray circles), GNR (blue squares), Ag/C (red diamonds), Ag-GNR (green triangles), and 20% Pt/C (black crossed squares).

The RRDE data for the Vulcan Carbon and GNRs corroborates the *n*-values ~ 2 e^- obtained by the Koutecky-Levich equation. Over a potential range of -0.350 V to -0.500 V, the Vulcan carbon produces more than 80% peroxide, and the GNRs produce more than 60% peroxide. While the percentage of formed peroxide is decreased further with the Ag/C composite, the percentages are even lower for the Ag-GNR composite and 20% Pt/C, as shown in Figure 5.8.

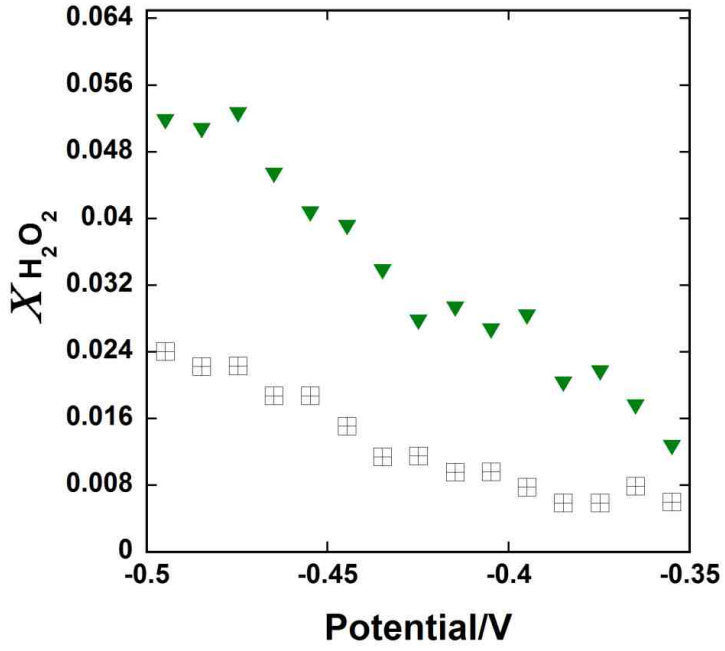

Figure 5.8: RRDE data for Ag-GNR (green squares) and 20% Pt/C (crossed squares), 500 rpm.

The amount of peroxide evolved for the Ag-GNR catalyst ranges from ~1.6% to 5.2%, whereas the 20% Pt/C generates ~0.8% to 2.4% peroxide. For both catalysts, more peroxide is produced at more negative potentials. These results indicate that an apparent four-electron pathway is the predominant process for the Ag-GNR composite.

Pt/C catalysts are susceptible to deactivation by methanol crossover effects and carbon monoxide poisoning, thus severely limiting performance. As a preliminary probe

to test potential crossover effects in alkaline fuel cells, the electrocatalytic selectivities of Ag-GNR and 20% Pt/C were studied via chronoamperometry at a constant potential of -0.350 V vs. Ag/AgCl. The results are shown in Figures 5.9 and 5.10.

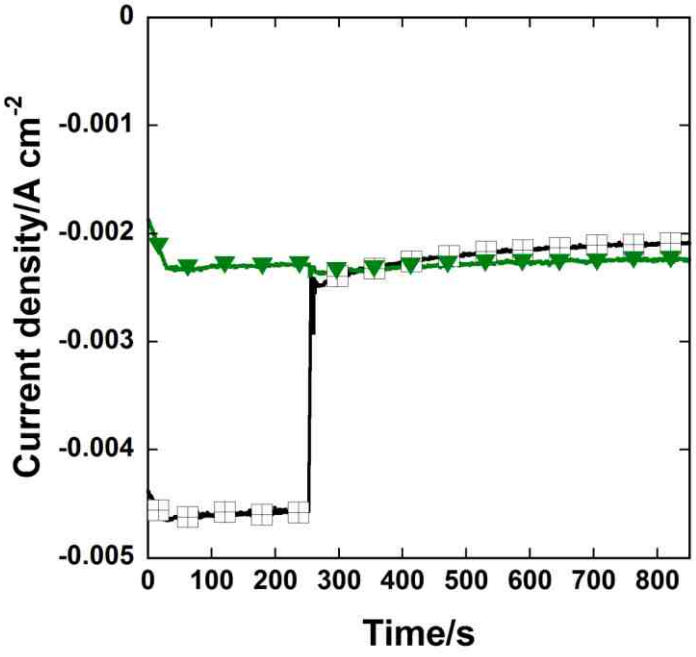

Figure 5.9: *i-t* chronoamperometric data for Ag-GNR (green triangles) and 20% Pt/C (crossed squares), 1000 rpm. Electrodes were held at a constant potential of -0.350 V vs. Ag/AgCl. Injection of 2 weight percent methanol occurred at *t*=250 seconds.

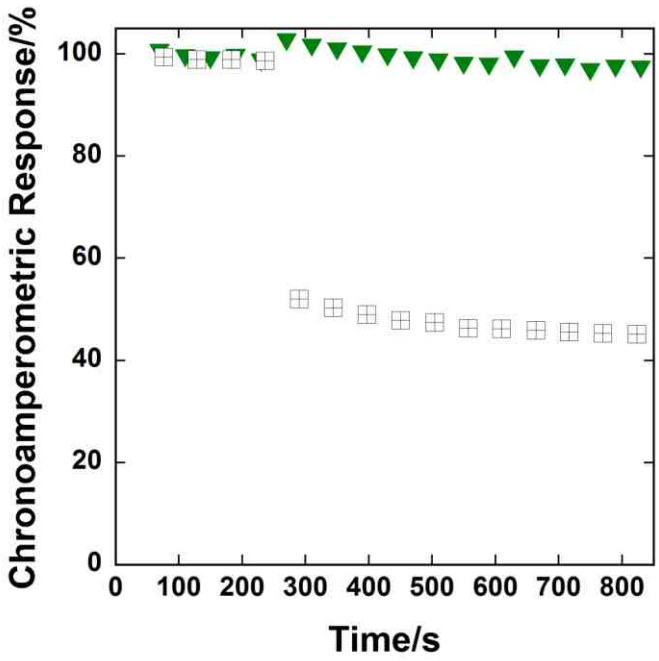

Figure 5.10: Percent chronoamperometric response data for Ag-GNR (green triangles) and 20% Pt/C (crossed squares) at -0.350 V upon injection of 2 weight percent methanol at *t*=250 seconds.

Upon the addition of 2 weight percent methanol into the electrochemical cell, 20% Pt/C suffers a drastic decrease in current density of ~50%. In contrast, the Ag-GNR composite shows a stable response with < 5% decrease in current density, as exhibited in Figures 5.9 and 5.10. In the presence of methanol, the Ag-GNR composite is generating about the same amount of current as the 20% Pt/C catalyst, indicating that it is not subject to the potential deleterious effects of methanol crossover.

5.4 Summary and Conclusions

Graphene nanoribbons are an interesting type of graphene material with electrocatalytic properties that had not yet been employed in a composite catalyst. Ag is a catalytically active metal that has been successfully utilized in graphene composites and

is significantly more viable economically than Pt. Therefore, the study of a novel Ag-GNR composite was of interest, and our catalytic studies revealed that the Ag-GNR composite outperforms the composite Ag/C catalyst for the ORR. This composite material operates by an apparent four-electron process with < 5% peroxide produced in 0.1 M KOH. When subjected to simulated methanol crossover effects, the Ag-GNR demonstrated electrocatalytic selectivity much better than the commercial benchmark, 20% Pt/C.

Chapter 6

Summary and Conclusions

The oxygen reduction reaction (ORR) is a critical electrochemical process that occurs in both fuel cells and metal-air batteries. While Pt and Pt-based alloys are currently considered the benchmark catalysts for this reaction due to their remarkable catalytic behaviors, these materials are costly and relatively rare, accelerating the need for novel, highly active, affordable catalyst materials.

Nanoscale manganese oxides have been extensively investigated as catalysts for the ORR in alkaline electrolyte. Nanowires have been demonstrated to be the most active nanoscale morphology. [19] In addition, α-MnO_2 has been identified as the most active crystalline phase. Previous studies have demonstrated that doping manganese oxide catalysts with transition metals can improve the catalytic performance relative to the undoped species. Building upon recent work, [24] the current study sought to gain more insight into the roles of Cu and Ni-dopants in α-MnO_2 nanowire electrocatalysts.

Cu-α-MnO_2 and Ni-α-MnO_2 nanowires containing varied amounts of dopant were synthesized via a modified hydrothermal technique. The physical properties of the catalysts were characterized. Rotating disk electrode (RDE) studies were performed to assess the catalytic performance of the doped nanowires.

Composite catalyst materials containing graphene are also of interest, as graphene has been demonstrated to enhance the conductivity of the composite while promoting the more favorable four-electron reduction process. The catalytic behaviors of graphene nanoribbons (GNRs) obtained by the chemical unzipping of multi-walled carbon nanotubes (MWCNTs) have not been extensively studied. A novel composite material

consisting of Ag-nanoparticles formed on GNRs (Ag-GNR) was analyzed for its ability to catalyze the ORR. [82]

Elucidating the Role of Cu-dopants in α-MnO_2 Nanowire Electrocatalysts for the Oxygen Reduction Reaction in Alkaline Media

- Doping α-MnO_2 nanowires with Cu improves their performance as catalysts for the ORR in alkaline electrolyte.
- The inclusion of this dopant species provides for not only higher terminal current densities, but also enhanced kinetic rate constants that exceed rates attained by α-MnO_2 alone. Also, the charge transfer resistances decrease as the amount of Cu-dopant in the nanowires increases.
- X-ray photoelectron spectroscopy (XPS) revealed an increase in Mn^{3+} character in the catalyst that corresponds to an increased amount of Cu-dopant at the surface. Mn^{3+}, which is a d^4 species, likely demonstrates enhanced catalytic performance due to asymmetric filling of the e_g orbital set; the resulting geometric distortion is hypothesized to promote oxygen reduction on the catalyst surface. [63]

Efforts to Understand the Role of Ni-dopants in α-MnO_2 Nanowire Catalysts for the Oxygen Reduction Reaction in Alkaline Media

- There is some data that suggest doping α-MnO_2 nanowires with Ni improves their performance as ORR catalysts; the catalysts containing 4.4% Ni and 6.1% Ni demonstrated higher terminal current densities than the undoped species. The sample containing 4.4% Ni demonstrated the most improvement in kinetic rate constant relative to the undoped species. The sample containing 6.1% Ni yields an *n*-value of 3.45 e^-, greater than *n*=3.1 e^- for undoped α-MnO_2.

- As observed for the Cu-α-MnO_2 catalysts, the correlation between Mn^{3+} character and dopant concentration as studied by XPS can provide some basis for rationalizing the demonstrated catalytic performance of Ni-α-MnO_2 catalysts as well.

Silver-Graphene Nanoribbon Composite Catalyst for the Oxygen Reduction Reaction in Alkaline Electrolyte

- Catalytic studies revealed that the Ag-GNR composite outperforms a commercial Ag-Carbon (Ag/C) catalyst; the *n*-value (3.51 e^-) and kinetic rate constant (1.66 x 10^{-2} cm/s) were improved, as were the onset potential (-0.133 V) and half-wave potential (-0.352 V).
- Rotating ring disk electrode (RRDE) studies revealed that the Ag-GNR composite generates ~1.6% to 5.2% peroxide, which is significantly lower than the amount generated by commercial Ag/C (10% to 25%) and only slightly higher than the amount generated by 20% Pt/C (~0.8% to 2.4%).
- When subjected to simulated methanol crossover effects, the Ag-GNR demonstrated a slight decrease in current density (< 5%), whereas the benchmark 20% Pt/C suffered a drastic decrease of ~50%; therefore, the electrocatalytic selectivity of the Ag-GNR catalyst is improved significantly relative to the benchmark.

References

1. Cheng, F. and J. Chen, *Metal-air batteries: from oxygen reduction electrochemistry to cathode catalysts.* Chemical Society Reviews, 2012. **41**(6): p. 2172-2192.

2. Girishkumar, G., *et al*., *Lithium−Air Battery: Promise and Challenges.* The Journal of Physical Chemistry Letters, 2010. **1**(14): p. 2193-2203.

3. Zheng, Y., *et al*., *Nanostructured metal-free electrochemical catalysts for highly efficient oxygen reduction.* Small (Weinheim an der Bergstrasse, Germany), 2012. **8**(23).

4. Palacin, M.R., *Recent advances in rechargeable battery materials: a chemist's perspective.* Chemical Society Reviews, 2009. **38**(9): p. 2565-2575.

5. Hoare, J.P., *The Electrochemistry of Oxygen*. 1968: Interscience Publishers, John Wiley & Sons, Inc.

6. Paulus, U.A., *et al.*, *Oxygen reduction on a high-surface area Pt/Vulcan carbon catalyst: a thin-film rotating ring-disk electrode study.* Journal of Electroanalytical Chemistry, 2001. **495**: p. 134-145.

7. Yeager, E., *Electrocatalysts for O_2 reduction.* Electrochimica Acta, 1984. **29**(11): p. 1527-1537.

8. Pleskov, Y.V. and V.Y. Filinovskii, *The Rotating Disk Electrode*. 1976, New York: Plenum Publishing Corporation.

9. Jorissen, L., *Bifunctional oxygen/air electrodes.* Journal of Power Sources, 2006. **155**: p. 23-32.

10. Trotochaud, L., *et al*., *Solution-Cast Metal Oxide Thin Film Electrocatalysts for Oxygen Evolution.* Journal of the American Chemical Society, 2012. **134**(41): p. 17253-17261.

11. Takashima, T., K. Hashimoto, and R. Nakamura, *Inhibition of Charge Disproportionation of MnO_2 Electrocatalysts for Efficient Water Oxidation under Neutral Conditions.* Journal of the American Chemical Society, 2012. **134**(44): p. 18153-18156.

12. Appleby, A.J., *Electrocatalysis of aqueous dioxygen reduction.* Journal of Electroanalytical Chemistry, 1993. **357**: p. 117-119.

13. Christensen, P.A., A. Hamnett, and D. Linares-Moya, *Oxygen reduction and fuel oxidation in alkaline solution.* Physical Chemistry Chemical Physics, 2011. **13**: p. 5206-5214.

14. Albery, W.J. and M.L. Hitchman, *Ring-Disc Electrodes*. 1971, London: Oxford University Press.

15. *Probing Fuel Cell Electrocatalyst Properties Using Pine Rotating Disk and Ring-Disk Electrodes: Overview of the Nafion Thin-Film RRDE Technique*. 2007, Pine Research Instrumentation. p. 1-5.

16. Mayrhofer, K.J.J., *et al.*, *Measurement of oxygen reduction activities via the rotating disc electrode method: From Pt model surfaces to carbon-supported high surface area catalysts.* Electrochimica Acta, 2008. **53**: p. 3181-3188.

17. Gojkovic, S.L., S.K. Zecevic, and R.F. Savinell, *O_2 Reduction on an Ink-Type Rotating Disk Electrode Using Pt Supported on High-Area Carbons.* Journal of the Electrochemical Society, 1998. **145**(11): p. 3713-3720.

18. Bard, A.J. and L.R. Faulkner, *Electrochemical Methods: Fundamentals and Applications*. 2nd ed. 2000: Wiley.

19. Cheng, F., *et al.*, *MnO_2-Based Nanostructures as Catalysts for Electrochemical Oxygen Reduction in Alkaline Media.* Chemistry of Materials, 2010. **22**(3): p. 898-905.

20. Spendelow, J.S. and A. Wieckowski, *Electrocatalysis of oxygen reduction and small alcohol oxidation in alkaline media.* Physical Chemistry Chemical Physics, 2007. **9**(21): p. 2654-2675.

21. Genies, L., R. Faure, and R. Durand, *Electrochemical reduction of oxygen on platinum nanoparticles in alkaline media.* Electrochimica Acta, 1998. **44**: p. 1317-1327.

22. Antoine, O. and R. Durand, *RRDE study of oxygen reduction on Pt nanoparticles inside Nafion: H_2O_2 production in PEMFC cathode conditions.* Journal of Applied Electrochemistry, 2000. **30**: p. 839-844.

23. Roche, I., *et al.*, *Carbon-supported manganese oxide nanoparticles as electrocatalysts for the Oxygen Reduction Reaction (ORR) in alkaline medium: Physical characterizations and ORR mechanism.* Journal of Physical Chemistry C, 2007. **111**(3): p. 1434-1443.

24. Lambert, T.N., *et al.*, *Graphene-Ni-α-MnO_2 and -Cu-α-MnO_2 nanowire blends as highly active non-precious metal catalysts for the oxygen reduction reaction.* Chemical Communications, 2012. **48**(64): p. 7931-7933.

25. Zoltowski, P., D.M. Drazic, and L. Vorkapic, *Carbon-air electrode with regenerative short time overload capacity: Part 1. Effect of manganese dioxide.* Journal of Applied Electrochemistry, 1973. **3**: p. 271-283.

26. Xiao, W., D. Wang, and X.W. Lou, *Shape-Controlled Synthesis of MnO_2 Nanostructures with Enhanced Electrocatalytic Activity for Oxygen Reduction.* Journal of Physical Chemistry C, 2010. **114**(3): p. 1694-1700.

27. Lima, F.H.B., M.L. Calegaro, and E.A. Ticianelli, *Investigations of the catalytic properties of manganese oxides for the oxygen reduction reaction in alkaline media.* Journal of Electroanalytical Chemistry, 2006. **590**: p. 152-160.

28. Liu, X., *et al*., *A Review on the Synthesis of Manganese Oxide Nanomaterials and Their Applications on Lithium-Ion Batteries.* Journal of Nanomaterials, 2013. **2013**: p. 1-7.

29. Truong, T.T., *et al*., *Morphological and Crystalline Evolution of Nanostructured MnO_2 and Its Application in Lithium-Air Batteries.* ACS Nano, 2012. **6**(9): p. 8067-8077.

30. Devaraj, S. and N. Munichandraiah, *Effect of Crystallographic Structure of MnO_2 on Its Electrochemical Capacitance Properties.* The Journal of Physical Chemistry C, 2008. **112**(11): p. 4406-4417.

31. Cheng, F., *et al*., *Facile Controlled Synthesis of MnO_2 Nanostructures of Novel Shapes and Their Application in Batteries.* Inorganic Chemistry, 2006. **45**(5): p. 2038-2044.

32. Sun, M., *et al*., *Controlled synthesis of nanostructured manganese oxide: crystalline evolution and catalytic activities.* CrystEngComm, 2013. **15**: p. 7010-7018.

33. Qiu, G., *et al*., *Hydrothermal Synthesis of Manganese Oxide Nanomaterials and Their Catalytic and Electrochemical Properties.* Chemistry of Materials, 2011. **23**: p. 3892-3901.

34. Cheng, F., *et al*., *Selective Synthesis of Manganese Oxide Nanostructures for Electrocatalytic Oxygen Reduction.* ACS Applied Materials & Interfaces, 2009. **1**(2): p. 460-466.

35. Chabre, Y. and J. Pannetier, *Structural and electrochemical properties of the proton / γ-MnO_2 system.* Progress in Solid State Chemistry, 1995. **23**(1): p. 1-130.

36. Zhou, H., *et al.*, *Studies of Decomposition of H_2O_2 over Manganese Oxide Octahedral Molecular Sieve Materials.* Journal of Catalysis, 1998. **176**: p. 321-328.

37. Voinov, M., *MnO_2: Structure and Activity.* Electrochimica Acta, 1982. **27**(7): p. 833-835.

38. Cao, Y.L., *et al.*, *The mechanism of oxygen reduction on MnO_2-catalyzed air cathode in alkaline solution.* Journal of Electroanalytical Chemistry, 2003. **557**: p. 127-134.

39. Han, X., *et al*., *Porous calcium-manganese oxide microspheres for electrocatalytic oxygen reduction with high activity.* Chemical Science, 2013. **4**(1): p. 368-376.

40. Ríos, E., *et al.*, *Electrocatalysis of oxygen reduction on $Cu_xMn_{3-x}O_4$ spinel particles/polypyrrole composite electrodes.* International Journal of Hydrogen Energy, 2008. **33**(19): p. 4945-4954.

41. Garcia, A.C., *et al.*, *Evaluation of Several Carbon-Supported Nanostructured Ni-Doped Manganese Oxide Materials for the Electrochemical Reduction of Oxygen.* Journal of the Electrochemical Society, 2011. **158**(3): p. B290-B296.

42. Benbow, E.M., *et al*., *Oxygen Reduction Properties of Bifunctional alpha-Manganese Oxide Electrocatalysts in Aqueous and Organic Electrolytes.* Journal of Physical Chemistry C, 2011. **115**(44): p. 22009-22017.

43. El-Deab, M.S. and T. Ohsaka, *Electrocatalysis by design: Effect of the loading level of Au-nanoparticles-MnO_x nanoparticles binary catalysts on the electrochemical reduction of molecular oxygen.* Electrochimica Acta, 2007. **2007**: p. 2166-2174.

44. Tang, Q., *et al*., *One step synthesis of carbon-supported Ag/Mn_yO_x composites for oxygen reduction reaction in alkaline media.* Applied Catalysis B: Environmental, 2011. **104**: p. 337-345.

45. Cheng, F., *et al.*, *Enhancing Electrocatalytic Oxygen Reduction on MnO_2 with Vacancies.* Angewandte Chemie-International Edition, 2013. **52**(9): p. 2474-2477.

46. Feng, J., *et al.*, *Engineering manganese oxide/nanocarbon hybrid materials for oxygen reduction electrocatalysis.* Nano Research, 2012. **5**(10): p. 718-725.

47. Lee, J.S., *et al*., *Ionic liquid modified graphene nanosheets anchoring manganese oxide nanoparticles as efficient electrocatalysts for Zn-air batteries.* Energy & Environmental Science, 2011. **4**(10): p. 4148-4154.

48. Bezdicka, P., Grygar, T., Klapste, B., Vondrak, J., *MnO_x/C composites as electrode materials. I. Synthesis, XRD and cyclic voltammetric investigation.* Electrochimica Acta, 1999. **45**: p. 913-920.

49. Roche, I., *et al.*, *Durability of carbon-supported manganese oxide nanoparticles for the oxygen reduction reaction (ORR) in alkaline medium.* Journal of Applied Electrochemistry, 2008. **38**(9): p. 1195-1201.

50. Geim, A.K. and K.S. Novoselov, *The rise of graphene.* Nature Materials, 2007. **6**(3): p. 183-191.

51. Hummers, W.S. and R.E. Offeman, *Preparation of Graphitic Oxide.* Journal of the American Chemical Society, 1958. **80**: p. 1339.

52. Marcano, D.C., *et al.*, *Improved Synthesis of Graphene Oxide.* ACS Nano, 2010. **4**(8): p. 4806-4814.

53. Park, S., *et al.*, *Hydrazine-reduction of graphite- and graphene oxide.* Carbon, 2011. **49**: p. 3019-3023.

54. Cao, Y., *et al.*, *alpha-MnO_2 nanorods grown in situ on graphene as catalysts for Li-O-2 batteries with excellent electrochemical performance.* Energy & Environmental Science, 2012. **5**(12): p. 9765-9768.

55. Qian, Y., S.B. Lu, and F.L. Gao, *Synthesis of manganese dioxide/reduced graphene oxide composites with excellent electrocatalytic activity toward reduction of oxygen.* Materials Letters, 2011. **65**(1): p. 56-58.

56. Wu, J., *et al.*, *Manganese oxide-graphene composite as an efficient catalyst for 4-electron reduction of oxygen in alkaline media.* Electrochimica Acta, 2012. **75**: p. 305-310.

57. Toupin, M., T. Brousse, and D. Belanger, *Influence of Microstructure on the Charge Storage Properties of Chemically Synthesized Manganese Dioxide.* Chemistry of Materials, 2002. **14**: p. 3496-3952.

58. Nelson, A.J., J.G. Reynolds, and J.W. Roos, *Core-level satellites and outer core-level multiplet splitting in Mn model compounds.* Journal of Vacuum Science and Technology A, 2000. **18**(4): p. 1072-1076.

59. Rossouw, M.H., *et al.*, *Alpha Manganese Dioxide for Lithium Batteries: A Structural and Electrochemical Study.* Materials Research Bulletin, 1992. **27**: p. 221-230.

60. Brenet, J.P., *Electrochemical Behavior of Metallic Oxides.* Journal of Power Sources, 1979. **4**: p. 183-190.

61. Shannon, R.D., *Revised Effective Ionic Radii and Systematic Studies of Interatomic Distances in Halides and Chalcogenides.* Acta Crystallographica, 1976. **A32**: p. 751-767.

62. Hasan, M.A., *et al.*, *Promotion of the hydrogen peroxide decomposition activity of manganese oxide catalysts.* Applied Catalysis A: General, 1999. **181**: p. 171-179.

63. Suntivich, J., *et al., Design principles for oxygen-reduction activity on perovskite oxide catalysts for fuel cells and metal-air batteries.* Nature Chemistry, 2011. **3**: p. 546-550.

64. Sokol'skii, G.V., *et al., Effects of Electrochemical Doping of Manganese Dioxide with Copper and Lithium on the Physiochemical Properties.* Powder Metallurgy and Metal Ceramics, 2006. **45**: p. 158-162.

65. Bhide, V.G. and R.H. Dani, *Electrical Conductivity in Oxides of Manganese and Related Compounds.* Physica, 1961. **27**: p. 821-826.

66. Li, Q., *et al., Copper Doped Hollow Structured Manganese Oxide Mesocrystals with Controlled Phase Structure and Morphology as Anode Materials for Lithium Ion Battery with Improved Electrochemical Performance.* ACS Applied Materials & Interfaces, 2013.

67. Ding, K.-Q., *Direct Preparation of Metal Ions-doped Manganese Oxide by Cyclic Voltammetry.* Journal of the Chinese Chemical Society, 2008. **55**: p. 543-549.

68. Trari, M., *et al., Preparation and physical properties of the solid solutions* $Cu_{1+x}Mn_{1-x}O_2$. Journal of Solid State Chemistry, 2005. **178**: p. 2751-2758.

69. Stoller, M.D., *et al., Graphene-Based Ultracapacitors.* Nano Letters, 2008. **8**(10): p. 3498-3502.

70. Liang, Y., *et al., Strongly coupled inorganic/nanocarbon hybrid materials for advanced electrocatalysis.* Journal of the American Chemical Society, 2013. **135**(6): p. 2013-2036.

71. Huang, C., C. Li, and G. Shi, *Graphene based catalysts.* Energy & Environmental Science, 2012. **5**: p. 8848-8868.

72. Chen, D., H. Feng, and J. Li, *Graphene Oxide: Preparation, Functionalization, and Electrochemical Applications.* Chemical Reviews, 2012. **112**: p. 6067-6053.

73. Bai, S. and X. Shen, *Graphene-inorganic nanocomposites.* RSC Advances, 2012. **2**: p. 64-98.

74. Kosynkin, D.V., *et al., Longitudinal unzipping of carbon nanotubes to form graphene nanoribbons.* Nature, 2009. **458**: p. 872-878.

75. Kosynkin, D.V., *et al., Highly Conductive Graphene Nanoribbons by Longitudinal Splitting of Carbon Nanotubes Using Potassium Vapor.* ACS Nano, 2011. **5**(2): p. 968-974.

76. Nakada, K., *et al., Edge state in graphene ribbons: Nanometer size effect and edge shape dependence.* Physical Review B, 1996. **54**(24): p. 17954-17961.

77. Barone, V., O. Hod, and G.E. Scuseria, *Electronic Structure and Stability of Semiconducting Graphene Nanoribbons.* Nano Letters, 2006. **6**(12): p. 2748-2754.

78. Kim, H., *et al*., *On the mechanism of enhanced oxygen reduction reaction in nitrogen-doped graphene nanoribbons.* Physical Chemistry Chemical Physics, 2011. **13**(39): p. 17505-17510.

79. Lim, E.J., *et al*., *Highly dispersed Ag nanoparticles on nanosheets of reduced graphene oxide for oxygen reduction reaction in alkaline media.* Electrochemistry Communications, 2013. **28**: p. 100-103.

80. Tammeveski, L., *et al*., *Electrocatalytic oxygen reduction on silver nanoparticle/multi-walled carbon nanotube modified glassy carbon electrodes in alkaline solution.* Electrochemistry Communications, 2012. **20**: p. 15-18.

81. Demarconnay, L., C. Coutanceau, and J.M. Leger, *Electroreduction of dioxygen (ORR) in alkaline medium on Ag/C and Pt/C nanostructured catalysts - effect of the presence of methanol.* Electrochimica Acta, 2004. **49**(25): p. 4513-4521.

82. Davis, D.J., *et al*., *Silver-graphene Nanoribbon Composite Catalyst for the Oxygen Reduction Reaction in Alkaline Electrolyte.* Electroanalysis, 2014. DOI: 10.1002/elan.201300254